THE ROLE OF VORTEX RING FORMATION AND PRESSURE DROP ON DYNAMICS OF THE LEFT VENTRICLE DURING DIASTOLE

Thesis by
Arash Kheradvar

In Partial Fulfillment of the Requirements for the Degree of
Doctor of Philosophy

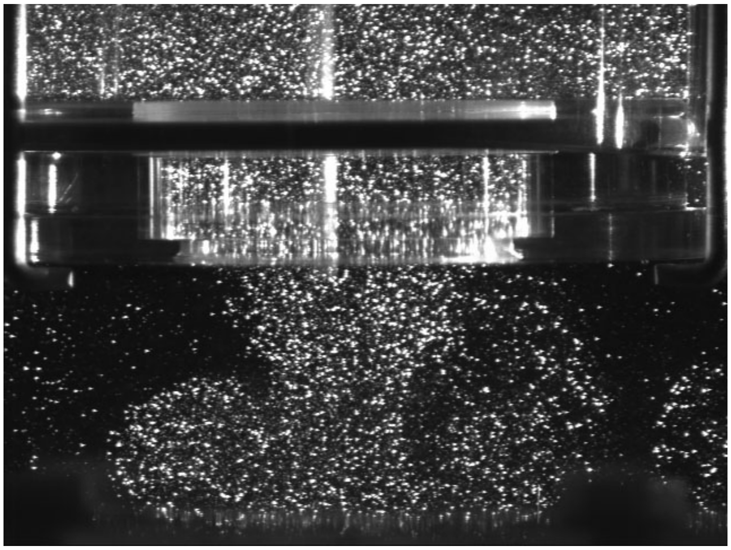

California Institute of Technology
Pasadena, California

2007
(Defended November 1, 2006)

This work is dedicated to my parents for being my first and greatest teachers
and to my wife because of her unconditional and perpetual love and support

Acknowledgements

I wish to express my sincere thanks to Professor *Mory Gharib* for being the best advisor I could have ever had during the years of my education. Mory provided me with the intellectual freedom to be raised as an independent researcher. I appreciate what I have learned from him, not only the broad knowledge, sharp scientific instinct and creative ideas, but also the optimistic and friendly attitude. I believe that the influence of Mory on my scientific life is beyond this thesis and I hope I will be able to have such an effect on my future students and colleagues.

During the past few years in Caltech, I had the privilege to get to know people who had influence in my scientific and personal life. I am particularly thankful to the members of my thesis committee, Prof. *Scott Fraser*, Prof. *Ivan Vesely* and Prof. *Anthony Leonard*, for their active participations and the insightful feedbacks. Among the friends, I would like to especially thank *Arash Yavari, Michele Milano, Ben Lin, Derek Rinderknecht, Arian Forouhar, Anna Hickerson, Anya Grosberg, Gwyneth Card, Maziar Motahari, Aydin Babakhani, Amy Kar-Wei Lam* and *Amir Sadjadpour*. I would also like to express my gratitude to all the past and present members of Gharib group for their unconditional support.

In addition, I am grateful to Prof. *Ken Pickar* for teaching me how to think as an entrepreneur, to Prof. *Guruswami Ravichandran* for his support and for the discussions we had on *FORMAVALVE* project, to Prof. *Michael Dickinson* for giving me the opportunity to use his lab equipments and to Edwards Lifesciences Corporation for providing me with the bioprosthetic heart valves.

Among many others whom I wish to acknowledge, I am particularly grateful to the past and present staff of the Caltech: *Jim Endrizzi, Parandeh Kia,* Prof. *Rod Kiewiet, Linda Scott* and *Kathleen Hamilton* for their kind support and, to *Rick Paniagua* and *Tony Tooski* for their careful technical support to my projects. I would also like to thank the *Rosen family* who endowed the *Benjamin M. Rosen* fellowship that supported my first year at Caltech.

I would like to thank my mom; her love and support have kept me strong even during the most difficult days. I am also grateful to my dad for his unreserved support in my life. Finally, thanks to my wife *Ladan* for giving me charm and ecstasy, for being full of love and support and for making my life so colorful.

Arash Kheradvar
November 1, 2006

Abstract

The role of vortex ring formation and pressure drop on dynamics of the left ventricle during diastole

By
Arash Kheradvar

In the field of cardiology, the current ability to accurately detect diastolic dysfunction is unsatisfactory due to the lack of an effective diagnostic index. Currently, assessments of diastolic dysfunction are based on echocardiographic measurements that are assumed to be correlated with progression from mild dysfunction to more severe disease. However, relying on existing ultrasonic indices for diagnosis of diastolic failure leads us to underestimate the progress of dysfunction. The presence of vortical flow that develops along with a strong propulsive trans-mitral jet during diastole in a normal left ventricle has been demonstrated by different imaging modalities. Thus, physical characteristics of these vortical structures may provide more effective indices of diastolic function than existing ones. In the first few chapters of this thesis, I fully describe the relationship between physical characteristics of these vortices and the dynamics of mitral valve during diastole. We found that regardless of the valve size and the pressure drop time-constant, the mitral annuls recoil computed would be maximized when the trans-mitral vortex ring pinches off in a range of formation time between three and five.

In chapter five, I introduce a novel technique that can estimate the viscoelastic properties of the left ventricle based on harmonic behavior of the ventricular chamber. Elastic deformations resulting from the changes in the ventricular mechanical properties of

myocardium are represented as a time-varying spring, while the viscous components of the model include a time-varying viscous damper, representing relaxation and the frictional energy loss.

In the final chapter, I discussed about effect of isovolumic relaxation phase on diastolic rapid filling in the process of post infarction cardiac remodeling in sheep. The results of this study confirmed that the post-infarction changes in isovolumic relaxation phase have direct influence on diastolic rapid filling phase, which leads to complex variations in end-diastolic lengthening and end-systolic shortening of the LV contractile elements.

Table of Contents

CHAPTER ONE. INTRODUCTION AND BACKGROUND

CHAPTER TWO. CORRELATION BETWEEN VORTEX RING FORMATION AND MITRAL ANNULUS DYNAMICS DURING VENTRICULAR RAPID FILLING

CHAPTER THREE. INFLUENCE OF MITRAL VALVE KINEMATICS AND LEFT VENTRICULAR PRESSURE DROP ON ANNULUS PLANE DYNAMICS

CHAPTER FOUR. IMPACT OF VENTRICULAR PRESSURE DROP ON EARLY DIASTOLIC MITRAL RECOIL THROUGH VORTEX FORMATION TIME

CHAPTER FIVE. **A**SSESSMENT OF **L**EFT **V**ENTRICULAR **V**ISCOELASTIC **C**OMPONENTS BASED ON MITRAL **A**NNULUS **H**ARMONIC **B**EHAVIOR

CHAPTER SIX. **E**FFECT OF **I**SOVOLUMIC **R**ELAXATION **P**HASE ON **D**IASTOLIC **R**APID **F**ILLING IN THE **P**ROCESS OF **P**OSTINFACTION **C**ARDIAC **R**EMODELING

APPENDIX

List of Figures

List of Tables

CHAPTER ONE

Introduction and Background

1.1. Background and Significance

Since the early twentieth century, technological advances have had a major impact on diagnostic tools, therapeutic approaches, and instrumentation in the field of cardiology. However, despite all the progress achieved in medical sciences, cardiovascular diseases are still the leading cause of mortality and morbidity in the industrialized world. From micro to macro, our limited understanding of the heart's function continues to represent an obstacle to our ability to design strategies for proper detection and effective treatment of cardiac dysfunctions. Thus, the major challenge in solving the problem of dysfunctions in the cardiovascular system arises mainly from an inadequate understanding of the basic mechanisms governing the function of the system itself.

As an example, heart failure is now recognized as a major, growing, public health problem in both industrialized and developing countries, mainly affecting the elderly population. It has been reported that 4.8 million people in the United States suffer from congestive heart failure (CHF) [1]. Every year 500,000 new cases of CHF are diagnosed[1] and 274,000 people die due to its complications[2]. Despite significant advances in the treatment of heart failure, mortality rates still remain high: 30 to 40 percent of patients with advanced disease, and 5 to 10 percent of patients with mild symptoms die within 5 to 10 years[3]. Any effort to describe the epidemiology, etiology, and prognosis of heart failure, however, must consider the difficulty in precisely defining the nature of heart failure[4]. The term "heart failure" does not mean that the heart has failed; it simply implies that the heart does not pump as effectively as it should and is not working efficiently enough to meet the body's needs for oxygen-rich blood.

1.2. Diastolic Heart Failure

Heart failure (HF) can arise from any condition that compromises the *contractility* of the heart (systolic heart failure), or that interferes with the heart's ability to *relax* (diastolic heart failure). Hospital- and community-based reports indicate that around one-fourth to one-half of patients with congestive heart failure (CHF) suffer from diastolic HF, and the rest suffer from systolic HF[5]. However, diastolic HF may also lead to an accompanying systolic HF[6].

Diastolic heart failure is a clinical syndrome characterized by the symptoms and signs of left heart dysfunction[*], a preserved ejection fraction[†] (EF), and an increased diastolic filling pressure. From a conceptual perspective, diastolic heart failure occurs when the ventricular chamber is unable to accept an adequate volume of blood during diastole at

---

[*] e.g., Exertional dyspnea, paroxysmal nocturnal dyspnea, orthopnea, jugular venous distention, crackles, a displaced apical impulse, extra heart sounds S_4 and S_3, etc.

[†] $EF(\%) = \frac{LVEDV - LVESV}{LVEDV} \times 100$: *LVEDV*: Left Ventricular End Diastolic Volume; *LVESV*: Left Ventricular End Systolic Volume. Preserved EF implies that EF >45%.

normal diastolic pressures and at volumes sufficient to maintain an appropriate stroke volume. These abnormalities are initiated by a decrease in ventricular relaxation and/or an increase in ventricular stiffness (decreased compliance)[7].

1.3. Current techniques to evaluate Diastolic Dysfunction

Echocardiography[‡] is a valuable, non-invasive tool that employs Doppler principles for imaging the heart and its surrounding structures. In general, echocardiography refers to the process of imaging the heart with ultrasound, and is used to evaluate cardiac chamber size, wall thickness, wall motion, valve configuration and motion, and the proximal great vessels. By using the ultrasound technique, anatomic relationships or disorders (e.g. septal defects, valve incompetency, etc) can be identified and some information regarding cardiac function (e.g., blood flow) can also be deduced.

Normal trans-mitral blood flow is laminar and relatively low in velocity (usually less than 100 cm/sec). There is an early diastolic flow velocity, caused by the sustained myocardial relaxation, that results in an LV pressure below LA pressure which causes the mitral valve to open and rapid LV filling to occur (E-wave). The late component of diastolic flow is caused by atrial contraction at the end diastole, which pushes the remaining blood inside the LA into LV (A-wave).

[‡] For further information refer to the appendix.

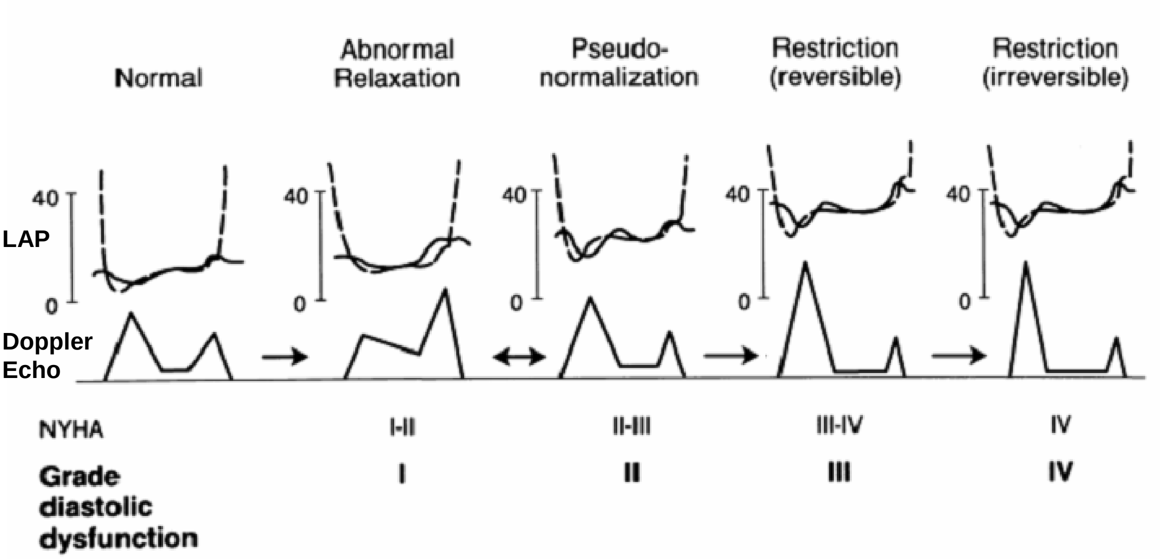

Figure 1.1. Progression of diastolic dysfunction. In a normal adult, LA pressure is around 2-5 mmHg, the peak E-wave is around 85 cm/s, and A-wave is around 45 cm/s. In the early stage of cardiac dysfunction, because of abnormal relaxation, LVP cannot drop efficiently, so E-wave (index of suction) drops, DT increases and A-wave (index of atrial contraction) increases to compensate the drop in E-wave. If no treatment starts at this stage, heart tries to compensate the suction effect by increasing the LAP. At this stage, E-wave, A-wave and DT look normal. This stage is critical because the changes are still reversible at this point. In the next stage, the ventricle stiffens, which leads to an increase in LVP and eventually an increase in LAP to compensate. At this stage E-wave is tall and A-wave shortens; in the final stage, the LAP increases to around 40mmHg and the ventricle has a very low compliance. Modified from "Nishimura RA, Tajik AJ. Evaluation of diastolic filling of left ventricle in health and disease: Doppler echocardiography is the clinician's Rosetta stone. *J Am Coll Cardiol* 1997; 30:8–18". *NYHA*: New York Heart Association classification; *LAP*: Left Atrial Pressure.

Normally, in left ventricular diastole, early (rapid) filling exceeds the atrial component of filling. Hence, the mitral inflow velocity profile shows that the E-wave is taller than the A-wave[§]. With impaired relaxation, the E component will be reduced, resulting in a lower E to A ratio. However, gradually, at some point, the left ventricle (LV) loses its compliance and the A component starts to diminish, resulting in a corrected E/A ratio while dysfunction is still progressing. Currently, assessments of diastolic dysfunction are based on classifications that assume progression from mild dysfunction [E/A under 1, isovolumic relaxation time (IVRT) over 100ms, normal E wave deceleration] to moderate disease [pseudonormalization; i.e. apparently normal E/A], to severe dysfunction

---

[§] For further information about E and A waves refer to the appendix.

[restrictive; i.e. large E and small A, short E deceleration of under 120ms, short IVRT, reduced pulmonary systolic wave][8].

Although the above progression may be common, it is, absolutely not predicTable. In some cases, either impaired relaxation [e.g. hypertrophic cardiomyopathy] or decreased compliance [e.g. restrictive cardiomyopathy] may prevail. With impaired relaxation, early filling is weakened. Conversely, with a restrictive pattern, the E to A ratio increases while early filling is quite normal. However, in cases where both types of dysfunctions are present, or in the transition period between mild to moderate disease, a *pseudonormalization*[9] occurs that prohibits further deterioration of diastolic function from appearing in E to A ratio changes (Figure 1.1).

This type of confusion, which arises from using existing ultrasonic indices for the diagnosis of diastolic failure, leads us to underestimate the progress of dysfunction. During the conversion of diastolic dysfunction from mild to severe stages, pseudonormalization hides the progress of the disease in the moderate stage and, therefore, the E to A wave ratio acts as a false indicator (Figure 1.1).

1.4. Vortex Formation and Force Generation

The presence of vortical structures that develop along with a strong propulsive jet during normal LV diastole was initially recognized by *in-vitro* visualization of the ventricular flow[10,11] and subsequently confirmed by analyses based on color Doppler mapping[12] and Magnetic Resonance Imaging (MRI)[13,14].

Thus, physical characteristics of these vortical flow structures may provide a better understanding of physiological events related to diastolic functionality and may also result in more effective indices of diastolic function than existing methods. So far, the process of vortex ring formation and its influence on dynamics of the left heart has not been elucidated.

The topic of vortex rings, such as those observed in the LV during diastole, has received much attention over the past few years, as evidenced by the growing number of publications on this issue. The current understanding of the formation process and dynamics of laminar and turbulent vortex rings has been discussed in a review by Shariff and Leonard[15] and recent works of Gharib group[16,17,18].

Vortex rings typically develop from a starting jet-- a jet or pulse of fluid ejected into quiescent surroundings. The characteristic stroke ratio of a starting jet is identified as the ratio of the ejected jet length to the effective jet diameter $\left(L/D\right)$. Gharib, Rambod and Shariff (GRS)[16] discovered that by increasing the starting jet stroke ratio beyond a certain range (~3.5-4.5), no additional energy or circulation enters the leading vortex ring, and the remaining fluid in the pulse is ejected as a trailing jet. After this stage, the vortex ring is said to have pinched off from the generating jet and the size of the leading vortex ring can no longer be increased (Figure 1.2). GRS defined the vortex formation time at which pinch-off process occurs as the "formation number":

$$\left(F = \frac{L}{D} = \frac{\overline{U}_p t}{D}\right)_{pinchoff}{}^{**} \qquad (1\text{-}1)$$

[**] Note that $\boldsymbol{F}$ is a dimensionless parameter. $\overline{U}_p$ is the average piston velocity and $\boldsymbol{D}$ is the piston diameter.

GRS also experimentally demonstrated that regardless of jet velocity and circular nozzle size, the formation number at which maximum circulation is attained in a vortex ring would be in the range of 3.6 and 4.5. The narrow range of formation numbers, observed in various situations suggests that the formation number can be used as a robust parameter for describing formation of a vortex ring. Regardless of the actual value of the formation number, no additional circulation or energy enters a pinched-off vortex ring[16]. It has also been shown by Krueger and Gharib[17] that the time-averaged force generated by a pulsed jet is maximized near the conditions that create vortex rings of maximum circulation (Figure 1.3).

In other words, once the stroke ratio of a pulse is large enough to pinch off the leading vortex ring and initiate formation of the trailing jet flow, an additional increase in stroke ratio does not increase the time-averaged force unless it does so at the expense of efficiency. Krueger and Gharib emphasized the importance of the formation of a single leading vortex ring created by starting jets for efficient generation of force, showing that a trailing jet plays a less important role in the process.

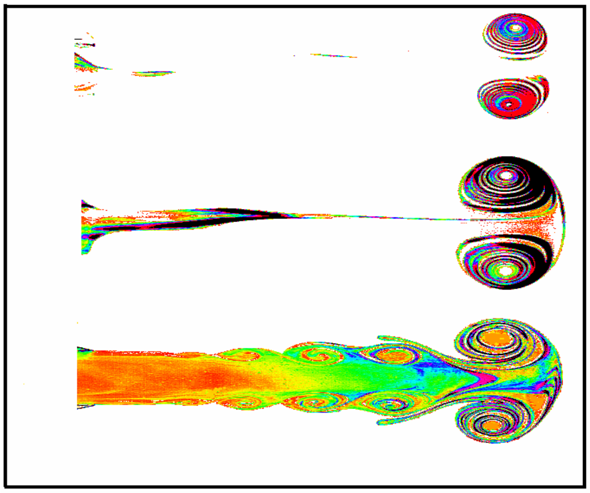

Figure 1.2. Vortex ring visualization. Visualization of vortex rings at $L/D \cong 9$ for (*a*) $L/D = 2$, $Re=2800$; (*b*) $L/D = 3{:}8$, $Re= 6000$; and (*c*) $L/D =14{:}5$. For further information refer to reference 16. Gharib M, Rambod E, Shariff K. A universal time scale for vortex ring formation. *J. Fluid Mech*: 121-140 APR 10, 1998

In a recent experimental study, Dabiri and Gharib[19] modified the definition of formation time in vortex generators with temporally variable nozzle diameter, such as the mitral apparatus. In this more general definition, instead of using the averaged exit velocity and a constant diameter, they averaged the proportion of instantaneous exit velocity and exit nozzle diameter multiplied by the pulse duration:

$$T^* = \int_0^t \frac{U_e(\varsigma)}{D_e(\varsigma)} d\varsigma = \overline{\left(\frac{U_e}{D_e}\right)}.T \quad (1\text{-}2)$$

where U_e and D_e are instantaneous exit velocity and opening diameter, respectively, and T is the pulse duration. It was shown that this dimensionless time-scale properly accounts for the effect of a time-dependent exit opening diameter. Thus, it removes the ambiguity which arises from using the maximum or averaged mitral valve exit diameter. The characteristics of a pulsed jet are sensitive to the time-dependent pressure gradient that initiates the starting flow. Therefore, a potential way to better describe the trans-mitral jet is to relate the vortex ring resulted from the trans-mitral jet to the diastolic pressure gradient that initiates the flow in early diastole.

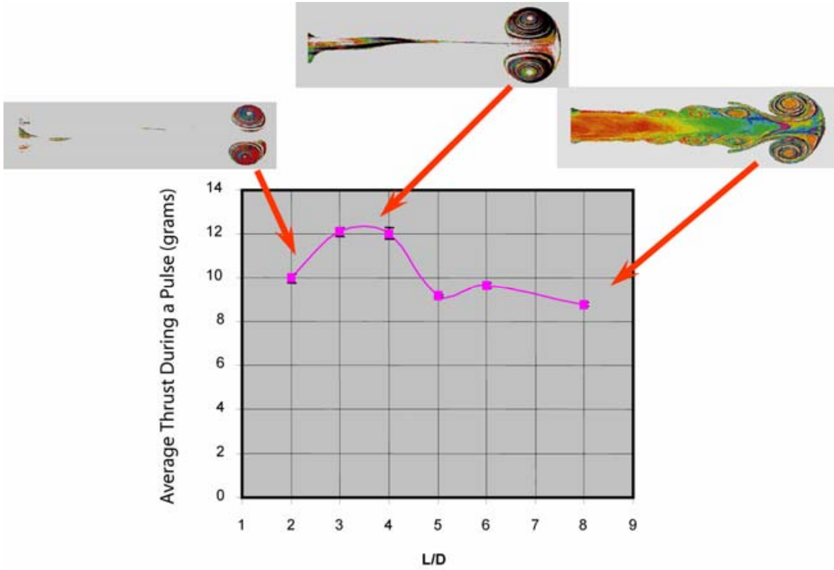

Figure 1.3. **Average thrust per pulse measurements**. It has been observed that the averaged thrust per pulse is maximized for L/D in the range of 3-4. For further information refer to reference (17) Krueger PS, Gharib M. The significance of vortex ring formation to the impulse and thrust of a starting jet. Physics of *Fluids* 15 (5): 1271-1281.

1.5. LV Diastolic Pressure

The end of systole occurs when the cardiac muscles undergo relaxation. By comparing left ventricular pressure (LVP), aortic pressure, aortic flow, dP/dt and ECG in open-chest dogs, Abel[20] showed that the maximal negative dP/dt (i.e., maximal rate of ventricular relaxation) corresponds closely to the end of ventricular systole, which is defined by stoppage of the forward flow in the ascending aorta. Weiss, et al[21] demonstrated that the time course of the left ventricular pressure-drop in isovolumic relaxation phase – after maximum negative dP/dt – can be regressed to an exponential function. This exponential time course of LV pressure drop during isovolumic relaxation phase (IVR) allows characterizing this phase by the time constant of the exponential function τ:

$$P = P_0 \exp(\frac{-t}{\tau}) \qquad (1\text{-}3)$$

where P_0 is the pressure at the initiation of the pressure drop and τ is the pressure drop time-constant which is a measure of LV suction. Yellin, et al[22] discovered that in a completely isovolumic non-filling cycle, the ventricle often relaxes to a negative minimum pressure (i.e., a state of suction). They modified the above mono-exponential equation as a more general form:

$$P = (P_0 - P_\infty)\exp(\frac{-t}{\tau}) + P_\infty \qquad (1\text{-}4)$$

where P_∞ is the pressure asymptote. In addition, Hori, et al[23] demonstrated the existence of an inverse relationship between the end systolic volume and the maximum negative diastolic pressure in the intact canine heart. They concluded that ventricular suction exists under physiological conditions and plays an important role in diastolic filling, particularly during exercise and tachycardia[††], while more blood needed to be ejected during systole.

During the course of diastolic dysfunction, as well as in the process of normal aging[24], a profound shift in the pattern of left ventricular filling occurs. Patients display a prolonged isovolumic relaxation time (IVRT), a marked reduction in the early diastolic filling rate (E-wave), a more gradual deceleration of early filling and an augmentation of the atrial component of the filling (A-wave)[25]. It has been presumed that these changes in filling dynamics result primarily from the slowing rate of LV pressure drop, manifested in the intact heart by prolongation of the time-constant of pressure drop (τ)[26,27]. We also showed that the pressure drop during the isovolumic relaxation phase at different chronological stages of cardiac remodeling followed by myocardial infarction (MI), changes to compensate for diastolic dysfunction [28].

1.6. Vortex Formation Time as a coupling parameter between Diastole and Systole

Diastolic dysfunctions, in steps that precede complete diastolic failure, are reflected in the dynamics of trans-mitral blood flow during early diastole (i.e. during the E-wave). The aim was to determine whether vortex formation time resulting from trans-mitral flow and valve kinematics can be used as a global parameter to identify the impairment of LV diastolic function at different stages of disease.

Diastole and systole are coupled to each other by the fact that the total volume of blood ejected during systole is originally received from the atria during diastole. Considering

---

[††] A rapid heart rate, usually defined as greater than 100

this coupling, one should also be able to establish a quantitative relationship between these two phases. In this section, vortex formation time as an index for trans-mitral flow during early diastole, and the ejection fraction (EF) as the standard measure for the LV function, would be related to each other. The following derivation establishes this relationship:

The term “ejection fraction” refers to the proportion of stroke volume to the end diastolic volume:

$$EF = \frac{LVEDV - LVESV}{LVEDV} \quad (1\text{-}5)$$

where *LVEDV* and *LVESV* are the Left Ventricular End-Diastolic and End-Systolic Volumes, respectively:

$$EF \times LVEDV = LVEDV - LVESV = STROKE\ VOLUME\ (SV) \qquad (1\text{-}6)$$

Stroke volume can also be written as:

$$SV = V_E + V_A = \overline{U}_E.T_E.\frac{\pi}{4}\overline{D}^2 + \overline{U}_A.T_A.\frac{\pi}{4}\overline{D}^2 \qquad (1\text{-}7)$$

where V_E and V_A are the volume contributions of E and A waves in ventricular filling, $\overline{U}_E$ and $\overline{U}_A$ are averaged velocities during E and A waves, and $\overline{D}$ is the averaged opening diameter of mitral valve. Multiplying both sides by $\frac{4}{\pi.\overline{D}^3}$:

$$SV \times \frac{4}{\pi.\overline{D}^3} = (\overline{U}_E.T_E.\frac{\pi}{4}\overline{D}^2 + \overline{U}_A.T_A.\frac{\pi}{4}\overline{D}^2) \times \frac{4}{\pi.\overline{D}^3} \qquad (1\text{-}8)$$

or

$$\frac{4}{\pi.\overline{D}^3} \times (EF \times LVEDV) = \frac{\overline{U}_E.T_E}{\overline{D}} + V_A \times \frac{4}{\pi.\overline{D}^3} \qquad (1\text{-}9)$$

Considering formation time from (1-1) as $T^* = \dfrac{\overline{U}_E . T_E}{\overline{D}}$, the equation (1-8) can be reorganized as:

$$T^* = \frac{4}{\pi.\overline{D}^3} \times (EF \times LVEDV) - \frac{4}{\pi.\overline{D}^3} \times V_A \qquad (1\text{-}10)$$

or

$$T^* = \frac{4}{\pi.\overline{D}^3} \times (EF \times LVEDV) \times (1 - \beta) \qquad (1\text{-}11)$$

where β is the percentage of stroke volume that corresponds to contribution of atrial contraction in LV filling and can be measured with ultrasound modalities. By defining $\alpha \equiv \dfrac{\sqrt[3]{LVEDV}}{\overline{D}}$, the equation (1-11) can be rewritten as:

$$T^* = \frac{4(1-\beta)}{\pi}.\alpha^3.EF \quad (1\text{-}12)$$

In a normal heart at rest, $V_A = 0.20 \times SV$ or $\beta = 0.20$. Therefore, the formation time at rest in a healthy heart can be computed as:

$$T^* = \frac{4 \times 0.80}{\pi.\overline{D}^3}.\alpha^3.EF \quad (1\text{-}13)$$

From (1-13), one can obtain variations of formation time as a function of ventricular geometric parameter (α) for different values of EF. For example, the solid line in Figure 1.4 shows that for EF=0.65, the formation time for E-wave increases along with α. Computing α based on normal human heart values for $LVEDV$ and the averaged diameter for the same heart[29] would result in a range of 1.7 and 2 for α. This curve shows that during a normal diastolic function, the E-wave phase is completed within a formation time ranging between 3.3 and 5.5, similar to the optimal range found in previous vortex ring studies[16,17]. Likewise, one can reach the conclusion that for a reduced EF (≈0.3), as is the case for an end-stage systolic heart failure, the formation time range drastically drops to 1.5-2.5[29]. This result predicts that the derived vortex formation time index can even discern the occurrence of the type of LV dysfunctions that appear in the value of EF (systolic dysfunctions).

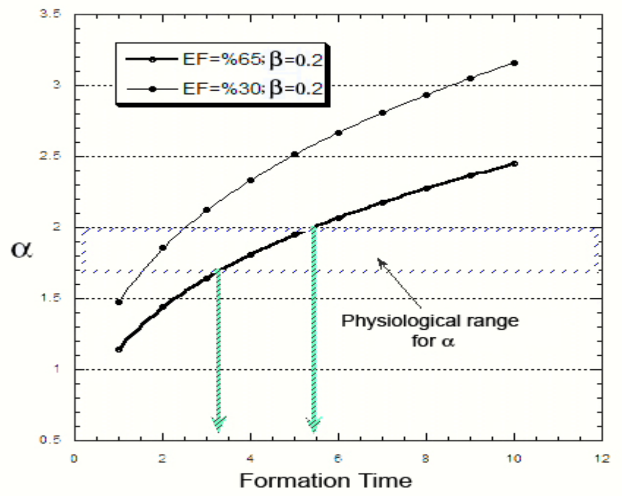

Figure 1.4. The relationship between formation time and geometrical factor (α). For the physiological ranges of α, formation time between 3.3 and 5.5 represents optimality for the normal heart, while a lower formation time range of 1.5-2.5 marks a reduced ejection fraction. Gharib M, Rambod E, Kheradvar A, et al. A global index for heart failure based on optimal vortex formation in the left ventricle. *Proc Natl Acad Sci* 2006 18;103(16):6305-8.

1.7. Preliminary Clinical Study

Two independent preliminary studies[30] were carried out at University of California at San Diego and at Caltech by Gharib's group. A total of 110 volunteers, between 5 and 84 years of age, were randomly selected, for both studies, to undergo trans-thoracic echocardiography (TTE) for imaging the left ventricle from the apical view.

To evaluate the LV diastolic filling and its relationship to the trans-mitral velocity profile, the maximum diameter of mitral annulus ($D_{\max}$) was measured from the long-axis apical view using ultrasound M-mode Doppler. The distance from mitral annulus to the cardiac apex (L) was also obtained from the 2D echo images. Mean trans-mitral velocity ($\overline{U}_E$)

was obtained by pulsed-wave (PW) Doppler in the immediate downstream vicinity of mitral valve leaflets. Formation time was computed for each case based on an approximate definition:

$$T^* = \frac{\overline{U}_E T_E}{D_{max}} \quad (1\text{-}14)$$

Figure 1.4 shows the distribution of formation time versus age for both groups between the age of 5 and 84. The large, red squares mark the data for volunteers with DCM. A power curve-fit was used for the non-DCM cases, which shows that in adults [older than 20 years of age], distribution of formation time converges to a unique range of values between 3.5 and 5.0. In this plot, formation numbers for DCM cases are generally located below this range (Figure 1.5). A likely source of scatter in this preliminary data is derived from the use of the approximate definition for vortex formation time, which incorporates the maximum mitral valve exit diameter rather than the time-dependent diameter, as is discussed in the present proposal. Based on the previous experiments, a new protocol is suggested for the clinical validation study, which is described in appendix (A.3.).

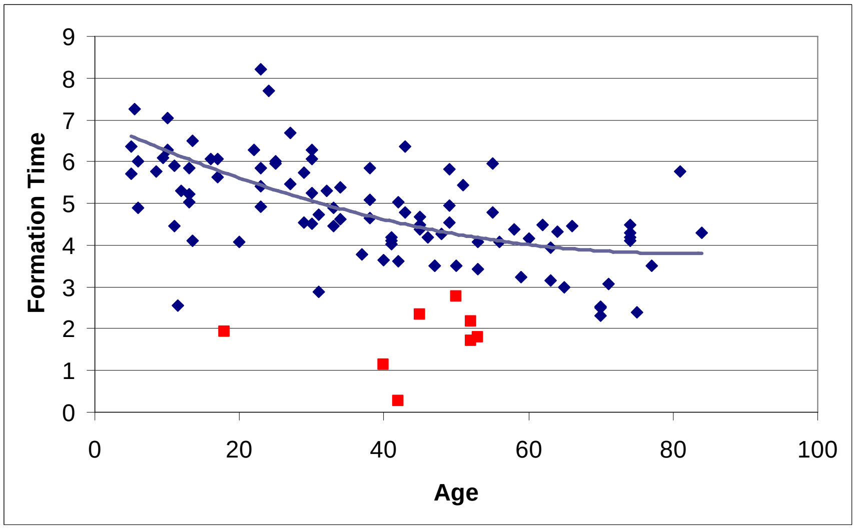

Figure 1.5. Distribution of formation time versus age. Blue dots represent normal population and red spots represent DCM cases. Note that the curve is only fitted to the normal data.

1.8. Objectives

The flow inside the left ventricle represents one of the most interesting problems in biological fluid dynamics, depending on its relevance on the global functionality of the heart pump. Due to the complexity of the relationship between left ventricular (LV) filling and ejection, the diastolic function must be contemplated for the assessment of global LV systolic function. Impairment of diastolic filling may result in a reduced pump function. One of the most important fluid phenomena involved in the left ventricular diastolic flow is related to the presence of vortical structures that develop with the strong jet that enters through the mitral valve.

The importance of vortex ring formation and the pinch-off process to propulsion rests on the relative contribution of the leading vortex ring and the trailing jet to the impulse supplied to the flow. The relationship between the vortex ring formation and the impulse supplied to the flow by individual starting jet during diastole seems to be particularly important. One of the main goals of the present study is to relate the vortex pinch-off process and the LV pressure drop during diastole. Our hypothesis is that the vortex formation time as a global non-dimensional index can be used to quantify diastolic function, regardless of other patient-dependent factors [e.g. sex, heart size, etc.], and can be used to improve our ability to predict the process that leads to diastolic failure.

The events in early diastole can be summarized as the untwisting process that drops the pressure in the LV[31], eventually leads to release of potential energy stored during systole, and finally results in the response of the LV to this pressure drop[32]. The response of the LV to the sudden pressure drop begins with the mitral valve opening, blood transfer from the atrium through the mitral valve, and ends up with the upward movement of cardiac base [mitral annulus plane] as a reaction to the blood jet.

Disease-related dysfunctions in each step of the above-mentioned process are reflected in the dynamics of trans-mitral blood flow during early diastole. However, variations in early trans-mitral blood flow can influence the vortex formation process in the ventricle. Therefore, the vortex formation number as a parameter related to the hemodynamics of early diastolic blood flow can be developed and used as a global index to characterize the state of diastolic function [i.e., suction and mitral valve dynamics].

Conventional measurements that reflect changes in normal diastolic function generally depend on patient-specific indices like the onset, rate, and extent of ventricular filling and pressure decline; pressure-volume or stress-strain relationships during diastole; and relations between E and A waves[33]. Indeed, ultrasonic measurements of existing blood flow indices cannot be interpreted correctly without a prior knowledge of gender, heart size, etc., besides the confusion of the current technique in diagnosing moderate HF. Other measurements, like intraventricular pressure and stress-strain relationships, are more difficult to obtain and cannot be made non-invasively. Moreover, since these conventional indices usually do not show a significant change until the heart is seriously dysfunctional[34], their effectiveness is limited.

Little has been done to experimentally measure the exerted force on the base of the heart due to blood jet in diastole, which leads to axial (upward) displacement of the mitral annulus. The major obstacles to this kind of experimentation are uncertainty about the origin of the resulting force and lack of a global model to describe the complex dynamics resulting from interaction between tissue and blood in cardiac chambers. Considering the partial contribution of the blood jet in generating force, and studying the relationship between various vortex formation conditions and the magnitude of the force *in-vitro* and *in-vivo*, could result in a better understanding of the complex dynamics of diastole, as well as the discovery of the conditions in which the diastolic phase is optimized.

The general objective of this thesis is to develop a better understanding of the role of trans-mitral blood flow in the heart by relating the vortex formation process to other hemodynamical factors that influence diastolic function in early diastole. Implementing novel diagnostic criteria which detect early diastolic dysfunctions will save millions of lives.

CHAPTER TWO

Correlation between Vortex Ring Formation and Mitral Annulus Dynamics during Ventricular Rapid Filling[‡‡]

2.1. Chapter Abstract

One of the most important fluid phenomena observed in the left ventricle during diastole is the presence of vortex rings that develop with a strong jet entering through the mitral valve. The present study is focused on the rapid-filling phase of diastole, during which the left ventricle expands and receives blood through the fully-open mitral valve. The atrio-ventricular system during rapid-filling phase was emulated experimentally with a simplified mechanical model, in which the relevant pressure decay and the dimension of mitral annulus approximate the physiological and pathological values. DPIV measurements were correlated with the force measurements on mitral annulus plane to analyze the relationship between the flow and the mitral annulus motion. The recoil force on the displaced annulus plane was computed based on the plane's acceleration and velocity, and correlated with the in-flow jet. Measurements of the recoil force for different values of the mitral annulus diameter showed that the recoil force was generated during fluid propulsion and it is maximal for an annulus diameter close to the normal

---

[‡‡] ASAIO journal, in press (scheduled for publication in Jan-Feb 2007 issue)

adult value in a healthy left ventricle. We also tested annulus diameters smaller and larger than normal. The smaller annulus corresponds to the stenotic valves, and the larger annulus exists in dilated cardiomyopathy cases. In both conditions, the recoil force was found to be smaller than in the normal case. These observations are consistent with the previously reported results for dilated cardiomyopathy and mitral stenosis clinical conditions as mentioned in the text.

2.2. Introduction

The topic of vortex rings has received much attention over the past few years. Vortex rings occur in nature wherever propulsive flow exists, from those seen in erupting volcanoes to those generated by squid and jellyfish to propel them. They are also present in the left ventricle (LV). The current understanding of the formation process and dynamics of the vortex rings has been extensively described in the literature[15,16,35,,36]. However, the process of vortex ring formation and its influence on dynamics of the left heart have not been elucidated so far.

The presence of vortex rings that develop during cardiac diastole was initially recognized by *in-vitro* visualization of the ventricular flow[10,11] and subsequently confirmed by analyses based on color Doppler mapping[12,37] and Magnetic Resonance Imaging[13,14]. During diastole, when the left ventricle is filling with the blood jet from the atrium, the ventricle expands and, as a result, the atrio-ventricular plane moves in opposite direction with respect to the blood flow. Little has been done so far to understand if any correlation exists between this movement and the formation process of the vortex ring created by the blood jet.

Vortex rings typically develop from a jet, or slug of fluid, ejected from a nozzle. In fluid mechanics, mitral inflow is considered a starting jet ejected from left atrium to the left ventricle. The characteristic stroke ratio of a starting jet (L/D), typically produced by a piston-cylinder mechanism, is identified as the ratio of the ejected jet length ($L = \int_T u_{piston}(t)dt$; where "$u_{Piston}$" is the piston velocity, "t" is time and "T" is the period of piston displacement) to the effective jet diameter (D). This ratio is usually referred to as *formation time*[16,38,39] and is a non-dimensional measure of time. Gharib, Rambod and Shariff (GRS)[16] discovered that by increasing the stroke ratio of a starting jet to values greater than 4, in semi-infinite space, no additional energy or circulation enters the leading vortex ring and the remaining fluid in the pulse will be ejected as a trailing jet. After this stage, the vortex ring is said to have pinched off from the starting jet, and as a result, the size of the leading vortex ring can not increase. The value of the stroke ratio (formation time) at which pinch-off occurs is recognized as *vortex formation number*. GRS experimentally showed that regardless of the jet velocity and the nozzle size in a semi-infinite space, the formation number lies between 3.6 and 4.5[16].

In a different experimental study, Krueger and Gharib[17] showed that the time-averaged thrust generated by a pulsed jet in semi-infinite space would be maximized, once a vortex ring with maximum circulation is created. In other words, once the stroke ratio of a pulsed jet is large enough to pinch off the leading vortex ring and initiate formation of the trailing jet flow, further increase in stroke ratio does not increase the time-averaged thrust. Krueger and Gharib[17] emphasized that formation of a single leading vortex ring has a more significant role in efficient generation of thrust, when compared to the trailing jet.

In this study, we examined the formation of a vortex ring in a confined chamber, in contrast to previous studies done in a semi-infinite space. The objective was to understand the dynamics of mitral annulus plane and its correlation to trans-mitral flow, using vortex ring formation as an index. To study this, we chose a simplified system to experimentally simulate the contribution of the vortex ring on the dynamics of the annulus plane.

In a normal ventricle, the annulus plane motion is mainly a consequence of compliance effect and passive stiffness of myocardium. However, the compliant walls of the ventricle would affect generation of a vortex ring along with the trans-mitral jet by dropping the LV pressure [suction effect] during diastole[40], and would literally interact with the formed vortex[41]. As a result, we chose to generate a vortex ring using an exponential pressure drop, mimicking the suction in the left ventricle[21,22,42] while carefully avoiding the influence of other factors.

In this study, the annulus is circular in shape, whereas the mitral annulus is oval-shaped, and contains leaflet structures that interact with the flow. However, incorporating leaflets without knowing the behavior of the system with no valves makes the interpretation of the results more difficult. Since no valve is used in this study, we only consider the effect of suction on the generating jet, once the mitral valve is fully open.

2.3. Methods

The experimental setup was a simplified analog of the left heart during rapid filling phase of diastole. In early diastole, pressure decays quickly in the left ventricle, the mitral valve opens immediately in response to pressure drop, allowing blood transfer from atrium to ventricle, and finally, the valve plane moves in the opposite direction with respect to blood flow. To be consistent with cardiac physiology, the LV pressure drop in early diastole was modeled as a decaying exponential function with pressure drop time constant (τ)[21] in physiologic range.

2.3.1. Experimental setup components

The experimental setup was comprised of two chambers partially filled with water; the nominal ventricle was built as a Plexiglas chamber connected to a suction pump (VSI SPS3891, *Vivitro Systems Inc*) to generate pressure drop, and the nominal atrium was a cylindrical tube sitting inside the ventricular chamber, as shown in Figure 2.1. Dimensions of the ventricular box were 13cm (width) by 13cm (depth) by 20cm (height), although, only the lower 13cm of the box was filled with fluid (Figure 2.1). The base [annulus plane] to apex distance was set to 9cm which is the same as the base-apex distance in LV, as mentioned in medical literature[43,44]**.** The fully-open mitral annulus was experimentally simulated as a flat plate with a circular annulus, which was made of neutrally buoyant Plexiglas to avoid any behavior influenced by difference in density. Additionally, to prevent the effect of mass transfer on annulus-plane dynamics, a low flow resistant pneumatic check-valve (R-702, *Resenex corp.* Chatsworth, CA) was placed on the ventricular chamber. The mass of fluid entering from the atrial tube pushed the trapped air in the ventricular chamber out of the box through the check-valve, avoiding mass transfer effect.

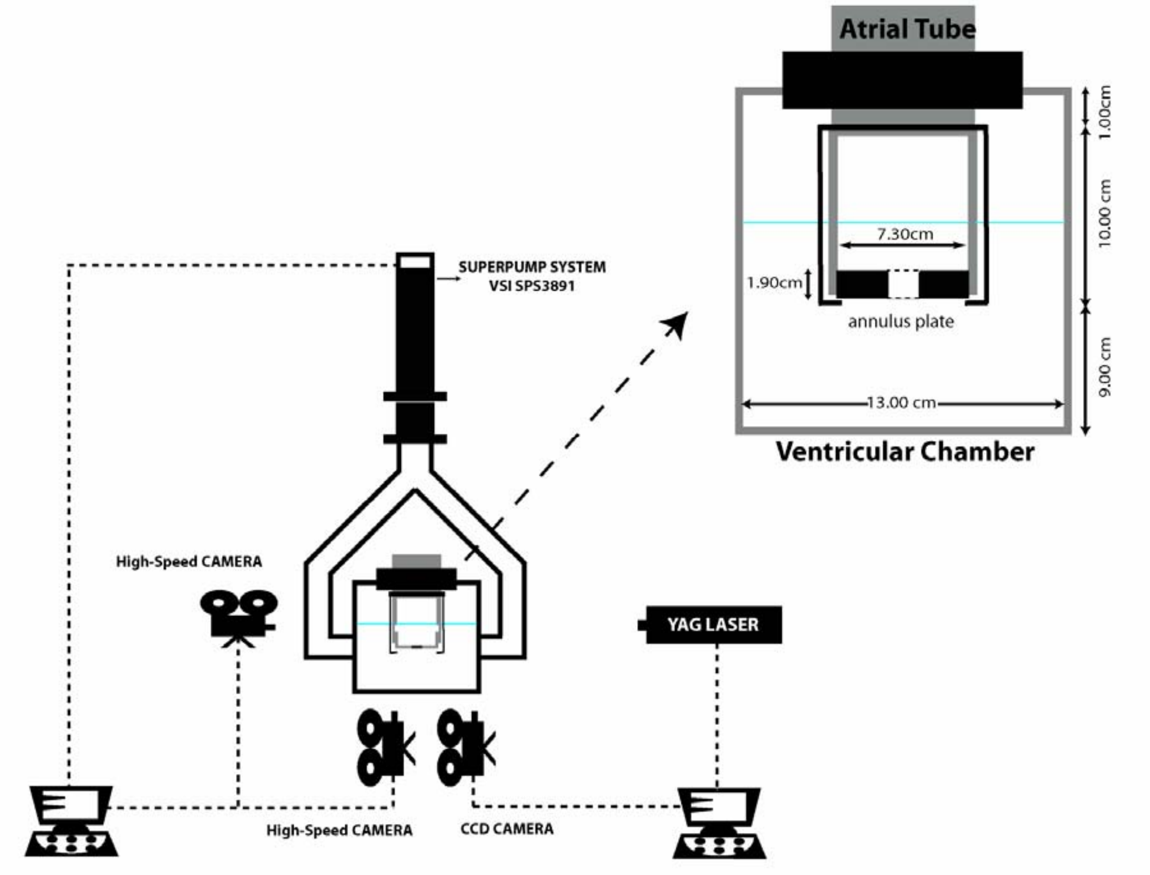

Figure 2.1. Schematics of the experimental setup. The experimental setup was comprised of two chambers partially filled with water; the nominal ventricle was built as a Plexiglas chamber connected to a suction pump to generate pressure drop, and the nominal atrium was a cylindrical tube sitting inside the ventricular chamber, as shown in Figure 1. Dimensions of the ventricular box were 13cm (width) by 13cm (depth) by 20cm (height), although, only the lower 13 cm of the box is full. The base [annulus plane] to apex distance was set to 9cm. two high speed cameras track the water level velocity and the annulus plane motion. Flow was illuminated by a 25mJ double pulsed Nd:YAG laser with the pulse separation of 1ms. A high-resolution monochrome CCD digital camera was positioned perpendicular to the ventricular chamber to capture the image sequences of the particle field.

To reproduce the movement of the valve plane during early diastole, the annulus-plane was allowed to slide in the downstream end of the atrial tube without friction. Three L-shaped rods prevented the plate from falling into the ventricular chamber. The LV pressure drop was reproduced by using a computer-controlled suction pump. The considered range for pressure drop time-constant was within the physiologic limits[25,45] and the volume of ejected fluid was set to 50ml, which is equivalent to the volume of blood transferred into the human LV during early diastole[46].

Table 2.1. Abbreviations and acronyms

P	Trans-annulus pressure
P_0	Initial ventricular pressure
P_{LV}	Ventricular pressure
P_∞	Pressure at atrial side of the nozzle
τ	Pressure drop time-constant
V	Volume of fluid passes the annulus
U_J	Instantaneous exit jet velocity
U_A	Water-level velocity at the atrium
U_P	Annulus-plane velocity
u_{Piston}	Piston velocity
D_J	Annulus diameter
D_A	Atrial tube diameter
ρ	Water density
V_A	Volume of fluid in atrium
V_0	Initial volume of fluid in atrium
x_0	Initial position of water level in atrium
x	Instantaneous position of water-level
T^*	Formation time
t	Time
m	Mass of the annulus plane plus the atrial fluid
g	Gravitational acceleration
a_P	Annulus plane acceleration
$M_{Annulus}$	Mass of the annulus plane
L_A	Ejecting height of water-level at atrium
L_J	Nominal ejected jet length
Γ	Circulation
ω	Vorticity

Both chambers and the sliding annulus plane were made out of Plexiglas to facilitate flow visualization and annulus-plane motion measurements.

2.3.2. Reproduction of early diastole

For each experiment, both atrial and ventricular chambers were set to have atmospheric pressure. To reproduce the sudden pressure drop in early diastole, the suction pump created a rapid pressure difference between the water inside the cylindrical atrium and the water inside the ventricular chamber. Three different sizes for annulus diameter were used to experimentally simulate different flow conditions. For all the considered cases, the pump was set to displace a constant volume of fluid (50ml) while the pressure drop scheme and the initial water height in the system were kept the same. The pressure inside the ventricular chamber and trans-annulus pressure were measured with a real-time pressure monitoring system during the experiment (Deltran DPT-400 pressure transducers and VSI-TP8891 *Vivitro Systems Inc*). For accuracy of measurement and to make sure that the obtained results were reproducible and consistent with each other, every set of the experiment ran in 20 consecutive cycles. For each single cycle, the LV pressure was forced to decay as an exponential function in response to the applied suction:

$$P_{LV} = P_0 \exp\left(\frac{-t}{\tau}\right) \quad (2\text{-}1)$$

where P_0 is the initial pressure set to atmospheric value, τ is the pressure drop time-constant and adjusted to be 35±5 milliseconds and t is time. The duration of each cycle was set to 100ms[47,48,49] imitating the duration of rapid filling phase of diastole (E-wave).

2.3.3. Measurement methods

Displacement of the water level inside the atrial tube was captured using a high-speed camera (Photron FASTCAM-Ultima APX, *PHOTRON USA, INC***.** San Diego, CA) at 250 frames per second. The water level velocity was computed by finite difference based on the measured water-level displacement data. Applying continuity equation and considering a uniform profile for exit jet velocity over the annulus cross-section, trans-annulus flow rate computed as:

$$\frac{dV}{dt} = \frac{\pi}{4} D_A^2 .(U_A - U_P) = \frac{\pi}{4} D_J^2 (U_J - U_P) \quad (2\text{-}2)$$

where V is the volume of fluid going through the annulus, U_J is the instantaneous exit jet velocity, U_A is the water-level velocity at the atrium, U_P is the annulus plane velocity, and D_J and D_A are the annulus diameter and the cross sectional diameter of atrial tube, respectively. Instantaneous exit jet velocity (U_J) was computed as:

$$U_J(t) = \frac{D_A^2}{D_J^2} U_A(t) + (1 - \frac{D_A^2}{D_J^2}) U_P(t) \quad (2\text{-}3)$$

Displacement of the annulus plane was monitored by a second high-speed camera [duplicating the first camera, mentioned earlier]. The two cameras were synchronized to capture immediate changes in flow and the annulus plane dynamics. Mass of the fluid inside the atrial tube at each instant of time was computed as:

$$\rho \int dV_A = \rho (V_0 - \frac{\pi}{4} D_A^2 (x_0 - \int_{x_0}^{x} dx)) \quad (2\text{-}4)$$

where ρ is water density, dV_A is the fluid volume element at each instant of time, V_0 is the initial volume of the fluid in atrium, x_0 is the initial position of atrial water level with respect to the origin before starting the experiment, x is the instant position of water level and dx is atrial water-level position element at each instant of time with respect to the origin. Formation time (T^*) was computed based on the definition described by Gharib,[3] et al, as:

$$T^* = \frac{1}{D_J} \int_0^t U_J(\varsigma) d\varsigma \quad (2\text{-}5)$$

The flow characteristic information [e.g. velocity field and circulation] was captured by phase-averaged DPIV (Digital Particle Image Velocimetry)[50]. DPIV uses two digital images of a particle-seeded flow illuminated by a thin laser sheet to determine the displacement field of the particles in the field of view (sampling window), by cross-correlating pixels in a subsection of two images. A high-resolution monochrome CCD digital camera (30fps, 768x480; TM-9701, PULNiX America, Inc.) was positioned perpendicular to the ventricular chamber to capture the image sequences of particle field (Figure 2.1). Pairs of images were captured from an illuminated sheet of fluorescent particles generated by a 25mJ double pulsed Nd:YAG laser with the pulse separation of 1ms.

The length of each pressure-drop cycle was set to 100ms, as mentioned earlier. The CCD camera used for DPIV took 2 pairs of images in each cycle. There were 20 consecutive cycles which were identical because of the same pressure drop (τ=35±5) applied. DPIV data were phase-averaged over the 20 identical cycles. Therefore, a total of 40 velocity/vorticity fields were captured at different time points in the rapid filling phase. This temporal resolution gave us an accurate estimate of the velocity and vorticity fields and enabled us to compute circulation of the vortex rings as well as validate the exit jet velocity (U_J) obtained from a different method (2-3). The CCD camera was triggered simultaneously with the first cycle of the experiment and was synchronized with the *PHOTRON* high-speed cameras. The laser sheet was set perpendicular to the jet and cut through the center of annulus. This configuration allowed analysis of velocity and vorticity fields resulting from the starting jet at the illuminated cross-section.

Vortex ring circulation within its formation stages was computed using DPIV data (Figure 2.7). Based on saturation status of circulation, the onset of pinch-off was determined. Circulation (Γ) was computed based on the vorticity field (computed from velocity field) of each captured frame. Vorticity (ω) is defined as the curl of the velocity vector:

$$\omega = \nabla \times \mathbf{u} \qquad (2\text{-}6)$$

Circulation (Γ) is characterized as the line integral of the velocity. Based on Stoke's theorem, the circulation around a reducible curve (c) is equal to the flux of vorticity through an open surface (Λ) with unit normal vector "***n***" bounded by the curve, that is:

$$\Gamma = \oint_c \mathbf{u} dk = \int_\Lambda \omega.\mathbf{n} ds \qquad (2\text{-}7)$$

where the right side is a surface integral and the left side is a line integral, "***u***" is the velocity vector[51], *ds* is the surface element, and *dk* is the line element.

2.3.4. Control volume analysis

The momentum equation related to the setup was derived by considering the control volume (Ω) equations for the fluid inside the atrial tube (Figure 2.2). Flow was considered inertia dominant because of high Reynolds numbers at the annulus, and shear stress contribution to the momentum equation was neglected. Assuming constant gravitational field (*g*) acting on the control volume (Ω) with moving boundary, the momentum equation would be described as:

$$\frac{\partial}{\partial t}(m\mathbf{U_p}) + \rho \int_{\partial\Omega} \mathbf{U_J}((\mathbf{U_J} - \mathbf{U_p}).\mathbf{n}) ds = m\mathbf{g} + \int_{\partial\Omega} (P_\infty - P)\mathbf{n} ds \qquad (2\text{-}8)$$

where $\mathbf{U_J}$ is the instantaneous exit jet velocity, $\mathbf{U_P}$ is the annulus plane velocity and *m* is the mass of the annulus plane together with the instantaneous mass of the fluid:

$$m(t) = M_{Annulus} + \rho \int_{\Omega} dV_A(t) \qquad \text{(2-9)}$$

P is the pressure at the annulus and P_∞ is the pressure at the atrial side of the nozzle (Table 2.1). Based on the momentum equation (2-8), recoil force is described as

$$\mathbf{F_{recoil}} = \frac{\partial}{\partial t}(m\mathbf{U_p}) = M_{Annulus}\mathbf{a_p} + \rho \int_{\Omega} \mathbf{a_p} dV_A + \rho \frac{\partial}{\partial t} \int_{\Omega} \mathbf{U_p} dV_A \qquad \text{(2-10)}$$

where $\mathbf{a_P}$ is the annulus plane acceleration. Thrust generated by the propulsion is described from momentum equation as:

$$\mathbf{F_{thrust}} = \rho \int_{\partial\Omega} \mathbf{U_J}((\mathbf{U_J} - \mathbf{U_p}).\mathbf{n}) ds + \int_{\partial\Omega} (P - P_\infty)\mathbf{n} ds \qquad \text{(2-11)}$$

where **n** is the unit outward normal and *ds* is the area element. This study considered uniform profile for the flow over the annulus. The only external force that applied to the surface of control volume was the weight of annulus plane, together with the fluid at each instant of time. Considering the direction of forces (Figure 2.2), equations (2-8), (2-10) and (2-11) are summarized as:

$$\mathbf{F_{recoil}} - \mathbf{F_{thrust}} = m\mathbf{g} \qquad \text{(2-12)}$$

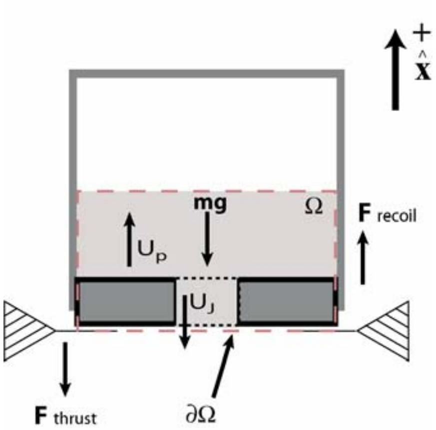

Figure 2.2. Embedded control volume (Ω) of fluid inside the atrial tube and at the annulus. U_J is instantaneous exit jet velocity, U_P is the annulus plane velocity, F_{thrust} is the force generated by thrust, F_{recoil} is the recoil force exerted on the annulus plane and *mg* is the weight of annulus plane plus instantaneous weight of water inside the atrial tube (over the annulus plane).

2.4. Results

2.4.1. Exit jet velocity and formation time

Exit jet velocity for each annulus diameter was computed based on equation (2-3) and is shown in Figure 2.3. Formation time was computed based on the instantaneous exit jet velocity (2-3) and the corresponding annulus diameter. For comparison purposes, all the results were shown as function of formation time, which is a non-dimensional time parameter[16]. For the largest annulus size (D_J =3.00 cm), velocity reached its maximum (108±8 cm/s) at *T*=0.97±0.3* and the trans-annulus flow ended at around *T*=2.00*. For D_J =2.50 cm, trans-annulus jet reached its peak velocity (188±10 cm/s) at *T*=2.00±0.2* and the flow ended prior to *T*=6.00*. Using the smallest annulus size (D_J =1.75 cm), trans-annulus jet velocity reached its maximum (287±11 cm/s) at *T*= 5.90±0.6* and the flow terminated around *T*=12.00* (Figure 2.3).

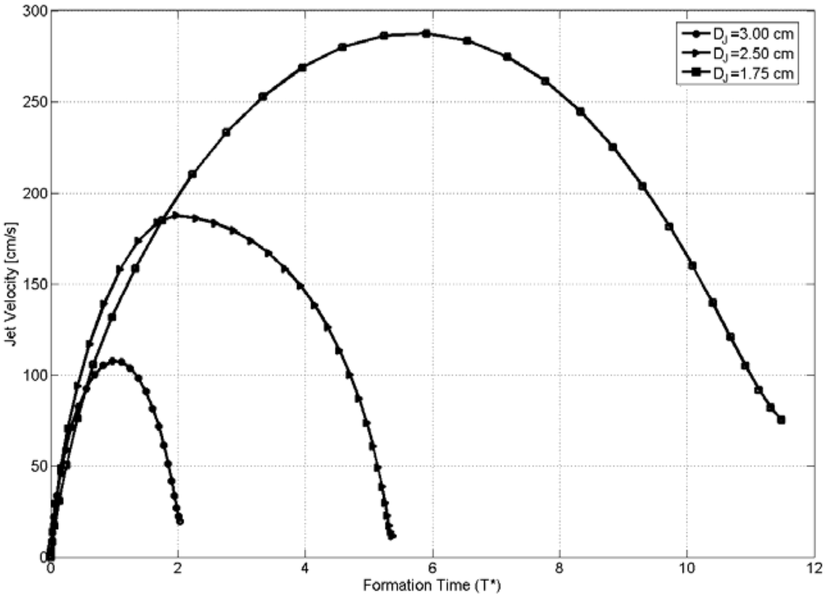

Figure 2.3. Exit jet velocity for each annulus diameter as function of formation time. For the largest annulus size case (D_J=3.00 cm), velocity reached its maximum (108±8 cm/s) at *T*=0.97±0.3* and the trans-annulus flow completed at around *T*=2.0.* For D_J=2.50 cm, trans-annulus jet reached its peak velocity (188±10 cm/s) at *T*=2±0.2* and the flow ended prior to *T*=6*. Using the smallest annulus size (D_J=1.75 cm), trans-annulus jet velocity reached its maximum (287±11 cm/s) at *T*=5.90±0.6* and the flow terminated around *T*=12.00*.

2.4.2. Trans-annulus pressure

Pressure difference between the atrial tube and ventricular chamber at the annulus (*P*) was measured during pressure drop in each cycle. The trans-annulus pressure normalized with the initial LV pressure (P_0) for each case plotted as function of formation time in Figure 2.4. For D_J=*3.00 cm*, pressure at the annulus dropped to 20 percent of its initial value at *T*=1.10±0.2.* The same extent of pressure drop occurred for D_J=*2.50 cm*, at *T*=2.30 ± 0.3* and for D_J=*1.75 cm*, at *T*=3.40 ± 0.3*.

2.4.3. Recoil force and thrust

For each annulus size, the velocity (U_P) and the acceleration of the annulus plane (a_P) were measured, and the recoil force (F_{recoil}) was computed based on momentum equation (2-8). The recoil force as function of formation time is shown in Figure 2.5 for each annulus size. For D_J *=3.00 cm,* recoil force reached its peak at *T*= 2.00±0.1*, for D_J *=2.50 cm*, the maximal recoil force was attained at *T*=3.8±0.2* and for D_J *=1.75 cm*, the forced had the peak at *T*=11.00±0.4* (Figure 2.5).

Force generated by the thrust (F_{thrust}) was computed based on exit jet velocity, annulus plane velocity and the pressure at the annulus (2-11). The magnitude of thrust can be compared with the recoil force in Figures 2.6 and 2.5. The thrust subtracted by instant weight of the atrial tube (*mg*) versus formation time is shown in Figure 2.6 for each annulus size. For D_J *=3.00 cm,* thrust reached its peak at *T*=2.00±0.1*, for D_J *=2.50 cm*, the maximal thrust was attained at *T*=5.0±0.4* and for D_J *=1.75 cm*, the forced had the peak at *T*=11.00±0.3* (Figure 2.6). The recoil force was computed based on equation (2-10) by tracking the annulus movement and trans-annulus flow with the high-speed camera.

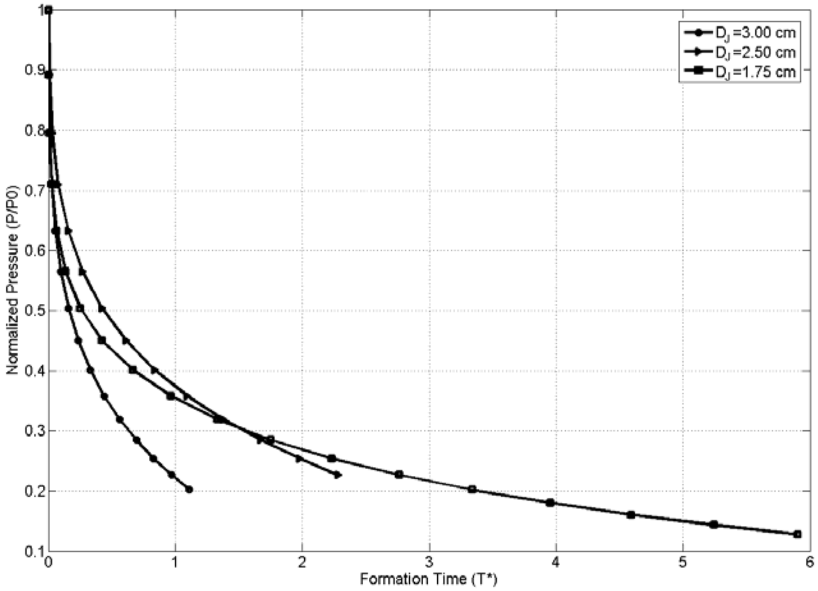

Figure 2.4. Trans-annulus pressure normalized with the initial LV pressure (P_0). For D_J *=3.00 cm*, pressure at the annulus dropped to 20 percent of its initial value at *T*=1.10±0.2*. For D_J *=2.50 cm*, pressure at the annulus dropped to 20 percent of its initial value at *T*=2.30± 0.3*. For D_J *=1.75 cm*, pressure at the annulus dropped to 20 percent of its initial value at *T*=3.40 ± 0.3*.

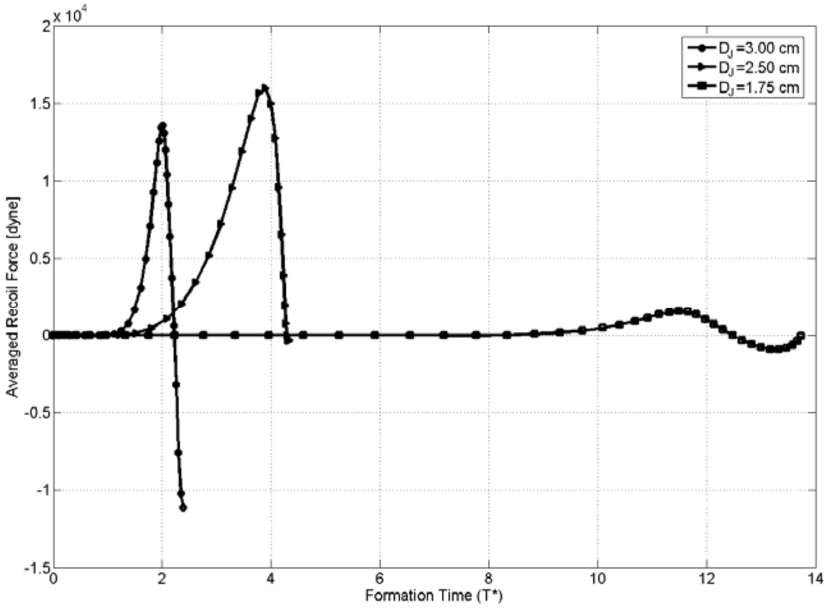

Figure 2.5. Time averaged recoil force for the considered cases. For D_J *=3.00 cm,* recoil force reached its peak at *T*= 2.00±0.1*, for D_J *=2.50 cm*, the maximal recoil force was attained at *T*=3.8±0.2* and for D_J *=1.75 cm*, the forced had the peak at *T*=11.00±0.4*.

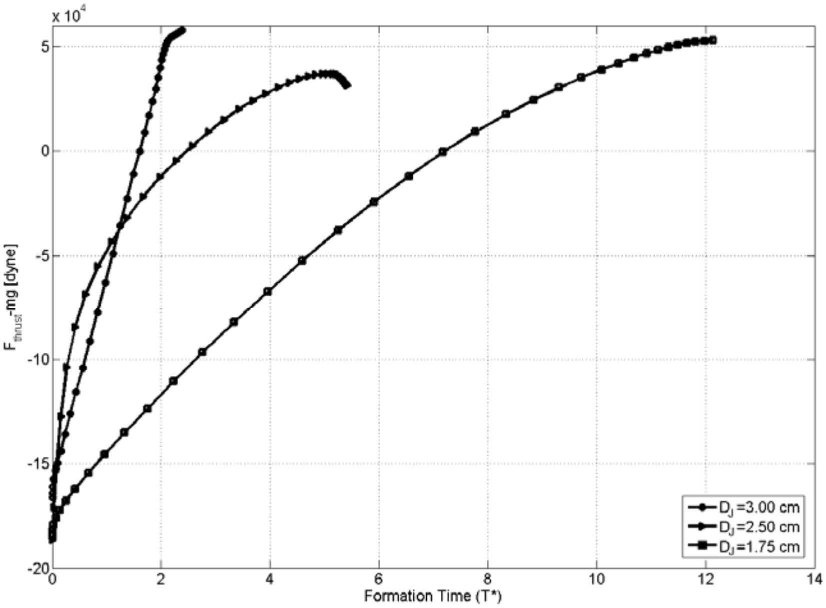

Figure 2.6. Time averaged thrust subtracted by the instantaneous weight of the water column in atrium. For D_J *=3.00 cm,* thrust reached its peak at *T*=2.00±0.1*, for D_J *=2.50 cm*, the maximal thrust was attained at *T*=5.0±0.4* and for D_J *=1.75 cm*, the forced had the peak at *T*=11.00±0.3* (Figure 6).

Likewise, the thrust magnitude was computed by measuring variations in trans-annulus pressure together with the instantaneous jet velocity (2-11). Considering that F_{recoil} and F_{thrust} have been computed by different experimental techniques, the slight discrepancies in the relative timings of the two quantities could be attributed to measurement errors.

2.4.4. Circulation

Circulation of the ejected vortex ring was computed based on vorticity/velocity fields (2-6 and 2-7) obtained from phase-averaged DPIV (Figure 2.7). Vortex ring pinches off when no additional energy or circulation would be added to the leading vortex ring[16]. By plotting the circulation versus formation time, the incident of pinch-off (formation number) can be defined as the formation time (T^*) at which the circulation curve saturates. Figure 2.8 compares the vortex ring circulation as function of formation time for each annulus diameter studied. It can be observed that the slope of circulation curve dramatically flattens at $T^*=2.00\pm0.2$ for $D_J=3.00\ cm$. For $D_J=2.50\ cm$, circulation curve started to saturate at $T^*=4.00\pm0.2$. However, for $D_J=1.75\ cm$, the circulation curve grew further than the former cases until $T^*=13.00\pm0.6$ at which the circulation curve began to flatten (Figure 2.8).

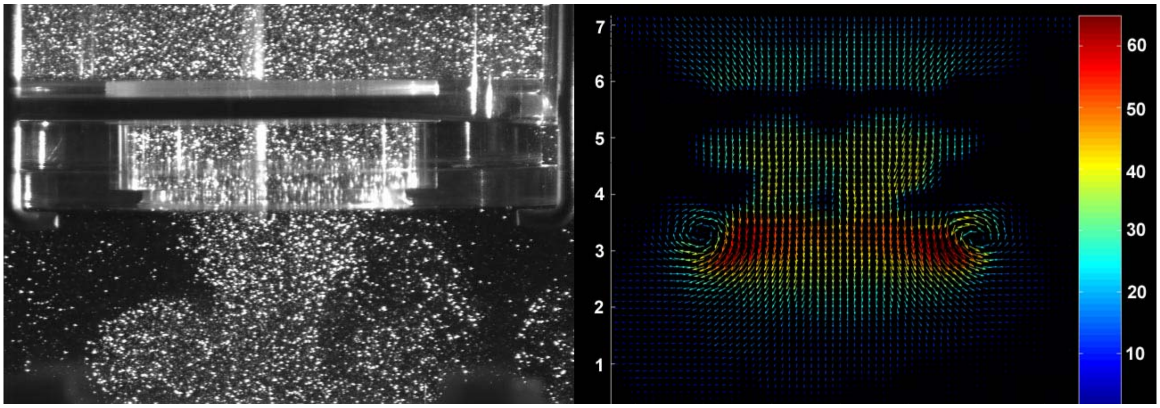

Figure 2.7. (Left). The particle field of the experiment with $D_J=3.00\ cm$ when a vortex ring is forming from trans-annulus flow. (Right) the velocity field of the same experiment. The circulation (Γ) of the leading vortex ring was computed from a sequence of velocity fields.

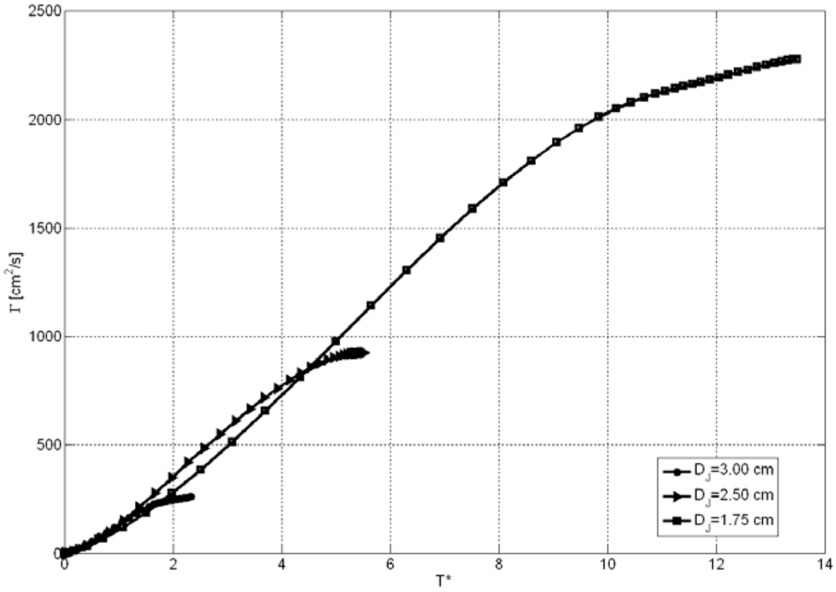

Figure 2.8. Circulation of the ejected vortex ring obtained from vorticity/ velocity fields versus formation time for each annulus diameter. The slope of circulation curve dramatically flattens at *T*=2.00±0.2* for D_J *=3.00 cm*. For D_J *=2.50 cm*, circulation curve starts to saturate at *T*= 4.00±0.2* and for D_J *=1.75 cm*, the circulation curve grew until *T*=13.00±0.6* at which the circulation curve began to flatten.

2.5. Discussion

The timing of trans-annulus pressure drop was found to be inversely correlated with the size of the annulus regardless of the similar pressure drop (τ=35±5) in ventricular chamber (Figure 2.4). Faster pressure drop for D_J *=3.00 cm* resulted in completion of trans-annulus flow [volume transfer] in a shorter formation time (Figure 2.3). For D_J *=2.50 cm and* D_J *=1.75 cm*, trans-annulus flow completed in *T*=5.40±0.5* and *T*=11.30±0.6*, respectively.

Although the volume of fluid transferred between the two chambers were identical, the magnitude and the instant of the recoil force was not the same for the annulus diameters studied (Figure 2.5). Therefore, the size of annulus is a significant parameter in dynamics of the annulus plane during propulsion. This study was planned in such a way that no other forces rather than the ones generated due to the trans-annulus flow can affect on the annulus plane. As a matter of fact, we computed the thrust generated during propulsion (Figure 2.6) and the circulation of the ejected vortex ring for each case (Figure 2.8) to correlate with the annulus plane recoil force.

The final magnitude of thrust generated by each annulus diameter was almost identical, while the time it took for each annulus size to reach the peak was different (Figure 2.6). This was the consequence of how momentum transferred from one chamber to another; the peak incident showed a direct relationship with the time period needed to complete the volume transfer (Figures 2.3 and 2.6). Considering the recoil force (Figure 2.5), it can be observed that it reached a peak (Figure 2.5) once the thrust force was close to its maximal magnitude (Figure 2.6), thus confirming the same occurrence of the recoil force and the thrust.

The other parameter that was found to be changing with different annulus sizes was the vortex ring circulation (Figure 2.8). It has been observed that decreasing the size of the annulus increases the final magnitude of the circulation (Figure 2.8). However, the formation time at which the magnitude of the circulation saturated was different for each annulus size. The larger the annulus diameter, the sooner the circulation saturates.

Considering the trend of vortex ring circulation and the incident of maximal recoil force (Figures 2.5 and 2.8), for $D_J=3.00\ cm$ and $D_J=2.50\ cm$, it can be observed that the peak recoil force occurred at the formation time ($T^*= 2.00\pm0.1$ and $T^*=3.8\pm0.2$, respectively) in which circulation was saturating ($T^*=2.00\pm0.2$ and $T^*=4.00\pm0.2$, respectively). In the case of $D_J=1.75\ cm$, the peak recoil force occurred at $T^*=11.30\pm0.3$, later than the formation time at which circulation saturated ($T^*=10.00\pm0.3$).

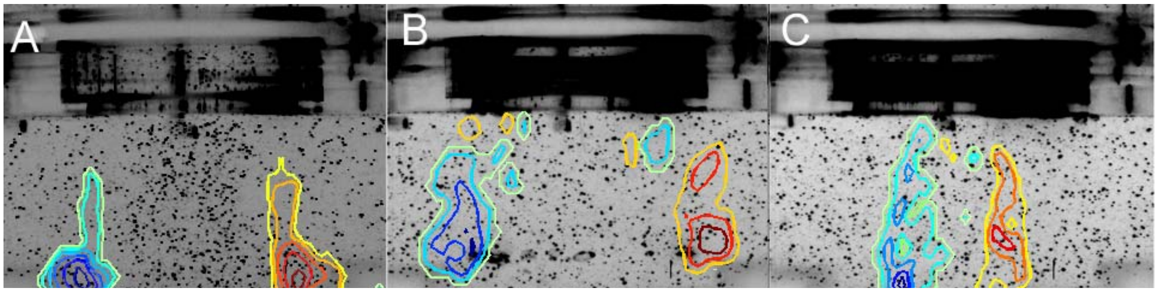

Figure 2.9. Snapshot of the vorticity field obtained by DPIV for different cases at the onset of peak recoil force. (A) D_J = 3.00 cm: in this case, the vorticity field shows that the leading vortex was not yet pinched off (*T*= 2.00±0.1*), whereas it was hitting the bottom wall. This prevented further growth of the leading vortex ring. (B) D_J =2.50 cm: in this case the leading vortex has just pinched off (*T*=3.8±0.2*) and (C) D_J = 1.75 cm: in this case, the recoil force had a peak at *T*=11.00±0.4*. The corresponding vorticity field shows that there was only trailing jet, meaning that the leading vortex ring has already been pinched off.

It has been shown previously that a vortex ring is considered pinched off when the circulation does not increase, which means that the leading vortex ring does not receive any additional energy from the starting jet[36]. In the present study, it was found that for D_J *=3.00 cm* and D_J *=2.50 cm*, both maximal recoil force and maximal jet thrust occurred at the formation time in which vortex ring circulation was saturated. Figure 2.9 shows a snapshot of the vorticity field obtained by phase-averaged DPIV for each case at the onset of peak recoil force. The maximal value of the recoil force was attained in the case with D_J *=2.50 cm* at *T*=3.8±0.2*. In this case, the formation time at which the recoil-force peak occurred was in the range of the formation number defined by Gharib, et al[3]. This implies that all the circulation produced in the pulsed jet went into the leading vortex ring, thereby maximizing the recoil force. This was also confirmed by the vorticity plot in Figure 2.9b, which shows that the leading vortex pinches off at this formation time.

The vorticity field in Figure 2.9A shows that at this formation time the leading vortex was not yet pinched off, whereas it was hitting the bottom wall. This prevented the further growth of the leading vortex ring, thereby limiting the corresponding recoil force and any further increase in magnitude of circulation (Figure 2.8). For the smallest annulus (D_J = *1.75 cm*), the recoil force had a peak at $T^*=11.30\pm0.3$ and the peak value was the smallest among all the three annulus sizes. By comparing Figure 2.5 and Figure 2.8, it can be inferred that at the incident of recoil force ($T^*=11.30\pm0.3$), the circulation curve has been flattened earlier, thus the vortex ring was already pinched off ($T^*=10.00\pm0.3$). This assumption was also confirmed by the corresponding vorticity field at the onset of peak recoil force plotted in Figure 2.9C. In this case, it was apparent that the vortex ring had already hit the bottom and the vorticity was no longer entrained from the shear layer region of the trailing jet. The recoil force in this case was the result of the trailing jet, rather than the consequence of vortex ring pinch-off; that might be a reason for its much smaller magnitude compared with the other two annulus sizes (Figure 2.5).

2.5.1. Equivalent piston-cylinder setup

Starting jets are typically created by using a piston-cylinder setup. To relate the results of the present study to the other known results for a standard piston-cylinder setup, an equivalent stroke ratio (SR) was defined for each annulus size as the ratio of the length of jet (L_J) to the jet diameter (D_J). These quantities were obtained based on conservation of mass and equating volumes of fluid exchanged between the two chambers:

$$V_{ejected} = \frac{\pi}{4} D_A^2 . L_A = \frac{\pi}{4} D_J^2 . L_J \quad (2\text{-}13),$$

where $V_{ejected}$ is the total volume of fluid ejected from the atrial tube in a single run, L_A is the water-level height change in atrial tube (L_A*=1.00 cm*; constant for all the cases), and L_J is the nominal jet length, or the distance traveled by a piston with diameter D_J, ejecting the same volume from an equivalent piston-cylinder setup. In other words, if the total ejected volume is kept constant, the equivalent SR can be attributed to an equivalent experiment performed with a piston-cylinder setup in which the total volume of ejected fluid is the same.

Based on equation (2-13), the equivalent stroke ratios were 9.14 for D_J*=1.75 cm*, 3.12 for D_J*=2.50 cm*, and 1.80 for D_J*=3.00 cm.* The equivalent piston-cylinder setup that generated the maximal recoil force (Figure 2.5) had an SR of 3.12, which among all cases, the closest to the ratio that Krueger and Gharib[17] found generated maximal averaged thrust. It was also found that the recoil force was maximized at a formation time close to the equivalent SR for each case (Figure 2.5). This was expected because of the fact that the total thrust for the three cases was conserved (Figure 2.6), due to the constant ejected volume (2-13). However, the magnitude of the peak recoil force was different in each case (Figure 2.5).

2.5.2. Physiological significance

It has been shown previously that the normal pattern of LV filling is altered due to the diastolic dysfunction, which occurs during development of heart failure (HF)[8,52,53]. This variation in trans-mitral flow would also be reflected in diastolic motion of the mitral annulus measured by Doppler tissue imaging (DTI)[54]. DTI of mitral annulus has been recognized as an effective indicator of LV function in human heart[55,56]. The peak velocity of the mitral annulus away from the apex during early diastole (E_M), which indicates the rate of longitudinal expansion of the LV, is reduced in patients with impaired diastolic relaxation[34].

In the present study, we showed that in a simplified model of the left heart, the variation in jet stroke ratio can be reflected in dynamics of mitral annulus plane. More specifically, we found that for a physiologic base-apex distance and an annulus diameter of *2.50 cm*, which closely approximates the normal annulus diameter in adults, if the physiologic pressure decay applied, the annulus plane recoil force would be maximal at the time in which the vortex ring pinched off. In a real heart, the complex geometry and the viscoelastic properties of the ventricular chamber, as well as the wall-flow interaction and viscosity are also responsible for variations in dynamics of mitral annulus. However, the above-mentioned parameters directly influence trans-mitral flow and the formed vortex ring.

Almost all of the patients with idiopathic dilated cardiomyopathy have a significantly larger mitral annulus[57]. Therefore, as a result, the trans-mitral jet stroke ratio would be different than a normal LV. In a recent study, Mori, et al[58] showed that the peak mitral annulus velocity also would be lower than normal in cases with dilated cardiomyopathy. The results of their study is congruent with our observation-- confirming that by increasing the annulus diameter to more than *2.50 cm,* even if a physiologic LV pressure drop is applied, the annulus recoil is not optimum when compared to normal.

On the other hand, another recent study by Ozer, et al[59] has demonstrated that the LV long-axis function [evaluated by DTI] in patients with pure mitral stenosis is significantly impaired, despite normal global systolic function. In this case, if the LV pressure drop during diastole remains constant, the trans-mitral jet stroke ratio will increase. This observation is also consistent with our study corroborating that by decreasing the mitral annulus diameter, despite the fact that the trans-mitral jet velocity increases, the annulus recoil force will be smaller than the normal case.

2.6. Conclusion

The present *in-vitro* study confirms the presence of a vortex ring during the rapid filling phase of diastole and implies that the process of vortex ring formation can influence mitral annulus dynamics. Additionally, this study suggests that vortex ring formation can be used as an index for assessment of LV function during diastole and as a factor that should be considered in design and implementing cardiac prosthetics devices.

2.7. Limitations

In this study we did not consider the active myocardial contractions, interaction of valve leaflet and flow, nor the blood viscosity on formation of the vortex ring. Works are in progress to design and use an actively contracting chamber for mimicking cardiac expansion, using bioprosthetic heart valves in mitral position and blood analogs for viscose flow. Another limitation of this study resulted from using a phase-averaged DPIV technique, which slightly increased the error factor due to the fast nature of the experiment. Work is in progress to use continuous laser for illumination and high-speed cameras for stereo-PIV to obtain more accurate results.

CHAPTER THREE

Influence of mitral valve kinematics and left ventricular pressure drop on annulus plane dynamics[§§]

3.1. Chapter Abstract

Several studies have suggested that the mitral annulus displacement and velocity in early diastole can be used as indicators of diastolic performance**.** The peak velocity of the mitral annulus away from the LV apex during early diastole, indicating the rate of longitudinal expansion of the LV, is reduced in patients with impaired diastolic relaxation. With the intention of relating the trans-mitral flow to mitral annulus plane dynamics, we measured annulus recoil force for different mitral valve sizes, while applying exponential pressure decay programs in the ventricular chamber. The vorticity plot was also obtained when the maximal recoil force was achieved. Comparing the vorticity contour plots with the recoil force measurements, it was inferred that the magnitude of recoil force is maximal whenever the vortex ring is about to pinch off, regardless of the size of the valve and the pressure gradient. Plotting the force magnitude versus formation time, it can be observed that the force is maximal in a range of formation times between 3 and 5, which is the optimum range or the range of vortex formation number.

[§§] Submitted to *Annals of Biomedical Engineering*

3.2. Introduction

Dynamics of mitral valve annulus during diastole is a topic that has received much attention recently given its important effects on valve performance in addition to its close association with diastolic heart failure (HF). Several studies have suggested that the mitral annulus displacement[60,61] and velocity in early diastole can be used as indicators of diastolic performance[34,62,63,64]. It has also been shown previously that during the development of HF, normal pattern of left ventricular (LV) filling would be altered due to the diastolic dysfunction[65,52,8,53]. This variation in trans-mitral flow would be reflected in diastolic motion of the mitral annulus measurable by Doppler tissue imaging (DTI)[54]. The peak velocity of the mitral annulus away from the LV apex during early diastole (E_M), indicating the rate of longitudinal expansion of the LV, is reduced in patients with impaired diastolic relaxation[34].

Mitral annulus anatomy and physiology has been extensively studied in both experimental animals and human subjects using roentgenogram marker imaging[66,67], sonomicrometry[68], MR Imaging[69] and echocardiography[70,71]. The current literature strongly supports the dynamic motion of the annulus during diastole. However, the influence of mitral valve kinematics in conjunction with trans-mitral flow on dynamics of the mitral annulus has not been discussed so far.

3.2.1. Vortex formation in left ventricle

The presence of vortex rings that develop during cardiac diastole was initially recognized by *in-vitro* visualization of the ventricular flow[10,11] and subsequently confirmed by analyses based on color Doppler mapping[12,72] and MR Imaging[13,14]. Vortex rings typically develop from a starting jet or slug of fluid ejected from a nozzle. In fluid mechanics, trans-mitral flow is considered a rapidly starting jet. The process of the formation of a vortex ring in fluid mechanics literature is described by a dimensionless number called "formation time"[16]:

$$f = \frac{\overline{U}}{D} T \qquad (3\text{-}1)$$

where $\overline{U}$ is the mean velocity of the jet, T is the pulse duration and D is the diameter of the nozzle. The importance of this number lies in the fact that by increasing it beyond a certain range (~3.5-4.5) for a starting jet, no additional energy or circulation enters the leading vortex ring, and the remaining fluid in the pulse ejects as a trailing jet[16]. In a recent article, Gharib, et al[30] showed that the distribution of formation time in randomly-selected volunteers converges to a unique range of values between 3.5 and 5.0. They also showed that the vortex formation time in patients diagnosed with dilated cardiomyopathy (DCM) is lower than that range.

The critical role of vortex ring formation rests on the relative contribution of the leading vortex ring and the trailing jet (which appears after pinch-off) to the thrust supplied to the flow[17]. In a recent paper[73], we measured the average recoil force exerted on an annulus plane during rapid filling phase as function of formation time (3-1), and showed that it would be maximal when the formation time reaches around the value of 4. This condition was achieved only by implementing physiologic values for the annulus diameter (without leaflets) and LV pressure drop to experimentally model the rapid filling phase. However, kinematics of the heart valve's leaflets as they open and close during diastole seem to interact with the process of vortex ring formation, thus complicating the response of the mitral annulus to the pressure drop. In the present study, we correlate early diastolic flow with the annulus plane recoil force and the trans-mitral pressure drop through the index of vortex formation time that is computed from the early diastolic flow profile, and mitral valve kinematics.

3.3. Methods

The experimental setup was built to imitate the trans-mitral flow during early diastole in response to rapid pressure drop in the left ventricle. As a result of the pressure drop, the mitral valve opens immediately, allowing the flow from atrium to ventricle, the ventricle expands and the valve plane moves in the opposite direction with respect to the flow. To be consistent with cardiac physiology, the LV pressure drop in early diastole was forced to decay as an exponential function with a pressure-drop time-constant (τ)[21] in physiological range (2-2).

3.3.1. Experimental setup components

The experimental setup was comprised of two chambers partially filled with water; the nominal ventricle was built as a Plexiglas chamber connected to a suction pump (VSI SPS3891, *Vivitro Systems Inc.*) to generate pressure drop, and the nominal atrium was a cylindrical tube sitting inside the ventricular chamber as shown in Figure 3.1. Dimensions of the ventricular box were 13cm (width) by 13cm (depth) by 20cm (height), although, only the lower 13cm of the box was filled with fluid (Figure 3.1). The base-apex distance was set to 9cm which is the same as the base-apex distance in LV as mentioned in medical literature[43,44]. The mitral annulus plane was replicated as a flat plate with a circular orifice for insertion of a mitral bioprosthetics. Additionally, to prevent the effect of mass transfer on annulus-plane dynamics, a low flow resistant pneumatic check-valve (R-702, *Resenex Corp.* Chatsworth, CA) was placed on ventricular chamber. The mass of fluid entering from the atrial tube pushed the trapped air in the ventricular chamber to leave the box through the check-valve avoiding mass transfer effect.

To reproduce the movement of the valve plane during early diastole, the valve plane was allowed to slide in the downstream end of the atrial tube without friction (Figure 3.1). Three L-shaped rods prevented the plate from falling in the ventricular chamber (Figure 3.1). The LV pressure drop was reproduced by a computer-controlled suction pump (Superpump system VSI SPS3891). The considered ranges for pressure-drop time-constant was within the physiologic range[25,45] and the volume of ejected fluid at each cycle was set to 50ml, which is equivalent to the volume of blood transferred into the human LV during early diastole[46].

Both chambers and the sliding annulus plane were made of Plexiglas to facilitate flow visualization and the measurement of annulus plane displacements using high-speed cameras. More details about the experimental apparatus are described in our recent publication[73].

Carpentier-Edwards' PERIMOUNT bioprosthetic heart valves (Edwards Lifesciences, *Irvine, California*) in different sizes (21, 23, 25 and 27mm) were used to mimic the mitral valve function. For each experiment, the appropriate bioprosthetic valve was securely placed within the annulus plane (Figure 3.1).

Figure 3.1. Schematics of the experimental setup.

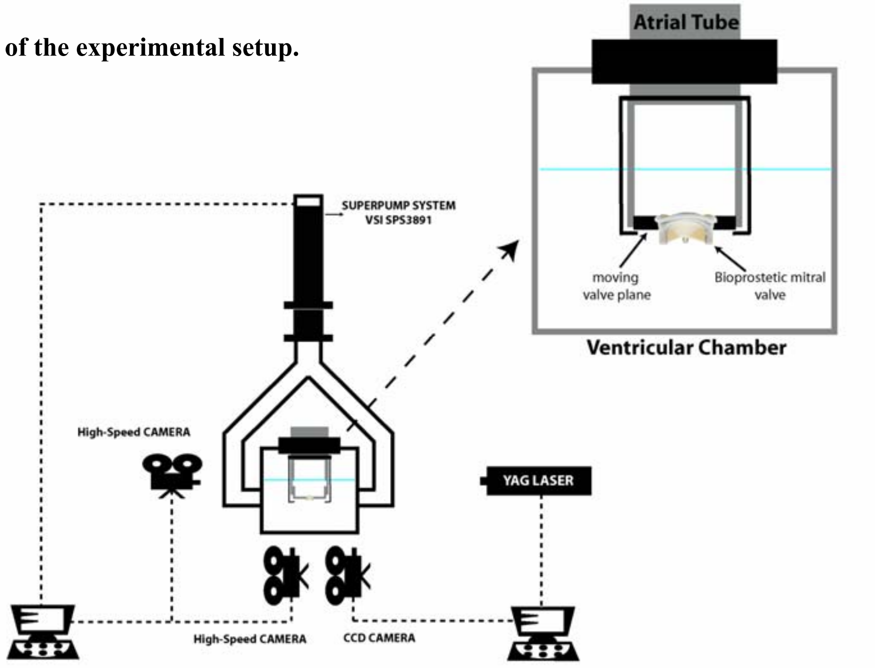

3.3.2. Reproduction of early diastole

For each run, both atrial and ventricular chambers were set to start from atmospheric pressure approximately equal to the physiological pressure in the left atrium prior to rapid filling. To reproduce the sudden pressure drop, the suction pump created a rapid trans-mitral pressure difference. We used four different sizes of mitral valve to simulate different flow conditions. For all considered cases, the pump was set to displace a constant volume of fluid (50ml) while the pressure drop scheme and the initial water height in the system were kept the same. The pressure inside the ventricular chamber was measured with a pressure monitoring system during the experiment (Deltran DPT-400 pressure transducers and VSI-TP8891 *Vivitro Systems, Inc.*).

For accuracy of measurement and to make sure that the obtained results were reproducible and consistent with each other, every set of experiment consisted of 20 consecutive cycles. For each single cycle, the LV pressure was forced to decay as an exponential function in response to the applied suction:

$$P = P_0 \exp(\frac{-t}{\tau}) \qquad (3\text{-}2)$$

where t was time, P_0 was the initial pressure set to atmospheric value, τ were the pressure drop time-constants and adjusted to 35±5 and 20±5 milliseconds.

3.3.3. Measurement methods

The displacement of water level inside the atrial tube, displacement of annulus plane and the opening area of the valve were measured using two synchronized high-speed cameras (Photron FASTCAM-Ultima, *PHOTRON USA, Inc***.** San Diego, CA) at 250fps. The water level velocity was computed by finite difference based on measured water level data. Applying continuity and considering a uniform profile for exit jet velocity over the valve cross-section, trans-mitral flow rate computed as:

$$\frac{dV}{dt} = A(U_A(t) - U_V(t)) = S(U_J(t) - U_V(t)) \quad (3\text{-}3)$$

where dV is the volume element of fluid going through the orifice, $U_J(t)$ is the instantaneous exit jet velocity, $U_A(t)$ is the water-level velocity at the atrium, $U_V(t)$ is the valve plane velocity, S is the open cross-section of the valve and A is the cross sectional area of atrial part, which is constant (Table 1). Instantaneous exit jet velocity (U_J) was computed from (3-3) as:

$$U_J = \frac{A}{S}U_A + (1 - \frac{A}{S})U_V \qquad (3\text{-}4)$$

Displacement of the annulus plane was monitored by a third high-speed camera (Photron FASTCAM-Ultima) at 250fps, synchronized with the other two described earlier. Mass of the fluid inside the atrial tube at each instantaneous of time was computed as:

$$\rho\int dV_A = \rho(V_0 - \frac{\pi}{4}D_A^2(x_0 - \int_{x_0}^{x} dx)) \quad (3\text{-}5)$$

where ρ is water density, dV_A is the fluid volume element at each instant of time, V_0 is the initial volume of the fluid in the atrium, x_0 is the initial position of atrial water level with respect to the origin before starting the experiment, x is the instant position of water-level and dx is atrial water-level position element at each instant of time with respect to the origin. Vortex formation time (T^*)[16] for temporally variable nozzle diameter is modified as[19]:

$$T^* = \int_0^t \frac{U_J(\zeta)}{D_S(\zeta)} d\zeta \qquad (3\text{-}6)$$

where U_J and D_S are instantaneous exit jet velocity and the effective valve diameter, respectively and t is the time.

3.3.4. Digital Particle image velocimetry (DPIV)

The flow characteristic information (e.g. velocity field and circulation) was captured by phase-averaged DPIV (Digital Particle Image Velocimetry)[50]. DPIV uses two digital images of a particle-seeded flow illuminated by a thin laser sheet to determine the displacement field of the particles in the field of view (sampling window) by cross-correlating pixels in a subsection of two images. Flow was seeded with neutrally buoyant, orange fluorescent particles with the diameter in the range of 60-80 μm. A high-resolution monochrome CCD digital camera (30fps, 768x480; TM-9701, PULNiX America, Inc.) was positioned perpendicular to the ventricular chamber to capture the image sequences of the particle field (Figure 3-1). The pair of images were captured from illuminated sheet of fluorescent particles generated by a 25mJ double pulsed Nd:YAG laser with the pulse separation of 1ms.

The length of each pressure-drop cycle was set to 100ms, as mentioned earlier. The CCD camera used for DPIV took two pairs of images in each cycle. There were 20 consecutive cycles which were identical because of the same pressure drop (τ=35±5 or τ=20±5) applied. DPIV data were phase-averaged over the 20 identical cycles. Therefore, a total of 40 velocity/vorticity fields were captured for different time-points of the rapid-filling phase. This temporal resolution gave us an accurate estimate of the velocity and the vorticity fields to compute circulation of the vortex ring and to validate the exit jet velocity (U_J) obtained from a different method (3-4). The CCD camera was triggered simultaneously with the first cycle of experiment and was synchronized with the *PHOTRON* high-speed cameras. The laser sheet was set perpendicular to the jet and cut through the center of annulus. This configuration allowed analysis of velocity and vorticity fields resulting from the starting jet at the illuminated cross-section.

3.3.5. Control volume analysis

The momentum equation related to the setup was derived by considering the control volume (Ω) equations for the fluid inside the atrial tube (Figure 3.2). Flow was considered inertia dominant because of high Reynolds number at the annulus and shear stress contribution to the momentum equation was neglected. Assuming constant gravitational field (**g**) acting on the control volume (Ω) with moving boundary, the momentum equation would be described as:

$$\frac{\partial}{\partial t}(m\mathbf{U_V}) + \rho\int_{\partial\Omega}\mathbf{U_J}((\mathbf{U_J}-\mathbf{U_V}).\mathbf{n})ds = m\mathbf{g} + \int_{\partial\Omega}(P_\infty - P)\mathbf{n}ds \qquad (3\text{-}7)$$

where $\mathbf{U_J}$ is the instantaneous exit jet velocity vector, $\mathbf{U_V}$ is the annulus plane velocity vector and *m* is the mass of the annulus plane together with the instantaneous mass of the fluid:

$$m(t) = M_{Annulus} + \rho\int_{\Omega}dV_A(t) \qquad (3\text{-}8)$$

P is the pressure at the annulus and P_∞ is the pressure at the atrial side of the valve (Table 3.1). Based on the momentum equation (3-7), recoil force is described as

$$\mathbf{F_{recoil}} = \frac{\partial}{\partial t}(m\mathbf{U_V}) = (M_{Annulus} + \rho\int_{\Omega}dV_A)\mathbf{a_V} + (\rho\frac{\partial}{\partial t}\int_{\Omega}dV_A)\mathbf{U_V} \quad (3\text{-}9)$$

where $\mathbf{a_V}$ is the valve plane acceleration vector.

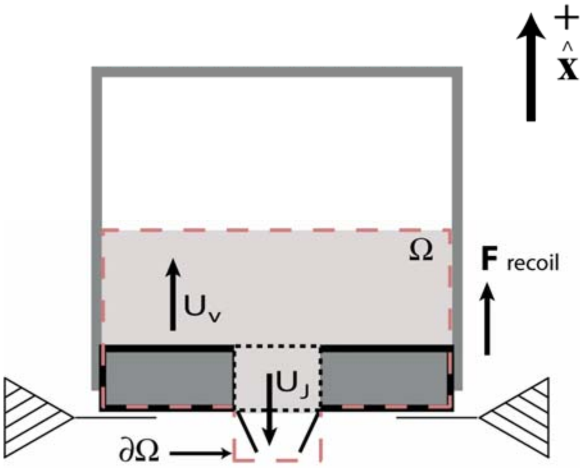

Figure 3.2. Embedded control volume (Ω) of fluid inside the atrial tube. Red broken line shows the embedded control volume. $\mathbf{U_J}$ is the instantaneous trans-mitral jet velocity. $\mathbf{U_V}$ is the valve plane velocity. The positive direction is shown on the Figure. The direction of the recoil force is shown.

3.4. Results

3.4.1. Correlation between the valve size and the annulus plane dynamics

Valve plane acceleration was measured for all the tested valves and the recoil force was computed based on that (3-9). Figure 3.3A depicts averaged annulus plane recoil force for different sizes of valves in resting physiological condition (τ=35±5ms) and Figure 3.3B shows the same function in a faster pressure drop condition (τ=20±5 ms). For comparison purposes, all results were shown as a function of formation time. Maximum jet velocities measured for different sizes of valves are shown in Table 3.2.

Table 3.1. Abbreviations and acronyms

P	Pressure at nozzle
P_0	Initial pressure at ventricle
τ	Pressure drop time-constant
V	Volume of fluid passes the orifice
U_J	Instantaneous exit jet velocity
U_A	Water-level velocity at the atrium
U_V	Valve (annulus) plane velocity
D_J	Orifice diameter
D_A	Atrial tube diameter
ρ	Water density
V_A	Instantaneous volume of fluid in atrium
V_0	Initial volume of fluid in atrium
x_0	Initial position of water level in atrium
x	Instantaneous position of water-level
T^*	Formation time
t	Time
m	mass of the annulus plane plus mass of atrial fluid
g	Gravitational acceleration
a_V	Valve (annulus) plane acceleration
$M_{Annulus}$	Mass of the annulus plane
P_∞	Pressure at atrial side of the nozzle

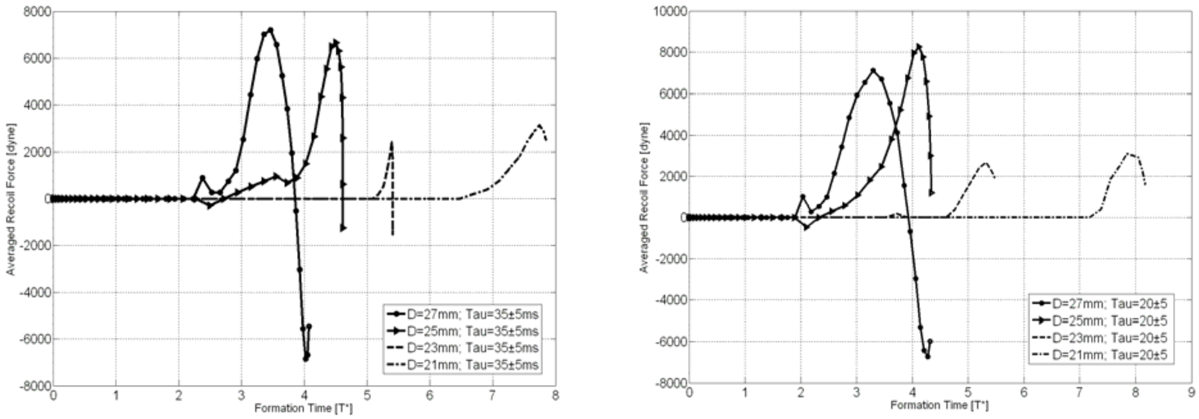

Figure 3.3**. Averaged annulus recoil force. (A)** Left: shows annulus recoil force as function of formation time for different valve sizes due to a pressure drop with the time constant of τ=35±5 ms. **(B)** Right: annulus recoil force as function of formation time for different valve sizes due to a pressure drop with the time constant of τ=20±5 ms.

3.4.2. Correlation between the pressure drop and the annulus plane dynamics

To relate different pressure-drop programs with the annulus recoil force, two distinct pressure programs were applied to the system. The pressure decay scheme followed the same exponential format as stated in (3-2), with different time-constants (τ=30±5 ms andτ=20±5 ms). Formation time and the mitral annulus recoil force were computed as stated in (3-3) to (3-9). Comparative plots of averaged recoil force as function of formation time for all the valve sizes are depicted in Figure 3.4.

For the valve size 21mm, variation in pressure drop time-constant did not result in a significant change in the magnitude or at the onset of the maximal recoil peak (Figure 3.4A). Variation of pressure drop time-constant using a 23mm mitral valve resulted in a change in magnitude of recoil force (Table 3.1), but no significant change at the peak incident (Figure 3.4B). Both magnitude and incident of peak recoil force changed considerably in response to different pressure drop programs when a 25mm valve were used in mitral position (Figure 3.4C). For the valve size 27 mm, variation in pressure drop time-constant resulted in a change at the incident of the recoil peak; however, the magnitude of the peak did not change (Figure 3.4D).

Mitral valve size	Maximum effective opening diameter (cm)	Maximum exit jet velocity (cm/s)	Maximum recoil force (dyne)		T* for maximum recoil force	
			τ=20±5 ms	τ=35±5 ms	τ=20±5 ms	τ=35±5 ms
27mm	2.79	93.27	7107	7191	3.30	3.50
25mm	2.27	120.56	8262	6660	4.10	4.50
23mm	2.11	125.00	2683	2434	5.30	5.40
21mm	1.98	129.40	3090	3134	7.80	7.70

Table 3.2. Physical dimensions of the Bioprosthetic mitral valves used for the experiments. Magnitude of maximal exit jet velocity, maximal recoil force and the formation time at which maximal recoil force occurred has been shown.

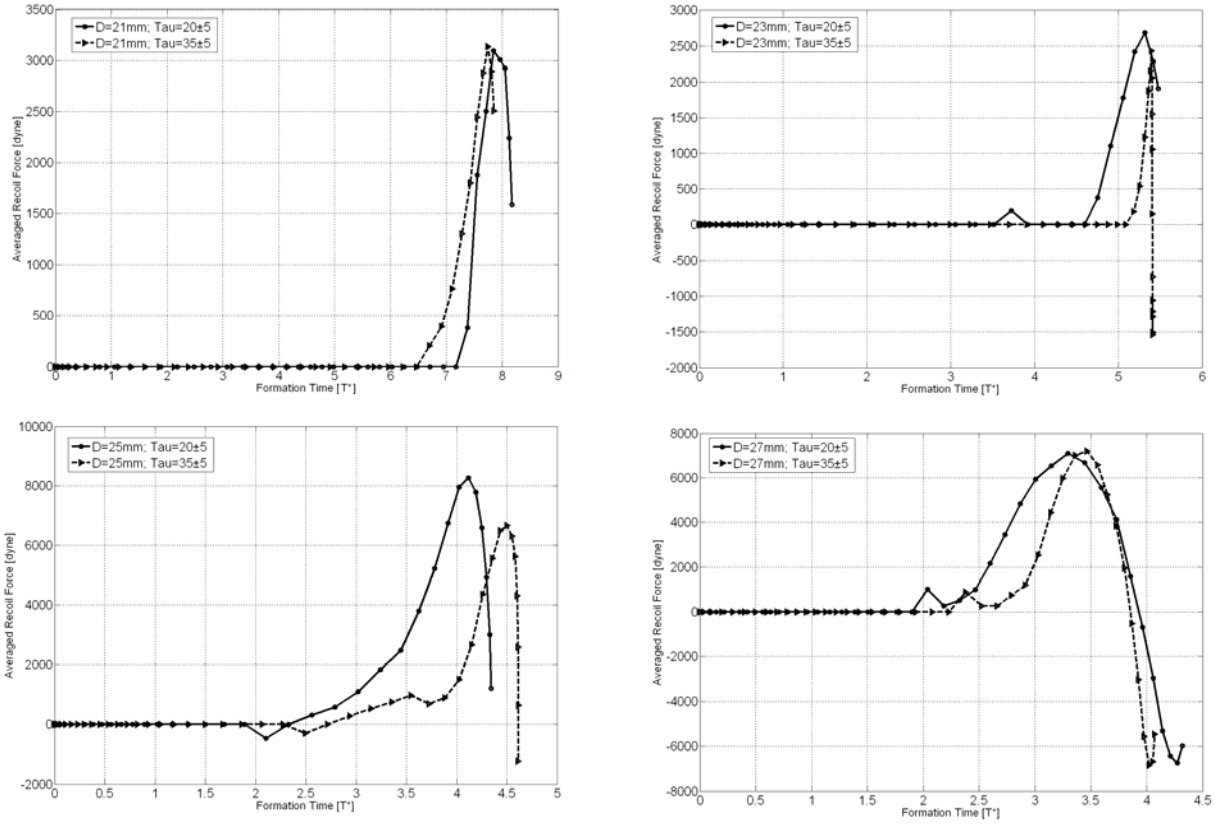

Figure 3.4. Comparison of annulus plane recoil force for different pressure drop programs (τ=35±5 ms versus τ=20±5 ms). (A) mitral valve size 21; **(B)** mitral valve size 23; **(C)** mitral valve size 25 and **(D)** mitral valve size 27.

3.4.3. Correlation between vortex formation and the annulus plane dynamics

The vorticity field was computed from DPIV measurements during trans-mitral flow for each experiment. Figures 3.5 and 3.6 depict the vorticity fields captured simultaneously with the maximal recoil force using different pressure-decay programs.

Figure 3.5 shows the vorticity field captured at the maximal recoil force after the pressure decay with the time constant of τ=35±5 ms. Figures 5A and 5B depict the vorticity field for valve sizes 21mm and 23mm, respectively, superimposed over the particle-seeded flow field when the recoil force reached its maximal value. The vorticity fields shown in both subfigures demonstrate the leading vortex ring has pinched off from the generating jet and a significant trailing jet appears. Figure 3.5C shows the vorticity contour plot just after completion of the pinch-off process from a 25mm valve. Figure 3.5D shows an isolated vortex ring ejected from a 27mm valve, which is not yet pinched off from its generating jet.

Vorticity contour plots obtained at the peak recoil force after applying a faster pressure drop (τ=20±5 ms) are shown in Figure 3.6. The pinched off leading vortex ring and a considerable trailing jet is captured for the valve sizes 21mm and 23mm (Figures 3.6A and 3.6B, respectively). Figure 3.6C shows a just pinched-off vortex ring, which appears to be in an earlier stage than in Figure 3.5c (valve size D=25mm). Figure 3.6D shows a growing vortex ring ejected from a 27mm valve.

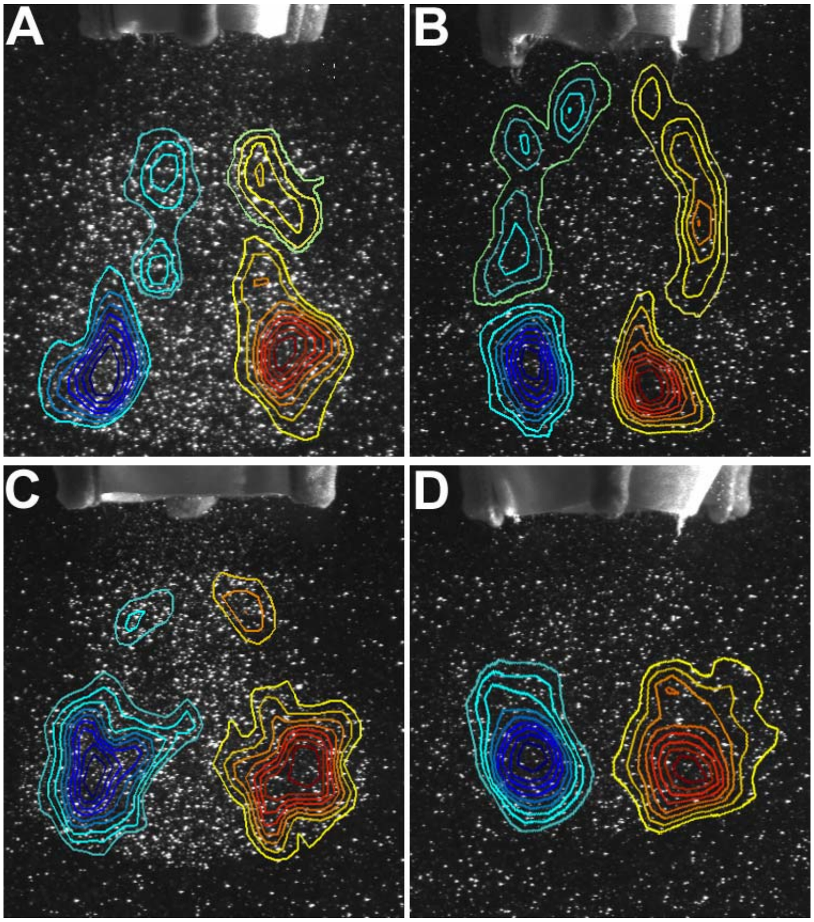

Figure 3.5. Vorticity contour plots computed from DPIV measurements during trans-mitral flow for each valve size when pressure decay time constant is assigned to τ=35±5 ms. (A) D=21 mm; (B) D=23mm. (C) D=25 mm and (D) D=27mm.

3.5. Discussion

In an intact heart, motion of the mitral annulus during the rapid filling phase represents the recoil force applied to the base of the heart. This motion is the consequence of interrelated changes in several parameters including LV volume status[74], left atrial pressure[75], atrioventricular flow[76] and the rate of myocardial relaxation[61]. All these factors can affect the LV flow structure. In the present study, we recapitulated the involved factors within the index of vortex formation time to quantify the mitral annulus recoil force based on that. We also substitute the myocardial relaxation effect with the LV pressure drop; bioprosthetic valves were used in mitral position and the left atrial pressure and the ejected volume were chosen similar to physiologic state.

Figure 3.6. Vorticity contour plots computed from DPIV measurements during trans-mitral flow for each valve size when pressure decay time constant is assigned to τ=20±5 ms. (A) D=21 mm; (B) D=23mm. (C) D=25 mm and (D) D=27mm.

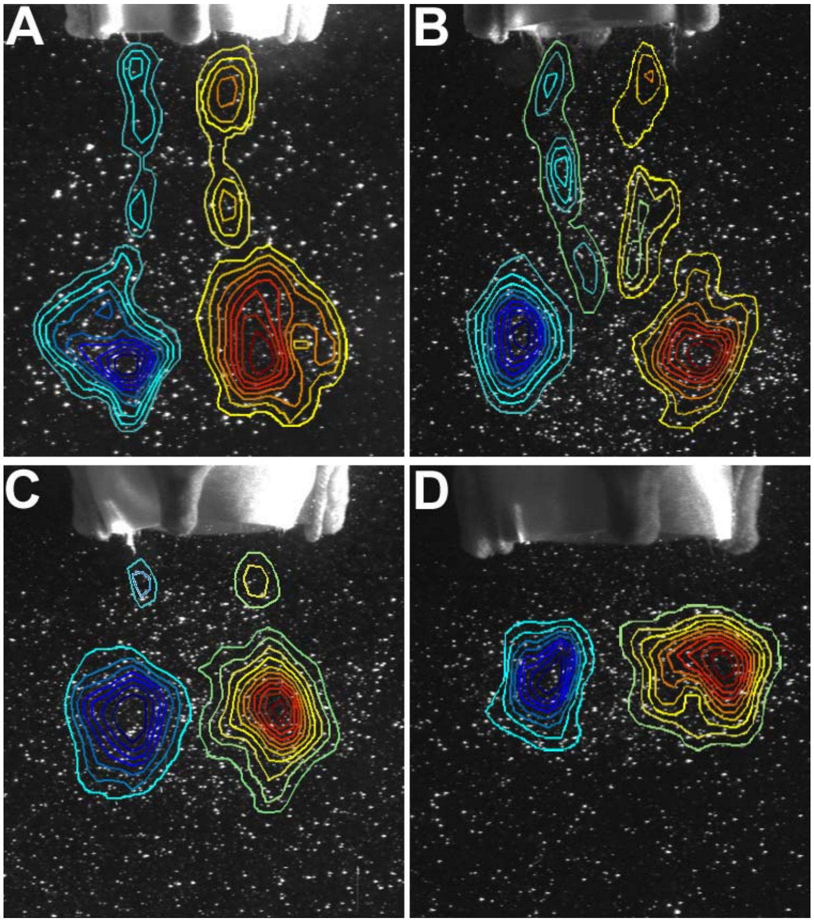

By looking at the status of the formed vortices generated by a pressure drop with a time constant of 20±5ms (Figure 3.5) at the time in which the maximum recoil force was attained (Figure 3.3A), it can be observed that for valve sizes 21mm and 23mm, the vortex ring has already pinched off earlier than the force peak and the maximum momentum has been transferred through the remaining trailing jets. However, in the larger diameter cases of mitral valves, the vorticity field (Figure 3.5) shows that the vortex ring is still forming (D=27mm) or the ring has just pinched off (D=25mm) when the maximum recoil force is achieved. Comparing the magnitude of recoil force in each case and considering the same transferred volume, it can be suggested that a maximal recoil force is generated over the mitral valve at the onset of vortex pinch off.

By increasing the rate of pressure drop (τ=20±5), the maximal recoil force occurred at an earlier formation time for larger valve diameters (25mm and 27mm) and the magnitude of the force has also changed (Figure 3.3B). By looking at the vorticity contour plots (Figures 3.6C and 3.6D) and comparing them with the previous case (*τ*=30±5), it can be inferred that the magnitude of the recoil force is maximal whenever the vortex ring is about to pinch off, regardless of the size of the valve and the pressure gradient. Plotting the force magnitude versus formation time (Figure 3.7), it can be observed that the force is maximal in a range of formation times between 3.00 and 5.00, which is the optimum formation time[17] or the vortex formation number[16].

For the smaller diameters (21mm and 23mm), the magnitude of the force did not show a significant difference by increasing the rate of the pressure drop (Figure 3.4A and 3.4B). The explanation for this phenomenon lies within the fact that momentum is mostly transferred by the trailing jets, rather than the vortex ring. Therefore, since the maximum size of the vortex ring is relatively small and its contribution to momentum transfer is less than the trailing jet, the onset of vortex ring pinch off does not change the magnitude of generated force.

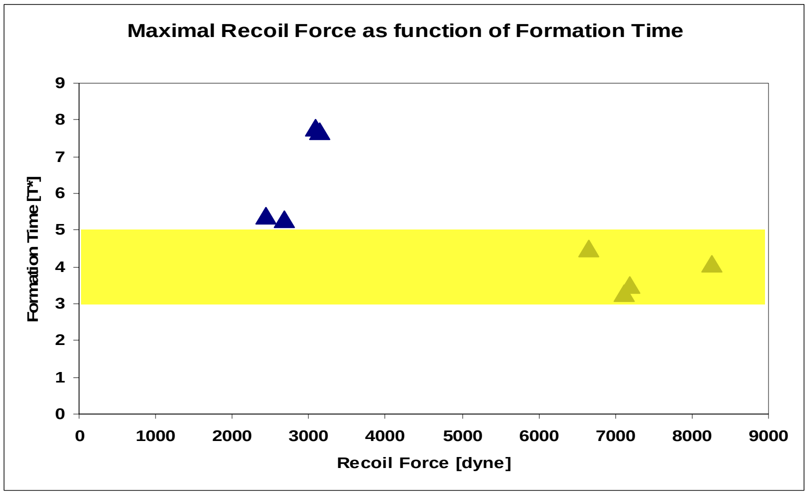

Figure 3.7. Maximal recoil force magnitude versus formation time. The yellow band shows the range of formation time that the maximal magnitude of recoil force has occurred at.

In summary, we suggest that the vortex formation process is the direct result of how the trans-mitral pressure difference is produced. Here, we do not seek the cause of disturbances in pressure gradient, which might have numerous explanations related to LV geometry, impaired relaxation, etc. However, we try to show that the vortex formation process can be used as an index for disturbances in trans-mitral flow.

3.6. Limitations

In this study we did not consider the active myocardial contractions. Works are in progress to design and use an actively contracting chamber for mimicking cardiac expansion.

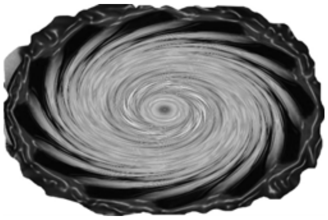

CHAPTER FOUR

Impact of Ventricular Pressure Drop on Early Diastolic Mitral Recoil through Vortex Formation Time

4.1. Chapter Abstract

The assessment of the mitral annulus motion with tissue Doppler imaging is claimed to be an accurate method to quantify global left ventricular systolic and diastolic function. In the present study, we used a mechanical model of the heart to generate different flow conditions based on systolic ratio. The model of left ventricle consisted of a transparent silicone sac with similar geometric characteristics for the mammalian heart. Two bioprosthetic heart valves were positioned at the mitral and aortic locations of the sac. The mitral valve recoil and the trans-mitral thrust were measured during early diastole and were correlated with the vortex formation time computed from trans-mitral flow and the temporal variation in mitral valve diameter. Results show that time-averaged thrust is maximized when formation time is in the range of 4 and 5 regardless of the shape of the waveform or the value of the pressure drop time-constant. In conclusion, we found that

the non-dimensional number representing the duration of early diastole is an important parameter with significant impacts on the quality of ventricular filling. The maximal mitral recoil and trans-mitral thrust were observed in conditions under which the left heart generates optimal propulsion.

4.2. Introduction

In cardiac physiology, left ventricular (LV) diastolic function, particularly early trans-mitral flow is an outcome of ventricular relaxation, compliance, and filling pressures. However, a number of additional physiological factors can influence diastolic function. Among them, diastolic suction or initial LV pressure drop -- as a result of ventricular relaxation during isovolumic relaxation -- were shown to actively contribute to early ventricular filling[22]. This rapid pressure drop is a phenomenon by which the LV can receive adequate filling volume at low pressure[77]. Thus, diastolic suction is one of the major parameters that affect the dynamics of LV filling.

The mitral annulus moves upward into the left atrium during diastole and downward toward the LV apex during systole[70]. The annulus movement exhibits rapid recoil back toward the left atrium during early diastole, which increases the net velocity of mitral inflow as much as twenty percent[78]. Recent studies[7,79,80] suggest that the diastolic motion of the mitral annulus, a representative of mitral annulus recoil force can be used to provide additional information on diastolic function.

In the present *in-vitro* study, the correlation between trans-mitral thrust, as a force that generates annulus recoil, and ventricular suction/filling has been studied through the index of vortex formation number. Ventricular pressure-drop and trans-mitral jet velocity were used as indicators for ventricular suction and ventricular filling, respectively.

4.3. Methods

In Chapters 2 and 3 we discussed the mitral annulus recoil force computed from the movement of the annulus plane. In the present study the recoil force was directly measured with a custom made load-cell[***] (*A.L. Design, Inc.,* Buffalo, NY) in an environment replicated as the mitral annulus inside a ventricular sac.

4.3.1. Experimental setup components

This study has been accomplished using Caltech's left heart pulsed flow simulator[51] modified specifically for this experiment. The schematic layout of the experimental system is shown is Figure 4.1. The system is comprised of a ventricle, shaped according to molds in the systolic state, and made of transparent silicone rubber (Figure 4.2). The ventricle was suspended around the Plexiglas atrium (Figure 4.3) at the upper part of a rigid, water filled, cubic container. The container is made of Plexiglas to avoid optical distortion.

The container is connected to a hydraulic pump system (Superpump system, VSI, SPS3891, *Vivitro systems Inc*., Victoria, BC, Canada). The Superpump system consists of a piston-in-cylinder pump head driven by a low inertia electric motor. The pump is controlled by a MATLAB® code compatible with a National Instrument Data Acquisition (DAQ) device. The code controls the pump's piston to move according to predefined functions. The oscillatory flow generated as a response to the appropriate waveform provides position and velocity feedback to the power amplifier (VSI, SPA3891Z). The water waveforms induce appropriate suction in the silicone ventricle during diastole.

[***] Dimensions and the engineering drawing of the load cell are provided in appendix (A.3.3.)

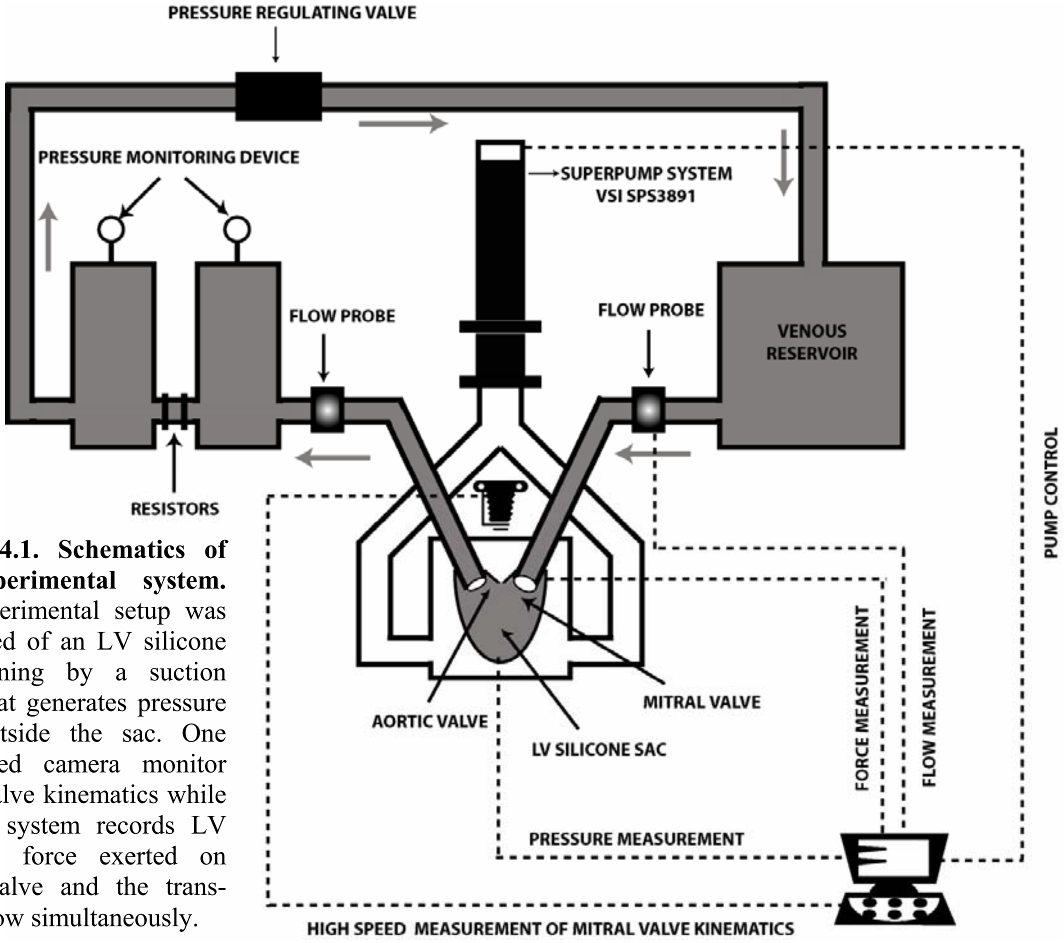

Figure 4.1. Schematics of the experimental system. The experimental setup was comprised of an LV silicone sac running by a suction pump that generates pressure drop outside the sac. One high-speed camera monitor mitral valve kinematics while a DAQ system records LV pressure, force exerted on mitral valve and the trans-mitral flow simultaneously.

One 27mm and one 23mm Carpentier-Edwards' PERIMOUNT heart valves (Edwards Lifesciences, *Irvine California*) were used in mitral and aortic positions, respectively. The mitral valve was mounted over the sensitive side of the load-cell (*A.L. Design, Inc.* Buffalo, NY) at the distal part of the atrial housing at the entrance of the LV sac (Figure 4.2). The aortic valve was positioned at the outlet of the LV sac (Figure 4.2). The mitral valve plane was designed in such a way that mimics the physiologic properties of a natural mitral valve and the passive mechanical properties of the papillary muscles were taken into account[81,82,83]. The load cell had a capacity of 14.00kg with the accuracy of 0.05% in vertical (trans-mitral flow) direction.

4.3.2. Reproduction of cardiac cycle

We used three different waveforms to imitate different physiological conditions for the left ventricle (Figure 4.3). The waveforms reproduced systolic ratios of 35%, 40% and 50% (Figure 4.3). Systolic ratio (SR) is the fraction of time in a cardiac cycle that the LV is in systolic phase. The frequency of cycles was set to different values for each systolic ratio group ranging from 0.5Hz to 1.67Hz (0.5Hz= 30 bpm; 1.0Hz=60 bpm; 1.2Hz=72bpm; and 1.67Hz =100bpm) reproducing operational range of cardiac function. Each experiment was running for 10 seconds. Since the motivation of this study was the dynamics of LV during early diastole (E-wave), atrial contraction phase (A-wave) was not generated by any types of waveform; except the 35% SR that generated a form of trans-mitral flow with an E-wave (35% of the cycle) followed by an A-wave (30% of the cycle).

In order to generate the physiological conditions, the aortic afterload was set to fluctuate in the range of 80-120 mmHg (mean 100 mmHg) during each cardiac cycle. The pressure at the aortic loop was measured by a pressure transducer (Deltran DPT-400). The pressure information was used as an input to a feed back control system that adjusts the stroke ratio of the hydraulic pump system.

4.3.3. Measurement methods

4.3.3.1. Trans-mitral flow/velocity measurement

Trans-mitral flow/velocity was measured by a flow measurement system (Transonic volume flow-meter, T-208, *Transonic Systems Inc.*) in real time. The flow rate information were acquired by Ni-DAQ card (CA-1000, *National Instrument*

Corporation) for further analysis along with the ventricular pressure, mitral recoil force and the effective open valve area. Trans-mitral jet velocity was computed from the flow rate and the effective open area of the mitral valve:

$$U_J = \frac{dQ}{dS} \qquad (4\text{-}1)$$

where Q is the trans-mitral flow rate and S is the open area of the mitral valve.

Figure 4.2. Close-up view of the ventricular sac and its components. A 27mm bioprosthetic mitral valve was securely positioned on a load cell that measuring the total force exerted on the valve plane. A Swan-Ganz catheter was used to measure the LV pressure during cardiac cycles. A 23mm bioprosthetic valve was used at the aortic position.

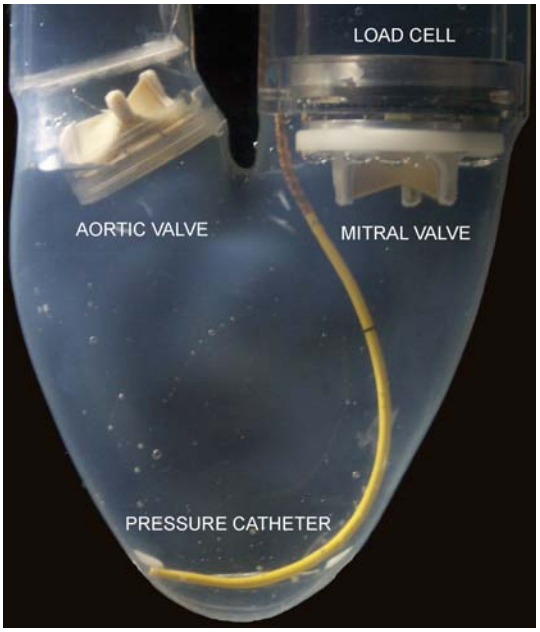

4.3.3.2. Ventricular pressure measurement

While the experiment was running, a clinical quality pressure transducer (Deltran DPT-400) monitored the real-time pressure changes inside the ventricular sac distal to the mitral valve through a Swan-Ganz catheter (Figure 4.2). The transducer was compatible with the pressure measurement system (VSI, TP8891) which amplified the signals and passed them to the DAQ card for further analysis on the computer. The schematic layout of the experimental system is shown in Figure 4.1.

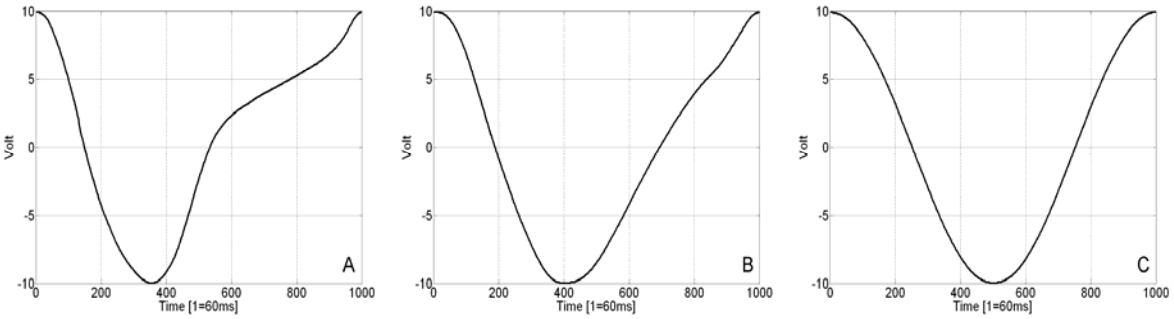

Figure 4.3. Standard waveforms used in experiments to run the ventricle. (A) 35% systolic ratio; **(B)** 40% systolic ratio and **(C)** 50% systolic ratio. All the waveforms are shown in a 60 bpm experiment.

4.3.3.3. Mitral recoil measurement

Recoil applied over the mitral valve [preventing it from movement in a cardiac cycle] was measured using a load cell positioned at the mitral entrance of the ventricular sac. The load cell was designed as a hollow disk letting the flow pass though it. The mitral valve was meticulously positioned over the sensitive area side of the load cell. The force signal generated from the load cell was transferred to an SGA strain-gauge transducer amplifier (*Interface, Inc. Scottsdale, AZ*). The amplified signal was captured by the Ni-DAQ system described earlier, together with the pressure and the flow signals. The load-cell was accurately calibrated with standard weights within its housing prior to the experiment.

4.3.3.4. Measurement of mitral valve open area

To capture the effective open area of the mitral valve in real-time, a high-speed digital camera (Photron FASTCAM-Ultima APX, *PHOTRON USA, INC***.** San Diego, CA) was used at 1000 frames per second (fps) which was synchronized with the pressure signal, trans-mitral flow and force measurements. The open area of the mitral valve in each fraction of second was computed from the acquired images (Figure 4.4) using a *MATLAB* code *(Mathworks Inc.*) specifically written for this study.

4.3.3.5. Computation of formation time

Early diastole consists of early rapid filling phase and mid-diastole or diastases which continues until the beginning of the atrial contraction phase. In echocardiography, early diastolic flow is characterized by an E-wave which represents the trans-mitral jet velocity. However, as a convention, the duration of early diastole is called the “E-wave” by cardiologists. Vortex formation time was computed from early trans-mitral jet velocity and the instantaneous open diameter of the mitral valve[19]:

$$T^* = \int_0^t \frac{U_J(\zeta)}{D_S(\zeta)} d\zeta \qquad (4\text{-}2)$$

where U_J and D_S are instantaneous exit jet velocity and the effective valve diameter, respectively; and t is the duration of the trans-mitral jet. For trans-mitral jet during early diastole, maximum T^* can be regarded as a non-dimensional measure for the total duration of the E-wave.

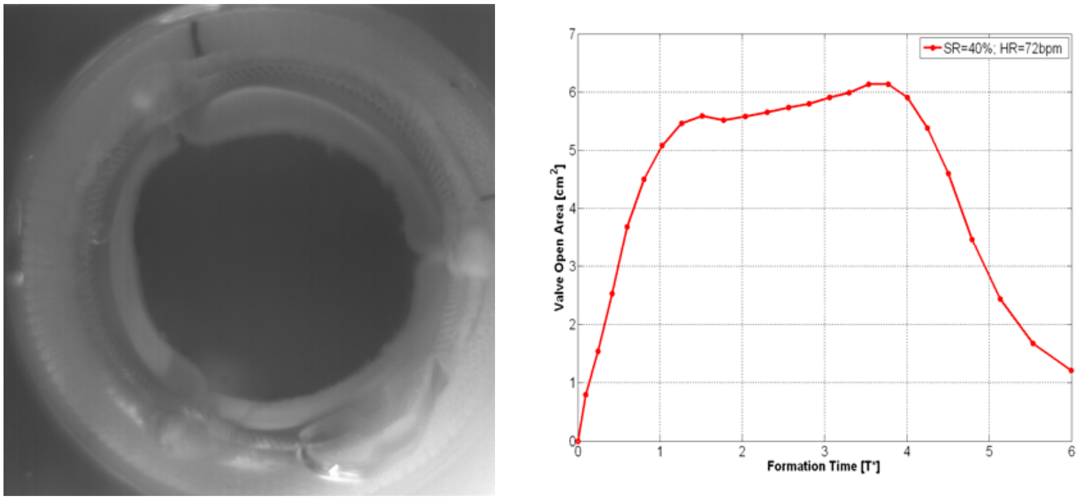

Figure 4.4. A clinical quality 27mm bioprosthetic valve at mitral position. Left. The image is taken when the valve was fully open during rapid filling phase. The excellent resolution of the image (1024x1024) with high frame rate (1000fps) makes the computation of effective open area as function time accurate. **Right.** Mitral valve open area as a function of formation time for 72 bpm: 40% SR.

4.3.4. Control volume analysis

An axisymmetric, fixed control volume (Ω) surrounding the trans-mitral jet flow in front of the mitral valve is shown in Figure 4.5. Assuming that the control volume allows the fluid external to the trans-mitral jet (residual fluid in LV) to be considered independent from the jet mechanism, making it explicit that the pressure at the mitral valve, and the recoil ($\mathbf{F_R}$) measured by the load cell can be regarded as the external forces between the jet and the ambient fluid acting on the mitral valve. Recoil ($\mathbf{F_R}$) is the force that restrains the valve from moving. In other words, Newton's third law guarantees that any force exerted on the control volume by the trans-mitral jet is also exerted on the trans-mitral jet by the control volume in an opposite direction, resulting recoil. Since the circulatory system is a closed system, gravitational forces are not applied to this control volume. Newton's second law for the control volume Ω is:

$$\sum \mathbf{F} = \rho \int_{\Omega} \frac{D}{Dt} \mathbf{U_J} dV + \int_{\partial\Omega} (P_V - P_A) \mathbf{n} dS + \mathbf{F_R} = 0 \qquad \text{(4-3)}$$

where $\mathbf{U_J}$ is the instantaneous exit jet velocity vector, $\mathbf{n}$ is the unit outward normal, dS is the area element, dV is the volume element, P_V is the LV pressure and P_A is the ambient pressure at the atrium. Thrust ($\mathbf{R}$) generated by trans-mitral flow is the rate of change of momentum of the fluid transferred from atrium to the ventricle:

$$\mathbf{R} = \rho \int_{\Omega} \frac{D}{Dt} \mathbf{U_J} dV = \rho \int_{\partial\Omega} \mathbf{U_J} (\mathbf{U_J} . \mathbf{n}) ds + \rho \frac{\partial}{\partial t} \int_{\Omega} \mathbf{U_J} dV \qquad \text{(4-4)}$$

The thrust ($\mathbf{R}$) should also balance the pressure forces applied to the control volume exerted at the valve level. From (4-3) and (4-4) e the thrust ($\mathbf{R}$) can be computed as the vector summation of recoil ($\mathbf{F_R}$) and the pressure forces:

$$\mathbf{R} = -\left(\int_{\partial\Omega} (P_V - P_A)\mathbf{n}\,dS + \mathbf{F_R}\right) \qquad (4\text{-}5)$$

4.4. Results

4.4.1. Pressure drop during isovolumic relaxation phase

Isovolumic relaxation (IVR) phase is the first part of diastole during which both valves are closed while the LV pressure is decaying as the volume of the chamber is constant. For each run, pressure drop during IVR was recorded and regressed to an exponential decaying function:

$$P(t) = P_0 \exp\left(\frac{-t}{\tau}\right) \qquad (4\text{-}6)$$

where *P(t)* is the ventricular pressure, *P₀* is the end-systolic pressure, τ (tau) is the pressure drop time-constant and *t* is the time. By increasing the heart rate in each group of different systolic ratios (SR), the magnitude of the pressure drop time constant decreased. Increasing the heart rate induces a faster pressure drop and improves the LV suction.

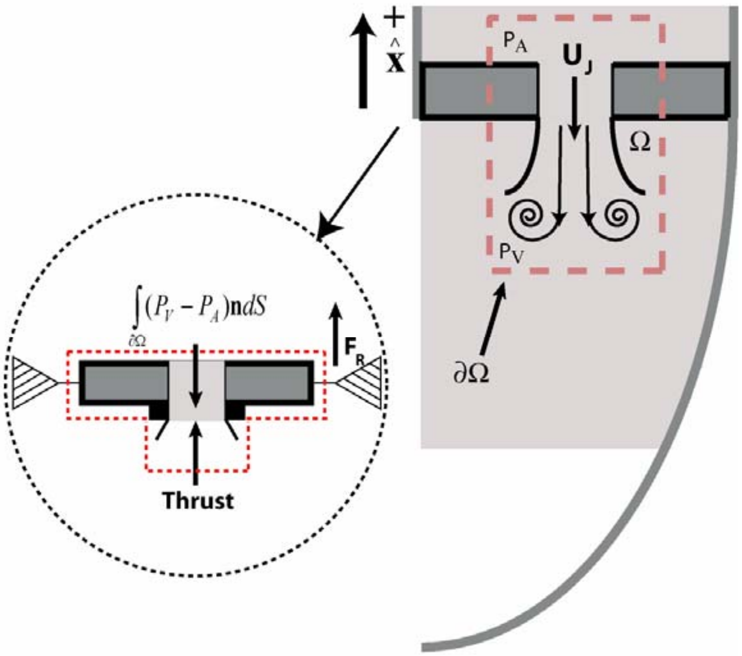

Figure 4.5. Control volume (Ω) for trans-mitral flow and the corresponding force diagram. $\mathbf{U_J}$ is the instant trans-mitral jet velocity. Pressure forces and the recoil (**F_R**) measured by the load cell act on the control volume. Total thrust (**R**) is the rate of change of momentum of the trans-mitral flow. P_V is the LV pressure and P_A is the ambient pressure at the atrium.

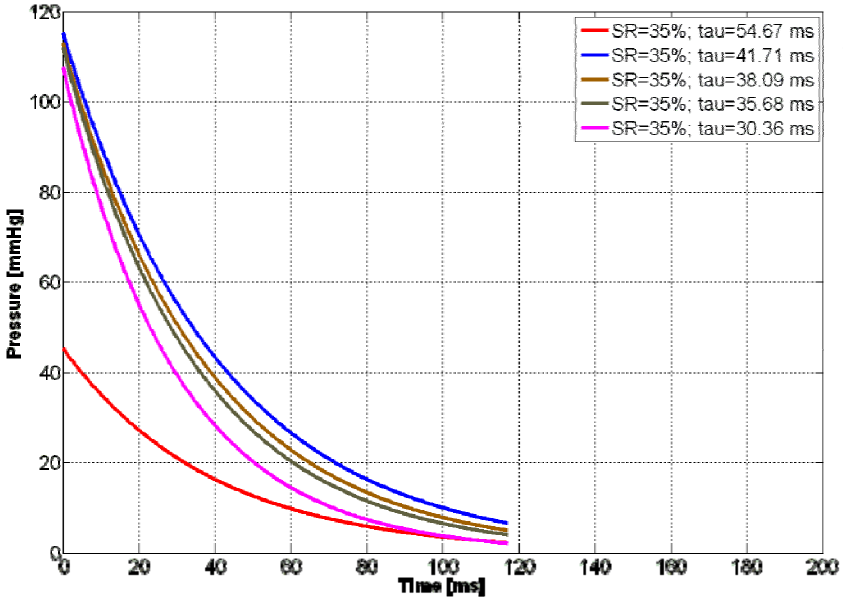

Figure 4.6. Left ventricular pressure drop during Isovolumic relaxation phase for the group of SR = 35%. Pressure drop time-constant (tau) has been computed from regression of the pressure to an exponential function. The details of the curve fitting are shown in Table 4.1.

P=P_0*exp(-t/tau))								
35% SR[‡]	**P_0 (mmHg)**	**95% CI**	**Tau^{-1}**	**95% CI**	**Tau (ms)**	**SSE[†]**	**Adjusted R^2**	**RMSE[§]**
30bpm	45.42	43.74, 47.10	0.01829	0.01728, 0.01930	54.6747	4835	0.9445	6.098
60bpm	115.4	111.5, 119.3	0.02397	0.02277, 0.02516	41.7188	9571	0.9628	9.286
72bpm	113.1	109.2, 116.9	0.02625	0.02495, 0.02755	38.0952	7594	0.9662	8.671
80bpm	112.1	108.4, 115.7	0.02802	0.02670, 0.02934	35.6888	6561	0.9704	8.06
100bpm	107.9	104.7, 111.0	0.03293	0.03155, 0.03432	30.3674	3581	0.9794	6.416

Table 4.1. Regression of pressure drop during isovolumic relaxation phase in 35% systolic ratio. SR: Systolic Ratio; SSE: Sum of Squared Errors; RMSE: Root Mean-Square Error.

P=P_0*exp(-t/tau))								
40% SR[‡]	**P_0 (mmHg)**	**95% CI**	**Tau^{-1}**	**95% CI**	**Tau (ms)**	**SSE[†]**	**Adjusted R^2**	**RMSE[§]**
30bpm	47.45	46.07, 48.84	0.01168	0.01115, 0.01222	85.6164	3907	0.9427	0.9423
60bpm	122.4	117.0, 127.9	0.01449	0.01349, 0.01549	69.0131	36550	0.9039	0.9033
72bpm	119.9	114.7, 125.1	0.01894	0.01771, 0.02017	52.7983	23940	0.9284	0.9278
80bpm	119.7	114.6, 124.9	0.02294	0.02148, 0.02440	43.5920	18700	0.9394	0.9389
100bpm	113.8	108.1, 119.4	0.02495	0.02301, 0.02689	40.0802	10740	0.9307	0.9298

Table 4.2. Regression of pressure drop during isovolumic relaxation phase in 40% systolic ratio. SR: Systolic Ratio; SSE: Sum of Squared Errors; RMSE: Root Mean-Square Error.

P=P_0*exp(-t/tau))								
50% SR[‡]	**P_0 (mmHg)**	**95% CI**	**Tau^{-1}**	**95% CI**	**Tau (ms)**	**SSE[†]**	**Adjusted R^2**	**RMSE[§]**
30bpm	46.85	45.37, 48.33	0.01384	0.01318, 0.01450	72.2543	3698	0.9448	0.9445
60bpm	116.3	112.5, 120.0	0.01776	0.01689, 0.01862	56.3063	14340	0.9545	0.9542
72bpm	114.6	111.2, 117.9	0.02097	0.02009, 0.02186	47.6872	10020	0.9681	0.9679
80bpm	112.7	109.7, 115.6	0.02230	0.02145, 0.02314	44.8430	7319	0.9753	0.9751
100bpm	108.7	106.1, 111.3	0.02362	0.02284, 0.02441	42.3370	4949	0.9816	0.9814

Table 4.3. Regression of pressure drop during isovolumic relaxation phase in 50% systolic ratio. SR: Systolic Ratio; SSE: Sum of Squared Errors; RMSE: Root Mean-Square Error.

Figure 4.7. Left ventricular pressure drop during isovolumic relaxation phase for the group of SR = 40%. Pressure drop time-constant (tau) has been computed from regression of the pressure to an exponential function. The details of the curve fitting are shown in Table 4.2.

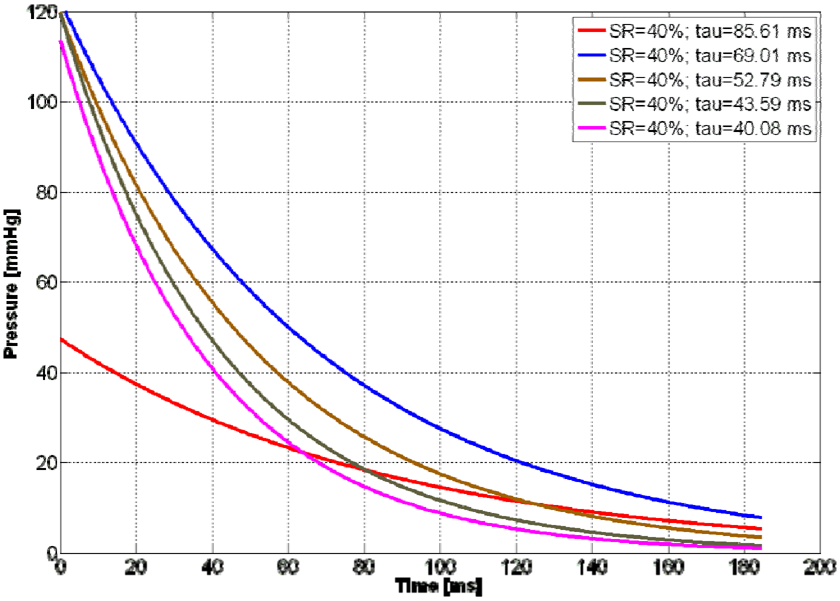

The range of pressure drop time-constants (tau) for 35% systolic ratio was between 30.36ms for 100 beat per minute (bpm) and 54.67ms for 30bpm (Figure 4.6 and Table 4.1). The range of tau for 40% systolic ratio was between 40.08ms for 100bpm and 85.61ms for 30bpm (Figure 4.7 and Table 4.2). Pressure drop time-constants for 50% systolic ratio (equal duration of systole and diastole) was in the range of 42.33ms for 100bpm and 72.25ms for 30 bpm (Figure 4.8 and Table 4.3).

4.4.2. Formation time

Formation time (*T**) as a non-dimensional measure for the duration of early diastole (E-wave) was computed from equation (4-2) using instantaneous exit jet velocity and the corresponding mitral valve open diameter as a function of time. The results for each experiment are summarized in Table 4.4. The range of E-wave duration in scale of formation time for the group of SR=35% was between 4.50 and 7.66; for the group of SR=40% was between 4.10 and 6.59 and, for the group SR=50% was between 5.56 and 7.83 (Table 4.4).

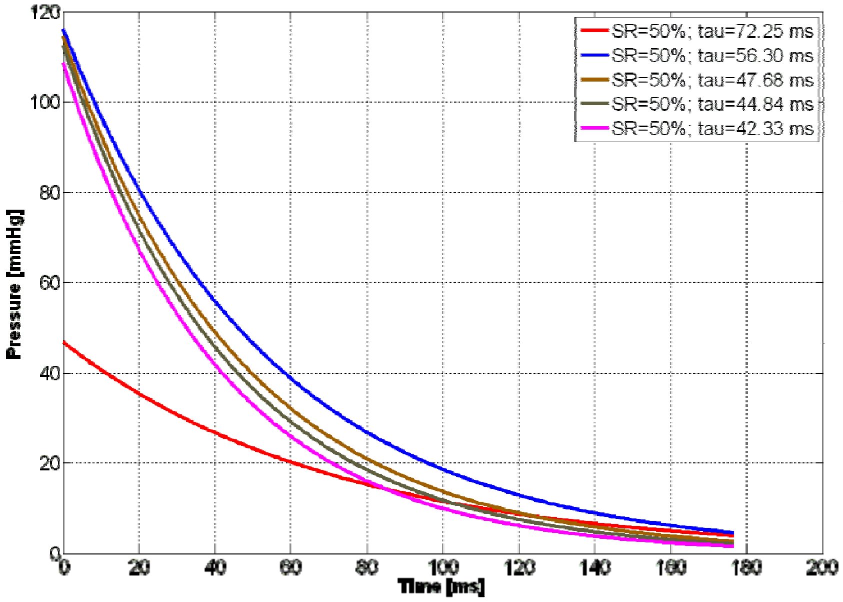

Figure 4.8. Left ventricular pressure drop during Isovolumic relaxation phase for the group of SR = 50%. Pressure drop time-constant (tau) has been computed from regression of the pressure to an exponential function. The details of the curve fitting are shown in Table 4.3.

4.4.3. Correlation between formation time and pressure drop time-constant

Pressure drop time constant (tau) was computed for each experiment as described in sections 4.3.3.2 and 4.4.1. Magnitude of maximal T^* and tau in milliseconds are provided in Table 4.4. Figure 4-9 depicts T^* (the non-dimensional duration of early diastole) plotted in a scatter diagram with tau (τ). The logarithmic regression was applied to formation time data versus tau. The best-fit logarithmic equation for this data was approximately: $T^* = 3.834\,Log(\tau) - 9.141$ with correlation coefficient of 0.9693 (Table 4.5).

SR	**Formation time (T*)**					**Tau (ms)**				
	30 bpm	**60 bpm**	**72 bpm**	**80 bpm**	**100 bpm**	**30 bpm**	**60 bpm**	**72 bpm**	**80 bpm**	**100 bpm**
35%	6.5947	5.0263	4.7014	4.1852	4.1062	54.6747	41.7188	38.0952	35.6888	30.3674
40%	7.6678	6.8931	6.1499	5.3762	4.5041	85.6164	69.0131	52.7983	43.592	40.0802
50%	7.1885	6.5755	6.1127	5.6942	5.2335	72.2543	56.3063	47.6872	44.843	42.337

Table 4.4. Formation time and pressure drop time-constant computed for each experiment. SR: systolic ratio; Tau: pressure drop time-constant.

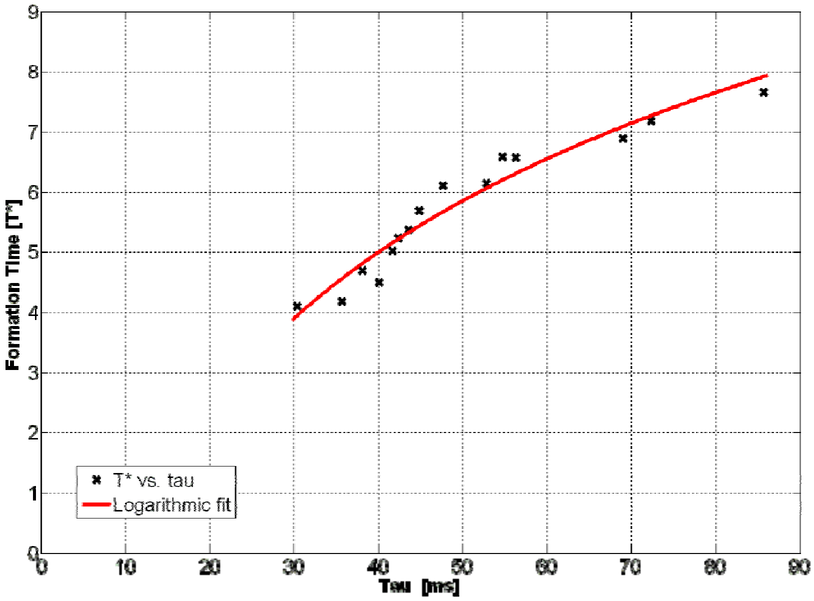

Figure 4.9. Non-dimensional duration of early diastole (T*) plotted in a scatter diagram with tau (τ). A logarithmic regression was applied to formation time data versus tau. The goodness of fit and information about the fit coefficients are provided in Table 4.5.

4.4.4. Thrust as a function of formation time

Recoil applied to the mitral valve was measured in real time with a load cell as described earlier in Section 4.3.3.3. The vector summation of recoil ($\mathbf{F_R}$) and the pressure forces applied to control volume (Figure 4.5) was computed as the trans-mitral jet thrust (**R**) for each case (4-5). Maximal thrust for each experiment along with its corresponding non-dimensional duration of early diastole (T^*) are summarized in Table 4.6.

The time-averaged thrust ($\overline{\mathbf{R}}$) of the trans-mitral jet during rapid filling phase can be regarded as an evaluation tool for the LV as a suction pump. The averaged thrust during early trans-mitral jet was computed as:

$$\overline{\mathbf{R}} = \frac{1}{T_{Jet}} \int_0^t \mathbf{R} d\zeta \qquad (4\text{-}7)$$

where T_{jet} is the duration of trans-mitral jet (E-wave) and **R** is the thrust.

For comparison purposes, evolution of time-averaged thrust for each case was plotted against formation time for each group in Figures 4-10 to 4-12.

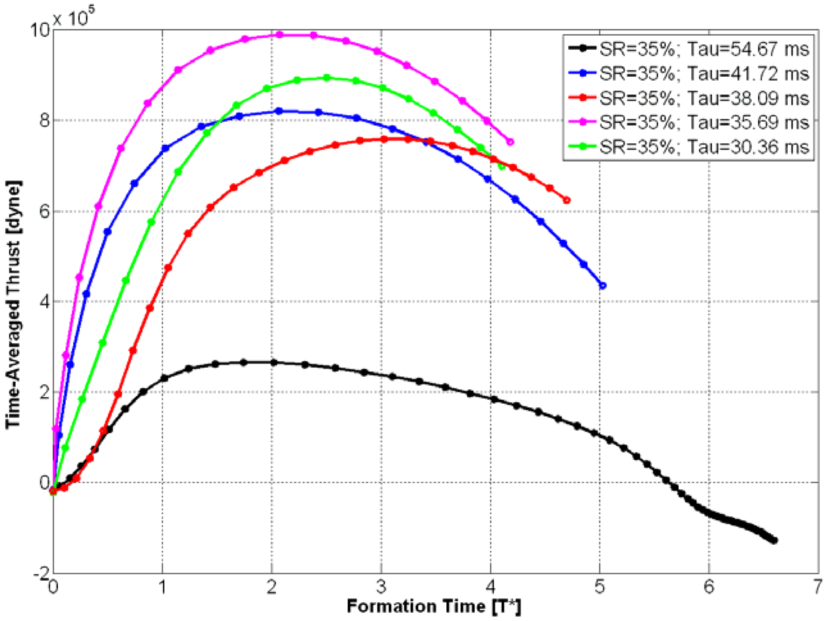

Figure 4.10. Time averaged thrust for 35% SR group during early diastolic flow.

4.4.5. Correlation between maximal thrust and the formation time

Magnitude of maximal trans-mitral thrust (**R**) during early diastole was plotted in a scatter diagram with non-dimensional duration of E-wave (T*) for each case (Figure 4.13). A second-order polynomial regression was applied to the maximal thrust data versus formation time. The best quadratic polynomial equation that fit this data was computed as: $R = -10^5 (1.124\,(T^*)^2 - 9.863\,(T^*) + 8.038)$ with R-squared of 0.7856 (Table 4.5). The maximal thrust in dyne and T* for each case are provided in Table 4.6.

y	x	Regression	A	95% CI	B	95% CI	CC	R^2
T*	Tau	y=A*Log(x)+B	3.834	3.251, 4.416	-9.141	-11.41, -6.875	0.9693	0.9396
R	Tau	y=A*exp(B*x)	3.446e+6	1.54e+6, 5.352e+6	-0.025	-0.038, -0.012	0.8240	0.6938
R	T*	$y=A*x^2+B*x+C$	-1.124e+5	-2.221e+5, -2650	9.86e+5	2.877e+5, 2.26e+6	-	0.7856

Table 4.5. Regression analysis for the involved parameters. CI: confidence Interval; CC: Correlation Coefficient.

SR	Formation time (T*)					Peak Thrust (dyne)				
	30 bpm	60 bpm	72 bpm	80 bpm	100 bpm	30 bpm	60 bpm	72 bpm	80 bpm	100 bpm
35%	6.5947	5.0263	4.7014	4.1852	4.1062	4.76E+05	1.20E+06	1.22E+06	1.44E+06	1.37E+06
40%	7.6678	6.8931	6.1499	5.3762	4.5041	2.83E+05	9.45E+05	1.07E+06	1.10E+06	1.25E+06
50%	7.1885	6.5755	6.1127	5.6942	5.2335	1.72E+05	8.54E+05	1.12E+06	1.24E+06	1.64E+06

Table 4.6. Formation time and peak recoil computed for each experiment. SR: systolic ratio.

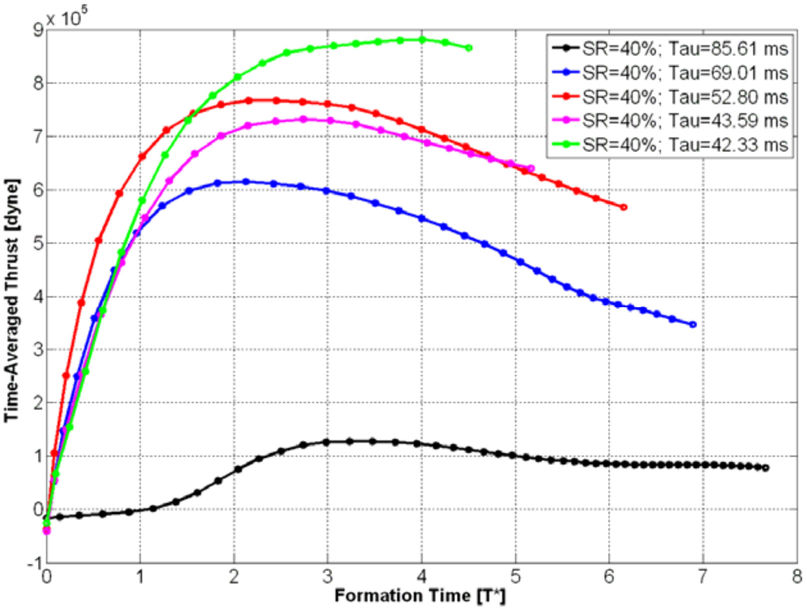

Figure 4.11. Time averaged thrust for 40% SR group during early diastolic flow.

Figure 4.12. Time averaged thrust for 50% SR group during early diastolic flow.

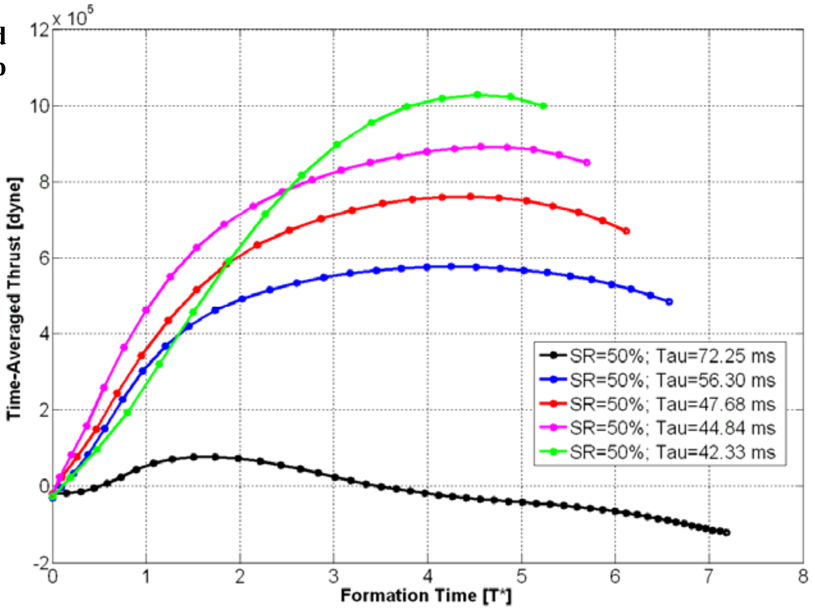

4.4.6. Correlation between maximal thrust and the pressure drop time-constant

Figure 4.14 depicts the maximal trans-mitral jet thrust (**R**) computed from early diastolic flow in a scatter diagram with the pressure drop time-constant (tau) for each experiment. An exponential regression was applied to the maximal thrust versus tau. The best exponential equation that describes the relation between two parameters was computed as $R = 3.46e006\exp(-0.025\tau)$ with the correlation coefficient of 0.8240. Magnitude of maximal thrust and tau for each case are provided in Tables 4.4 and 4.6.

4.5. Discussion

In Chapter 2, we used a simplified valve ess model for trans-mitral flow to study the presence of vortex ring formation. We observed that, while it was expected applying of a negative pressure (suction) to the LV base (annulus plane) would restrain the annulus plane from moving, the valve plane jumped in an opposite direction with respect to the flow[73]. By analyzing the vorticity field of the ejected flow, it was shown that the maximal recoil occurs once the formed vortex ring pinches off. We also showed that the size of mitral annulus is an important factor in magnitude of recoil and the duration of trans-mitral jet flow[73].

In Chapter 3, different sizes of bioprosthetic heart valves were positioned at the nozzle to inspect the influence of temporally variable motion of leaflets on the recoil motion of the annulus, and the vortex ring formation process. It was found that regardless of the size of the heart valve and regardless of the pressure drop time- constant, the recoil force computed from the annulus plane motion would be maximized once the vortex ring pinches off in a range of formation time between 3 and 5.

In the present study, we used a silicone sac that has comparable viscoelastic properties with the left ventricle. A bioprosthetic valve was placed at the aortic outlet of the sac to consider the effect of systole as well. This new experimental setup resulted in a more uniform pressure drop everywhere inside the sac (Figure 4.2). The previous studies (Chapters 2 and 3) did not take into account the systolic effect on the rapid filling phase.

However, the present study considered the effect of systole by experimentally simulating the systolic ratio and the flow disturbances due to the systolic ejection phase.

Figure 4.13. Maximal thrust plotted in a scatter diagram with Non-dimensional duration of early diastole (T*). A second-order polynomial regression was applied to recoil data versus formation time. The goodness of fit and information about the fit coefficients are provided in Table 4.5.

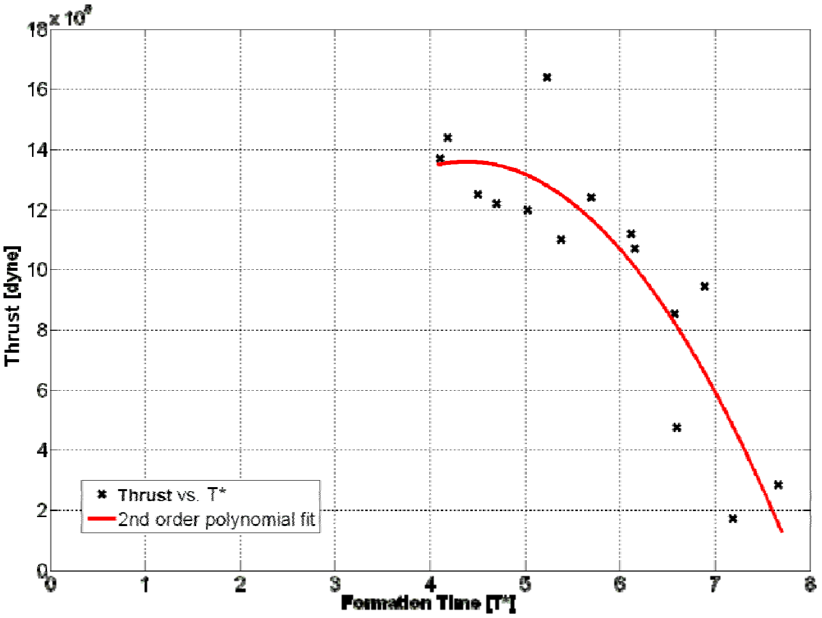

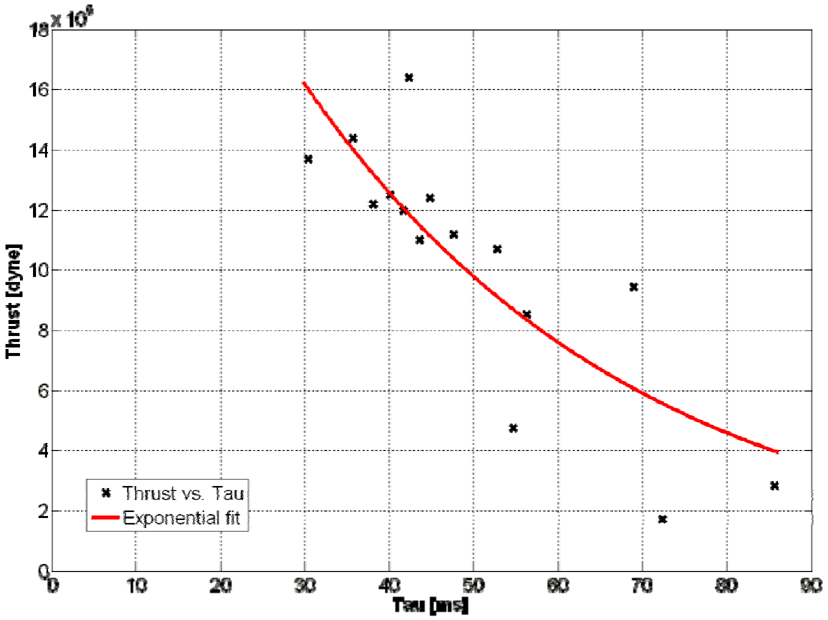

Figure 4.14. Maximal thrust plotted in a scatter diagram with pressure drop time-constant (tau). An exponential function was used to regress the two groups of data. The goodness of the fit and information about the fit coefficients are provided in Table 4.5.

4.5.1. Impact of suction on formation time

We categorized the experiments in three different groups based on the shape of waveforms (Figure 4.3) that generate the cardiac cycle. For all the considered groups, increasing the heart rate resulted in a smaller pressure drop time-constant which led to a faster pressure drop (Figures 4.6 to 4.8).

For a systolic ratio of 35%, a 30 beats per minute (bpm) heart rate (HR) produced a virtually slow pressure drop (tau= 54.67ms). This slow pressure drop resulted in a remarkably prolonged duration of early trans-mitral flow in scale of formation time (T^*=6.59; Table 4.4). The faster heart rate in this group (100bpm) resulted in tau= 30.67 ms and T^*=4.10. Increasing the heart rate would decrease the tau, resulting in a shorter non-dimensional duration of early diastole (Table 4.4).

In the group of 40% systolic ratio, an increase in magnitude of tau was observed by slowing down the heart rate for all the cases. The slower pressure drop increased the non-dimensional duration of the E-wave (Table 4.4). In the group of 50% SR, similar to the former two groups, increasing the heart rate decrease the pressure drop time-constant (tau) resulting in an increase in non-dimensional duration of the E-wave (Table 4.4).

Increasing the duration of the E-wave by reducing the systolic ratio[†††] extended the non-dimensional duration of early diastole (T^*) for each experiment with similar heart rates. However, shape of the waveform did not show to be correlated with the magnitude of tau. On the other hand, non-dimensional duration of the E-wave was strongly correlated with the pressure drop time-constant (tau). In Figure 4-9, it is shown that for a physiologic

---

[†††] Refer to section 4.3.2 for further information about the duration of E-wave generated by each waveform.

range of tau[84,85], the formation time lies in a range of 4-5.5 which is an optimal range for vortex ring formation.

4.5.2. Influence of formation time on mitral valve thrust

The time-averaged thrust within the early diastolic phase of a cardiac cycle is an indicator of the total momentum transferred to the LV by trans-mitral jet[86]. In the group of 35% SR, maximal averaged thrust was observed in the cases of 80bpm and 100bpm. In both cases, the E-wave was completed around the formation time range of $T^*\approx 4$. By increasing the formation time beyond $T^*=5$, the magnitude of the averaged thrust dropping 80% below the cases where the early diastole completed in formation time range of $T^*\approx 4$ (Figure 4.10).

For the group of 40% SR, the experiment in which the E-wave completed in less than $T^*=5$ attained the maximum thrust among the group. Increasing the formation time further than $T^*=6$ resulted in a drastic fall in magnitude of the thrust (Figure 4.11).

Within the group of 50% SR, the case in which the E-wave completed around $T^*\approx 5$ reached the maximal thrust (Figure 4.12). Increasing T^* beyond 6 resulted in a decline in magnitude of averaged thrust. However, increasing T^* further than $T^*=7$ ended in a significant drop in time-averaged thrust (Figure 4.12).

Regressing the scattered diagram of time-averaged thrust versus non-dimensional duration of the E-wave to a quadratic polynomial (Figure 4.13), shows that the thrust reaches to a peak when formation time (T^*) is in the range of 4 and 5 regardless of the shape of the waveform or the value of tau. The results obtained from this study along with the fact that increasing formation time greater than the range of 3.5 to 5, does not add any additional energy or circulation to the ejected leading vortex ring [16] strongly support the hypothesis that formation of a vortex ring has a major contribution in thrust generation during early diastole.

4.6. Conclusion

The non-dimensional duration of early diastole *(T*)* is an important parameter that influence the quality of ventricular filling. If the non-dimensional duration of early diastole increases due to any type of disorder (mitral stenosis, bradycardia, etc.), the trans-mitral thrust will be dramatically affected which can influence the magnitude of mitral valve recoil.

4.7. Limitations

The most important limitation of this study is the fact that we did not take the effect of muscle contraction into account. The rate of change of elastic and damping modulus of the ventricular muscles, as well as mitral valve papillary muscles, can actively affect the LV expansion during rapid filling phase and/or the mitral valve recoil. In the next chapter, a novel technique to assess the LV viscoelastic behavior based on ventricular harmonic motion would be discussed.

CHAPTER FIVE

Assessment of Left Ventricular Viscoelastic Components based on Ventricular Harmonic Behavior[§]

5.1. Chapter Abstract

Background. Assessment of left ventricular (LV) function with an emphasis on contractility has been a challenge in cardiac mechanics during the recent decades. The LV function is usually described by the LV pressure-volume (P-V) relationship. Based on this relationship, the ratio of instantaneous pressure to instantaneous volume is an index for LV chamber stiffness. The standard P-V diagrams are easy to interpret but difficult to obtain and require invasive instrumentation for measuring the corresponding volume and pressure data. In the present study, we introduce a technique that can estimate not only the elastic component but also the viscous properties of the LV based on oscillatory behavior of the ventricular chamber and it can be applied non-invasively as well. *Materials and Methods.* The estimation technique is based on modeling the actual long

---

[§] This paper is published as “Kheradvar A, Milano M, Gorman RC, Gorman III JH, Gharib M. Assessment of left ventricular viscoelastic components based on ventricular harmonic behavior; *Cardiovascular Engineering*, 2006 March 6(1): 30-39” axis displacement of the mitral annulus plane toward the cardiac base as a linear damped oscillator with time-varying coefficients. Elastic deformations resulting from the changes in the ventricular mechanical properties of myocardium are represented as a time-varying spring, while the viscous components of the model include a time-varying viscous damper, representing relaxation and the frictional energy loss. To measure the left ventricular axial displacement ten healthy sheep underwent left thoracotomy and sonomicrometry transducers were implanted at the apex and base of the LV. The time-varying parameters of the model were estimated by a standard Recursive Linear Least Squares (RLLS) technique. *Results*. LV stiffness at end-systole and end-diastole was in the range of 61.86-136 dyne/g.cm and 1.25-21.02 dyne/g.cm, respectively. Univariate linear regression was performed to verify the agreement between the estimated parameters, and the measured values of stiffness. The averaged magnitude of the stiffness and damping coefficients during a complete cardiac cycle were estimated as 58.63±12.8 dyne/g.cm and zero dyne.s/g.cm, respectively. *Conclusion*. The results for the estimated elastic coefficients are consistent with the ones obtained from force-displacement diagram. The trend of change in the estimated parameters is also in harmony with the previous studies done using P-V diagram. The only input used in this model is the long axis displacement of the annulus plane, which can also be obtained non-invasively using tissue Doppler or MR imaging.

5.2. Introduction

Assessment of left ventricular function with an emphasis on contractility has been a major challenge in cardiac mechanics during the recent decades. To date, extensive work has been done to develop models describing left ventricular (LV) dynamics. An excellent series of publications by Suga and Sagawa[87], Yellin[22,42] , Weiss[21], Peskin[88] and other researchers ultimately resulted in a more precise conceptual understanding of how the heart works. However, an applicable model that can differentiate between different pathophysiological states based on mechanical properties of the heart is still needed.

In regards to describing ventricular function, Suga and Sagawa introduced a diagram for instantaneous ventricular pressure-volume (P-V) relationship. Based on their diagram[87], they described the ratio of instantaneous pressure to instantaneous volume ($P(t)/(V(t)-V_d)$) as the time varying stiffness of ventricular chamber. The standard P-V diagrams are easy to interpret and give a rough estimate of the mechanical work done by the LV[89]. However, the pressure and the corresponding volume of the LV need to be measured invasively using sophisticated techniques, such as intravascular micromanometers and conductance catheters[90], which restrict the clinical applications of this model. Furthermore, this model ignores the viscoelasticity of the heart by not considering viscous damping. It has also been shown that although dp/dv provides a useful description of simultaneous LV pressure and volume events, it does not represent actual LV physical properties[91,92,93,94].

Table 5.1. **Abbreviations and acronyms**

x	longitudinal base to apex displacement
y	zero-mean displacement
$\overline{K}$	mean of stiffness coefficient
K_{ED}	end diastolic stiffness coefficient
K_{ES}	end systolic stiffness coefficient
$\overline{h}$	mean of damping coefficient
f_P	Force density
μ_K	mean of the mean of stiffness coefficient
μ_h	mean of the mean of damping coefficient
i	sample index
$\mathbf{P}_i$	covariance matrix of the estimated parameters
λ	smoothing (forgetting) factor
e_i	estimation error
$\mathbf{G}_i$	adaptive estimator gain
$\boldsymbol{I}$	identity matrix
t	time

Templeton and Nardizzi[95] implemented a different model based on perturbations of left ventricular pressure and volume. They described a second order linear differential equation for pressure with ventricular volume displacement as the model input. The model was then used to describe nominal elastic and viscous coefficients for the ventricle. However, their time varying coefficients were computed from an externally applied sinusoidal volume change rather than the naturally existing absolute volume and pressure of the ventricle. Additionally, this model was also dependant on obtaining LV pressure data in response to some LV volume perturbations, which makes the model almost impossible to use for clinical applications.

Recently Campbell, et al.[96] proposed a novel mathematical model that relates LV pressure-volume relationships to cardiac myocyte force-length dynamics in rat's hearts. This sophisticated model makes the beating heart amenable to studies that aim the relevance of myofilament contractile behavior to cardiac system function. However, the parameters inferred from this model mostly reflect the contractile parameters at cellular level rather than global state of the heart.

A more applicable model for diastolic function that uses Doppler velocity profile input has been developed by Kovács, et al.[97]. Their motivation was the similarity between the left ventricle during diastole as a suction pump and a damped harmonic oscillator. They used a linear differential equation that describes the motion of a forced, damped harmonic oscillator with constant coefficients. The forcing term of the model was set to zero during early diastole and to a sinusoidal forcing term during atrial contraction. Kovács, et al. used an approximation of the trans-mitral jet velocity obtained from Doppler echocardiography to validate their model. Despite the fact that their model only describes diastolic function, the major advantage of the Kovács model to other existing ones is its simplicity. However, recent technological advances in ultrasound techniques allow for accurate, direct measurements of annulus displacement, thus paving the way for the use of more sophisticated modeling techniques, capable of describing the entire cardiac cycle.

In the present study, we use a technique to assess the LV contractile behavior during the entire cardiac cycle. The estimation technique is based on modeling the actual long axis displacement of the mitral annulus plane toward the cardiac base as a linear damped oscillator with time-varying coefficients. We derive longitudinal rather than global indexes of stiffness and damping of the left ventricle. Elastic deformations resulting from the changes in the ventricular mechanical properties of myocardium are represented as a time-varying spring. The viscous components of the model include a time-varying viscous damper, representing relaxation and the frictional energy loss. Thus, one would expect the ventricular viscous properties to reflect the force-velocity behavior of cardiac muscle translated into ventricular level[98]. The nominal oscillator also has structural similarities to internal viscoelastic loading in papillary muscles[99,100] and myocytes resembling Voigt's model of viscoelasticity[101].

5.3. Method

5.3.1. Mathematical model

Longitudinal displacement of the mitral annulus plane toward the apex during a cardiac cycle was considered analogous to the motion of a damped harmonic oscillator with time-varying coefficients. The time dependency of the coefficients is an advantage of this model to the existing ones[97,102] and allows the model to describe systole, diastole and the transitional isovolumic phases of the cardiac cycle. This is consistent with the fact that the LV acts as two distinct pumps in a cardiac cycle; acting as a suction pump[103,104,105,106] during diastole and as a positive displacement pump during systole in which the pressure in the chamber depends on the walls displacement and the blood volume[107,108].

Due to the natural time-dependency of the LV mass (blood and tissue), identification of LV mass, separated from the rest of the heart, as a function of time was impractical. Therefore, the equation of motion for a linear harmonic oscillator with time varying coefficients was divided by the instantaneous mass of the system and rewritten as:

$$\ddot{y} + h(t)\dot{y} + K(t)y = 0 \qquad (5\text{-}1)$$

where (*y*) is the zero-mean displacement of the system and (*x*) is the longitudinal base to apex displacement (Table 5.1):

$$y = (x - \bar{x}) \quad (5\text{-}2)$$

The bar indicates mean value, the dot denotes differentiation with respect to time and "*h"* and *"K"* are the damping and elastic (stiffness) coefficients per unit mass, respectively. Equation (5-1) can also be reorganized to a constant-coefficient harmonic oscillator with time varying forcing term, as follows:

$$\ddot{y} + \bar{h}\dot{y} + \bar{K}y = (\bar{h} - h(t))\dot{y} + (\bar{K} - K(t))y \quad (5\text{-}3)$$

In (5-3), "$\bar{h}$" and "$\bar{K}$" are the averaged values of damping (*h*) and stiffness (*K*) coefficients during a cardiac cycle, respectively. The function on the right-hand side of (3) is the intrinsic forcing function, which can be a representative of contractile elements of the left ventricle[109,110,111]. The intrinsic forcing function is described as:

$$f(t) = (\bar{h} - h(t))\dot{y} + (\bar{K} - K(t))y \quad (5\text{-}4)$$

Considering that we measure the longitudinal displacement "*x(t)*", the parameters in this model, as well as the forcing function, can be estimated by using a standard identification technique[112], which will be described in details after the description of the data acquisition procedure.

5.3.2. Animal preparation

In order to assess the model behavior, an animal study with limited cases was performed with Dorset sheep. Animal data was collected at the Harrison department of surgical research, University of Pennsylvania School of Medicine. Animals were treated under an experimental protocol approved by the University of Pennsylvania's Institutional Animal Care and Use Committee (IACUC) and in compliance with NIH publication No. 85-23, as revised in 1985. Animals were induced with Thiopental sodium (10 to 15mg/kg intravenously [IV]) and intubated. Anesthesia was maintained with Isofluorane (1.5% to 2%) and oxygen. All animals received Glycopyrrolate (0.4mg IV) and Enrofloxin (10 mg/kg IV) on induction. To measure the left ventricular axial displacement and intraventricular pressure, ten healthy sheep between 35 and 45kg underwent left thoracotomy after induction of anesthesia. Sonomicrometry transducers (*1.0mm; Sonometrics Corp., London, Ontario, Canada*) were implanted at the apex and the base of the left ventricle to measure their mutual distance. The surface electrocardiogram (ECG), arterial blood pressure (ABP) and left ventricular pressure were continuously monitored and recorded. Left ventricular pressure was measured using a high-fidelity pressure transducer (*Spc-350, Millar Instruments Inc., Houston, TX*) inserted from the femoral artery into the left ventricle. Different phases of the cardiac cycle were defined based on the trend of $\frac{dP}{dt}$ in each case and the results confirmed by the ECG.

5.3.3. Equation of motion and parameter estimation

The relative displacements obtained from sonomicrometry transducers were substituted in equation (5-1). The problem of tracking the parameters was tackled by re-sorting to a class of recursive linear least squares algorithms[112]. To estimate the model parameters (Table 5.1), equation (1) was re-written as:

$$\ddot{y} = -h\dot{y} - Ky = \boldsymbol{\theta} \cdot \varphi^T \qquad (5\text{-}5)$$

where $\boldsymbol{\theta} = \{h, K\}^T$, and $\varphi = \{-\dot{y}, -y\}^T$. The coefficients $\boldsymbol{\theta}$ are estimated by a standard Recursive Linear Least Squares (RLLS) technique. Putting a 'hat' symbol on top of the estimated quantities, the RLLS equations read:

$$\mathbf{P}_{i+1} = \frac{1}{\lambda}\left(\mathbf{I} - \mathbf{G}_i \hat{\varphi}_i^T\right)\mathbf{P}_i \qquad (6)$$

where *i* denotes the sample index; ***I*** is the 2x2 identity matrix; $\mathbf{P}_i$ is the covariance matrix of the estimated parameters; $\mathbf{G}_i$ is the adaptive estimator gain; and the scalar λ adjusts the smoothing of the estimations (i.e. the closer λ to one, the smoother the estimation: typical values for this parameter are between 0.9 and 0.99). The adaptive estimator tracks the time varying coefficients, and then an estimation of the forcing term is obtained by computing the averaged coefficients and using equation (5-3). The model parameters are updated by computing the estimation error (e_i) for the second derivative, as follows:

$$e_i = \hat{\ddot{y}}_i - \boldsymbol{\theta}_i \cdot \hat{\varphi}_i^T \qquad (5\text{-}7)$$

The estimation error is used to update the estimate for the model parameters:

$$\boldsymbol{\theta}_{i+1} = \boldsymbol{\theta}_i + \mathbf{G}_i e_i \qquad (5\text{-}8)$$

where $\mathbf{G}_i$ is the linear estimator gain. The optimal value for the estimator gain $\mathbf{G}_{i+1}$ for use in the next step is computed as a function of the covariance matrix $\mathbf{P}_{i+1}$:

$$\mathbf{G}_{i+1} = \frac{\mathbf{P}_{i+1}\hat{\varphi}_i}{\lambda + \hat{\varphi}_i^T \mathbf{P}_{i+1}\hat{\varphi}_i}. \qquad (9)$$

The RLLS technique improves the parameter estimation by sequentially processing each sample. In order to make the estimator maximally responsive in the initial adaptation phase, the starting value for the covariance matrix $\mathbf{P}_0$ is set at $1000 \times \mathbf{I}$. The starting value for the parameters is chosen to be zero. Each step of the RLLS algorithm updates the covariance matrix of the predictions $\mathbf{P}_{i+1}$ by using current measurements, as in equation (5-6). The RLLS also improves the parameters estimation by predicting a measured quantity with (5-5), using current values of the parameters. Equation (5-7) computes the estimation error, which is used in equation (5-8) to improve the estimated parameter by means of an adaptive correction gain computed in equation (5-9).

Equation (5-1) is chosen as a continuous time model to make the physical interpretation of the parameters easier. However, in equations (5-6) through (5-9), discrete samples of the first and second derivatives of the measured displacement were used. Due to the presence of noise in the measured data and the effects of sampling rate, care was taken, while approximating these quantities with finite differences, to prevent the quantities from diverging. Söderström, et al.[113] thoroughly described the crucial choice of a suiTable estimator for the derivatives. In the present study, we use an estimator for the derivatives compatible with the RLLS technique[112].

5.4. Results

Based on our model, the system can be studied as an unforced damped harmonic oscillator with time-varying coefficients (5-1), or a forced damped harmonic oscillator with constant coefficients (5-3).

5.4.1. Unforced model with time-varying coefficients

Temporal evolutions in stiffness (elasticity) and damping of the system within a cardiac cycle is extracted from the unforced form of the oscillator (5-1). Stiffness and damping coefficients of the system for each individual case are estimated as a function of time, based on the RLLS algorithm [equations (5-6) through (5-9)]. Time evolution of the stiffness and damping coefficients used in the unforced form of the model are shown in Figures 5.1 and 5.2.

Since the estimated coefficients for "*K"* were obtained from a one-dimensional model of the left ventricle, their magnitudes represent longitudinal stiffness rather than the actual stiffness of the ventricle. Therefore, the magnitude of stiffness at the end-systole and the end-diastole do not have the same dimension as the results of the previous studies based on P-V curve[87,114,115]. However, to verify the accuracy of the results estimated by the model, we described a nominal force-displacement (f_P-x) diagram equivalent to Suga[87] and Sagawa's P-V diagram. In this diagram, instead of LV volume, long axis displacement is used and the pressure is replaced by the force density per unit mass (f_P), defined as LV pressure times unit area divided by the heart mass. The measured f_P of each case was plotted against the longitudinal displacement of the mitral annulus (Figure 5.3). Based on our definitions, the slopes of this curve at the end-systole and the end-diastole have a dimension equivalent to the estimated "*K".* The results for the oscillator's stiffness coefficient and f_P-x diagram stiffness at the end-systole and the end-diastole are provided in Table 5.2.

Univariate linear regression was performed to test the agreement between the model's estimation, and the measured values of "*K*" from f_P-x diagram. Bland-Altman analysis[116] was also employed to evaluate systematic bias in the correlation. Statistical analysis was performed using *STATA* statistical software (*version SE 8.00, STATA Corporation, College Station, Texas*).

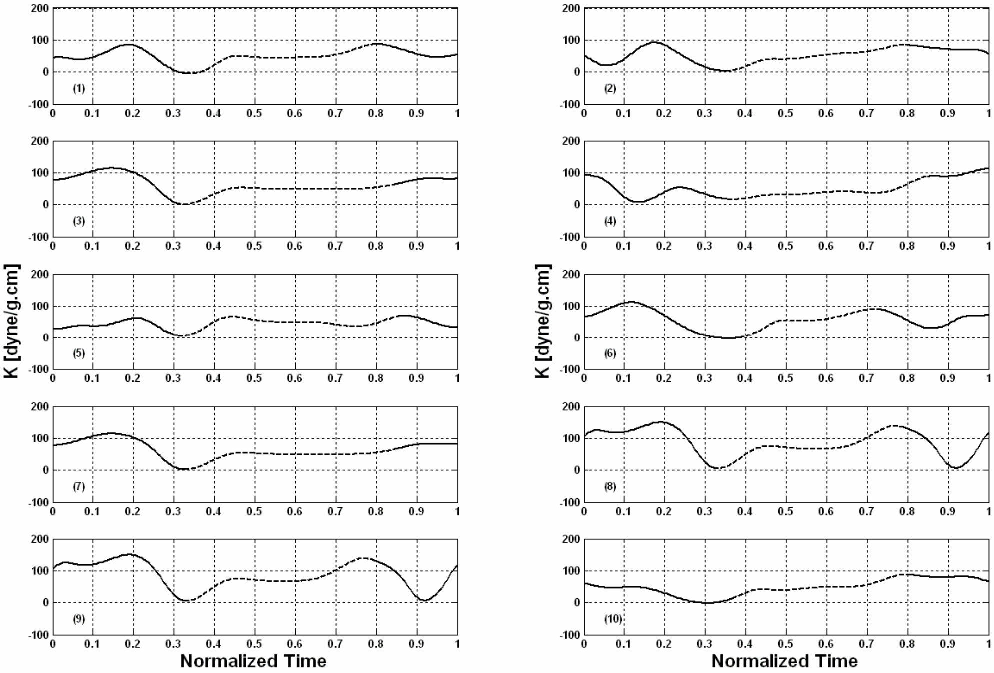

Figure 5.1. Time evolution of stiffness coefficients for all the 10 cases.

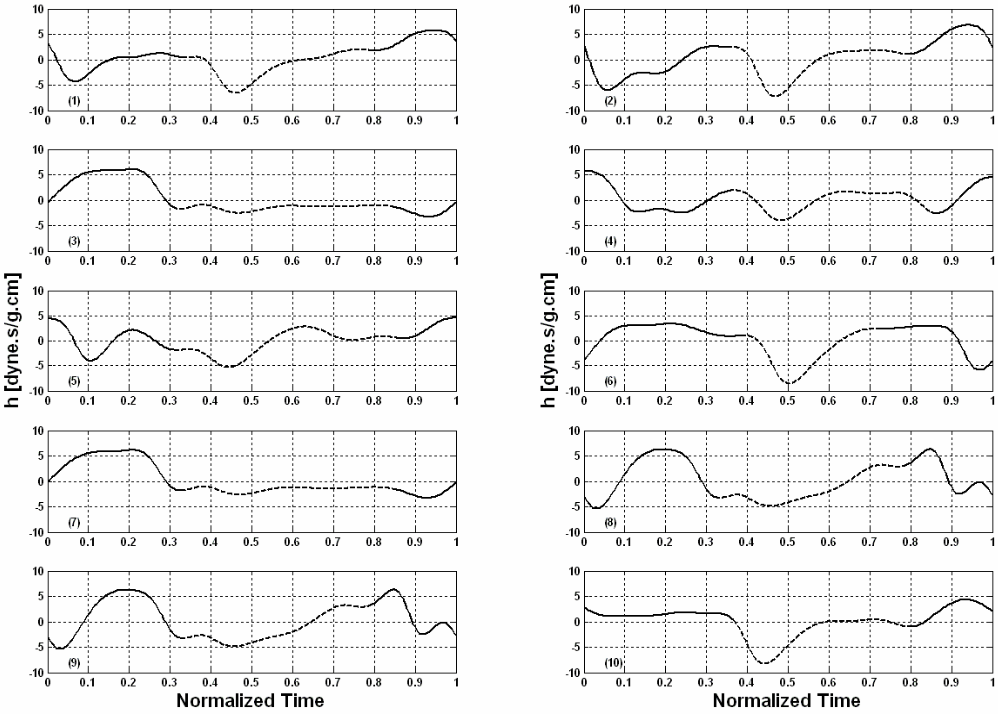

Figure 5.2. Time evolution of damping coefficients for all the 10 cases.

Figure 4 displays group regression and Bland –Altman plots for 10 comparisons between model-estimated stiffness and pressure-Displacement measured "*K*" at end-systole and end-diastole, respectively. The regression equation for K_{ES} was $K_{ES} = 0.5357 K_{ES_{fp-x}} + 42.3460$ (R^2=0.7141, p<0.002). Correlation coefficient between two data sets is 0.8450. The mean difference is 0.543 dyne/g.cm (p=0.910, 95% confidence interval: -10.03422**,** 11.12022) that is, no systematic bias. For K_{ED}, the regression equation is $K_{ED} = 0.7046 K_{ED_{fp-x}} + 2.8758$ (R^2=0.8253, p<0.00001). The correlation coefficient between two data sets is 0.9084. The mean difference is 0.675 dyne/g.cm (p=0.465, 95% confidence interval: -1.327367**,** 2.677367) and therefore, no systematic bias exists.

5.4.2. Forced model with constant coefficients

The forced form of the oscillator (5-3) provides information about the global (averaged) state of elasticity and damping of the system, in addition to the instantaneous intrinsic longitudinal force generated over a cardiac cycle.

Values of mean stiffness and damping coefficients for each case used in the forced form of the equation (5-3) are provided in Table 5.2. To determine whether the coefficients were from the same distribution and possessed the same mean, we applied Student's t-test for each sample of coefficients. For each coefficient of stiffness and damping, we calculated the mean of the means of all 10 cases, " μ_K "and" μ_h ", respectively.

Then the null hypothesis that each sample of coefficients had the same mean as " μ_K "and" μ_h " was tested. The estimated " μ_K "and" μ_h " for 10 healthy cases were

58.63±12.8 dyne/g.cm and zero dyne.s/g.cm, respectively. The p-value for each sample is shown in Table 5.2.

The forcing term of equation (5-3) was also computed based on (5-4), using the estimated parameters, zero-mean longitudinal displacement (y) and zero-mean longitudinal velocity ($\dot{y}$). Evolution of the forcing term within a cardiac cycle is shown in Figure 5.5. Incident of diastole and systole were determined based on simultaneous ECG and the LV pressure measurements

	$\overline{K}$ (dyne/g.cm)		$\overline{h}$ (dyne.s/g.cm)		K_{ES} (dyne/g.cm)		K_{ED} (dyne/g.cm)	
	magnitude	P-value	magnitude	P-value	measured	estimated	measured	estimated
Sheep1	49.11	0.16	0.05	0.90	74.5	85.81	2.15	2
Sheep2	51.32	0.50	0.02	0.90	98.33	83.83	8.73	5.84
Sheep3	62.39	0.39	0.09	0.68	70.35	61.86	3.12	1.25
Sheep4	47.16	0.12	0.01	0.64	96.67	89.64	12.2	16.62
Sheep5	44.40	0.05	0.04	0.79	74.17	68.74	5.69	4.8
Sheep6	56.86	0.83	0.04	0.79	100	86.41	4.33	5.43
Sheep7	63.62	0.15	0.07	0.70	71.52	66.86	5.2	3.42
Sheep8	83.40	0.05	0.12	0.68	111.25	134.5	11.22	7.07
Sheep9	83.48	0.05	0.12	0.68	111.25	136	10.59	7.07
Sheep10	47.84	0.06	0.02	0.85	97.83	86.79	18.04	21.02

Table 5.2. Magnitude of coefficients

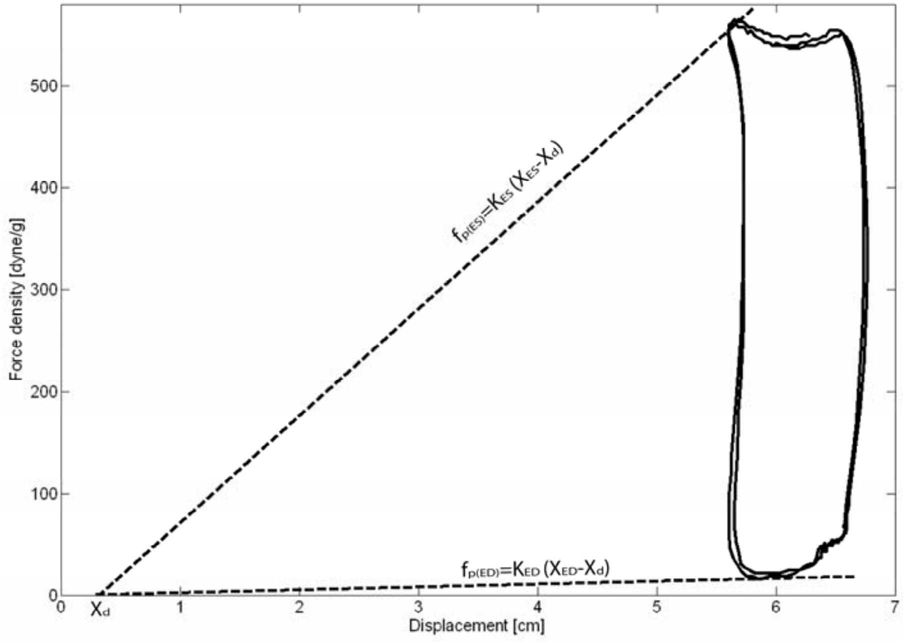

Figure 5.3. Plot of the force density of a representative case against the longitudinal displacement of the mitral annulus. See text for the definition of the force density (f_P). X_d is the axis intercept for the tangent lines.

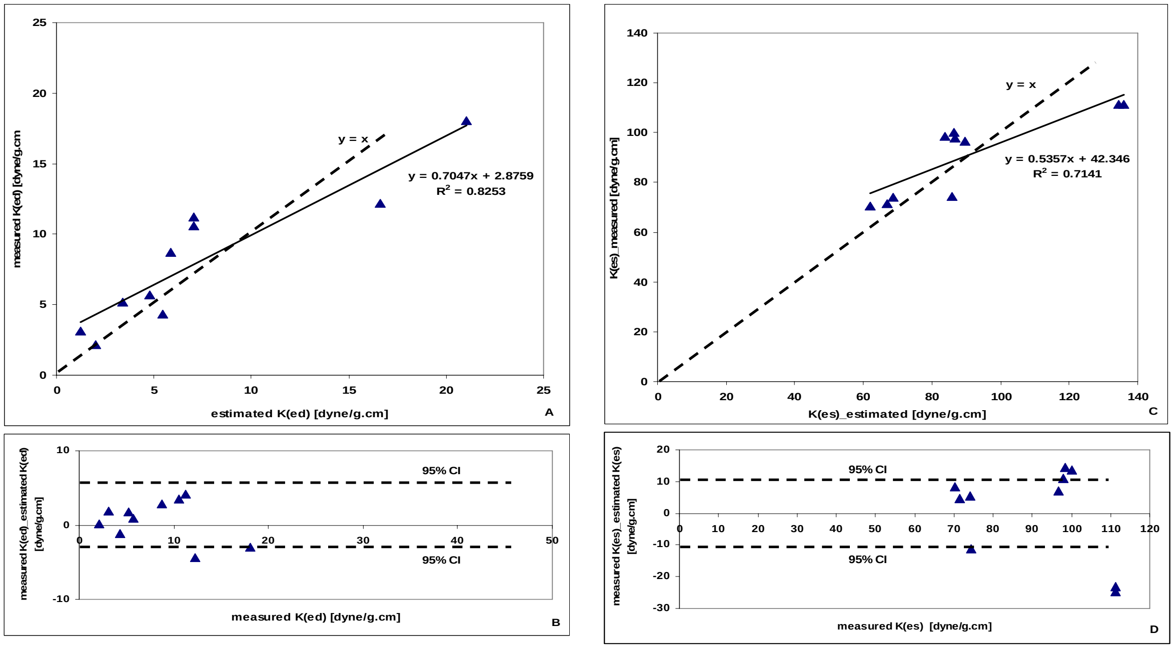

Figure 5.4. validation of the coefficients estimated by the model versus coefficients obtained from experiment. (A) Linear regression (solid line) and the line of identity (dotted line) comparing estimated left ventricular stiffness (K_{ED}) at end-diastole derived by harmonic oscillator model and by pressure-displacement diagram for 10 sheep. (B) Bland-Altman plot of difference between measured (K_{ED}) and estimated (K_{ED}) versus mean value. Mean and 95% confidence interval of the mean difference are shown. (C) Linear regression (solid line) and the line of identity (dotted line) comparing estimated left ventricular stiffness (K_{ES}) at end-diastole derived by harmonic oscillator model and by pressure-displacement diagram for 10 sheep. (D) Bland-Altman plot of difference between measured (K_{ES}) and estimated (K_{ES}) versus mean value. Mean and 95% confidence interval of the mean difference are shown.

5.5. Discussion

We developed a technique that employs a dynamic model for longitudinal displacement of the annulus plane toward the apex. Using this technique enables us to estimate longitudinal elastic and damping coefficients for the left ventricle based only on the mitral annulus displacement. Although the estimated values of coefficients were considered as one-dimensional parameters, their time-varying trends were consistent with the previous studies that considered dP/dV as an index of stiffness[87,115] and gave quantitative information about LV dynamics. The only input used in this model is the long axis displacement of the annulus plane, which can also be obtained non-invasively using tissue Doppler. The fact that the technique can be used as a non-invasive way to evaluate LV function is the key advantage of this model with respect to existing techniques.

As it can be observed in Figure 2, in all the cases, the stiffness of the model has a minimum at the end-diastole, increases during systole and reaches a maximal peak at the end-systole. This observation is consistent with the f_P-x diagram plotted based on measured data (Figure 5.3), with P-V diagram of Suga and Sagawa[87] and with the other models that describe LV stiffness based on P-V relationship[92,93,98,104,115].

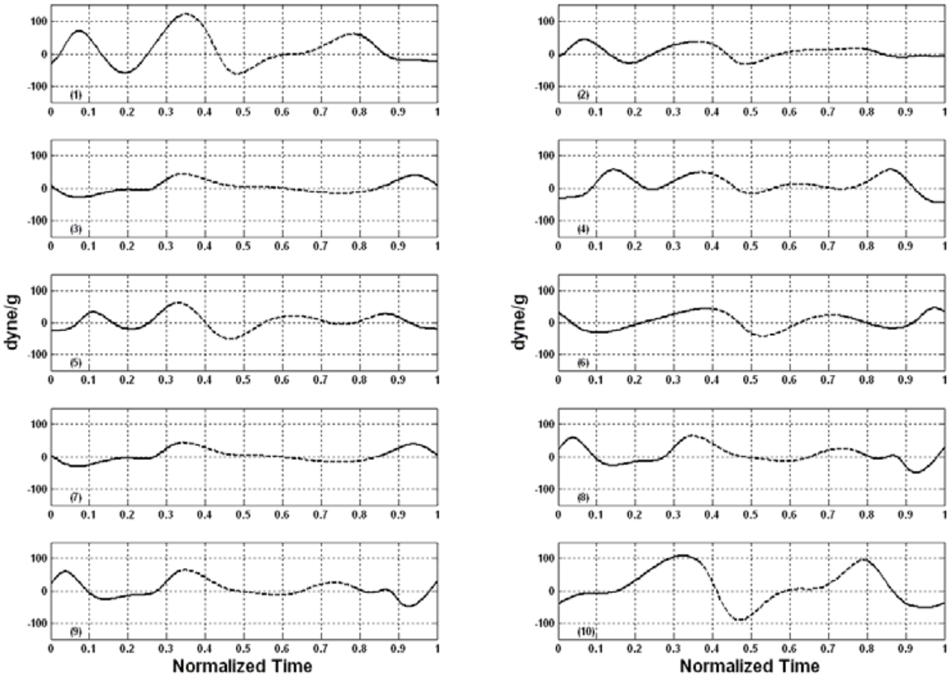

Figure 5.5. Time evolution of forcing term for all the 10 cases.

Estimation of damping coefficient gives additional information on ventricular contractile behavior with respect to the estimated elastic component data. The estimated damping coefficient for the system had a zero mean value, and its range of variation was between -10 and +10dyne.s/g.cm (Figure 5.3). The coefficient showed a negative peak during systole. Considering the fact that the stiffness coefficient is always positive and greater than the damping coefficient during systole (Figures 5.1 and 5.2), it can be inferred from the linearized stability analysis[117] that the equilibrium solution is unstable for each time point in which "h" is less than zero. This means that the displacement of the system grows (usually exponentially). This can be a justification for the sharp longitudinal displacement of the mitral annulus plane toward the apex during systole.

Although there are quite a number of published articles about the stiffness of LV chamber, less attention has been paid to viscous damping in the left ventricle. However, measured global damping of left ventricle over a cycle can also be used as an index for evaluation of cardiac functionality. Recent papers have studied the damping characteristics of myocardial contractile elements at cellular level[118,119]. Nevertheless, to our best knowledge, none have been published relating viscous damping at the cellular level to the global damping of the left ventricle as a continuum.

Time-varying behavior of stiffness and damping coefficients can be incorporated into an intrinsic forcing term (5-4) of an equivalent harmonic oscillator with constant coefficients (5-3). This forcing term shows periodic behavior over cardiac cycles and has a maximal positive peak at the end-diastole. However, other than the maximal peak at the end-diastole, no other features can be observed in common in all the cases (Figure 5.5). This may imply that the intrinsic forces generated by cardiac contractile elements are naturally complex and are not showing the same patterns in different hearts. Literature reports [109,110,111,118] suggest that myocardial contractile elements (e.g., titin) may affect active force generation in the heart. The present model confirms the existence of such an intrinsic active force in the left ventricle without articulating about its origin.

Another interesting observation resulting from the forced form of the oscillator is the similarity between the magnitude of $\overline{K}$ and $\overline{h}$ in all the 10 cases ($p>0.05$). Based on the present model, the mean damping coefficient can be considered zero in healthy hearts, denoting that the viscous damping is minimal in normal LV. Further studies are in progress to observe the variations of coefficients in cases where the physical state of the LV has been changed due to acquired or congenital heart diseases.

CHAPTER SIX

Effect of Isovolumic Relaxation Phase on Diastolic Rapid Filling in the Process of Postinfarction Cardiac Remodeling

6.1. Chapter Abstract

Myocardial infarctions, especially large ones, lead to complex variations in cardiac structure over the time, which involves not only the infarcted area but also the intact zones. In the present article, the relation between the time constant of isovolumic pressure-drop (τ) and left ventricular axial strain (ε) has been studied during the course of cardiac remodeling after induction of different types of myocardial infarction (MI) in sheep. Animals were categorized in three different groups for anteroapical, anterobasal, and posterobasal infarctions and were followed up two, five, and eight weeks after infarction. Gradual increase in end-diastolic and end-systolic lengths of the long axis was recorded followed by certain types of myocardial infarction. Our results showed an inverse relation between τ and ε in all three groups. However, in most infarction models, ε did not follow the same trend of change in either end-systolic or end-diastolic LV axial length. The present study also confirms that the post-infarction changes in isovolumic relaxation phase have direct influence on diastolic rapid filling phase, which leads to

complex variations in end-diastolic lengthening, and end-systolic shortening of the LV contractile elements.

6.2. Introduction

Efficient left ventricular (LV) filling during diastole is a vital component of normal cardiac function. Evaluation of diastolic function is crucial with the aim of early detection of dysfunctions after infarction However, the effect of infarction-induced remodeling on LV diastolic function is poorly understood. This is particularly true with regard to the time course and the effect of infarct location. The process of cardiac relaxation occurs mostly during the isovolumic relaxation (IVR) phase of the cardiac cycle. IVR is described as the period between aortic valve closure and mitral valve opening when ventricular pressure drops rapidly. Diastolic performance during IVR is best characterized by the time constant of isovolumic pressure drop (τ)[21], which is the time that pressure has fallen to approximately one-third ($1/e \approx 1/3$) of the end-systolic pressure. The early diastolic filling is the direct result of the LV suction and can be assessed by LV expansion after mitral valve opening.

Myocardial infarctions, especially large ones, in hearts as a homogenous system result in complex variations in cardiac structure over the time, which not only involve the infarct area but also affect the intact zones. This time dependent phenomenon is expressed as the ventricular remodeling process[120]. Remodeling is associated with impaired LV systolic performance[121] but its effect on diastolic function is poorly understood. In this study, the LV longitudinal axis function was considered an important determinant of its global performance due to longitudinally oriented subendocardial myocardial fibers[122,123].

In the present study, we investigated the effect of LV remodeling on diastolic function during both IVR and filling by using three ovine infarction models[124] similar in size, but at different locations. The results confirm that the post-infarction changes in IVR phase have direct influence on diastolic rapid filling expressed as end-diastolic lengthening, and end-systolic shortening of LV contractile elements.

6.3. Methods

6.3.1. Surgical procedure and data acquisition

Twenty sheep between 35 and 45kg were anesthetized and underwent left thoracotomy and ligation of two major coronary arteries[124]. Animals were treated under an experimental protocol approved by the University of Pennsylvania's Institutional Animal Care and Use Committee (IACUC) and in compliance with NIH publication No. 85-23, as revised in 1985. Animals were induced with Thiopental sodium (10 to 15mg/kg intravenously [IV]) and intubated. Anesthesia was maintained with Isofluorane (1.5% to 2%) and oxygen. All animals received Glycopyrrolate (0.4 mg IV) and Enrofloxin (10mg/kg IV) on induction. Under aseptic conditions, animals underwent left thoracotomy, and polypropylene snares were loosely placed around the appropriate coronary arteries. In all the animals, sonomicrometry transducers (*1.0mm; Sonometrics Corp., London, Ontario, Canada*) were implanted at the apex and base of the LV. The surface electrocardiogram (ECG), arterial blood pressure (ABP) and LV pressure (LVP) were continuously monitored and recorded. LVP was measured using a high-fidelity pressure transducer (*Spc-350, Millar Instruments Inc., Houston, TX*) inserted from the femoral artery into the LV.

Fourteen days after initial instrumentation, the sheep were anesthetized again. ECG, ABP and the LVP were continuously monitored and recorded as baseline data. Afterward, the subcutaneous snares were exposed, tightened, and tied to produce a myocardial infarction. Each animal received Magnesium sulfate (1g IV), Amiodarone (150mg IV) and Lidocaine (3mg/kg IV bolus, then 2 mg/min infusion) prior to infarction. ECG, ABP and the LVP were collected again thirty minutes after induction of infarction representing post-infarction data.

6.3.2. Infarction Models[124]

Six sheep had ligation of the distal left anterior descending and second diagonal arteries. This type of infarction involved 22±3 % of the LV mass and led to the development anteroapical MI[125] (Figure 6.1A). An anterobasal infarction involving 24±2 % of the LV mass was created in nine animals followed by ligating the first and second diagonal arteries (Figure 6.1B). Five animals underwent of ligation of the second and third obtuse marginal arteries resulted in a posterobasal MI[126,127] which involved 21±4 % of the LV mass (Figure 6.1C).

Desired data as mentioned earlier were collected during the eight weeks after infarction. Following the eighth week, the animals were euthanized (80 mEq potassium chloride IV bolus); the heart was excised, and inspected for validation of infarct size and location as well as position of sonomicrometry transducers.

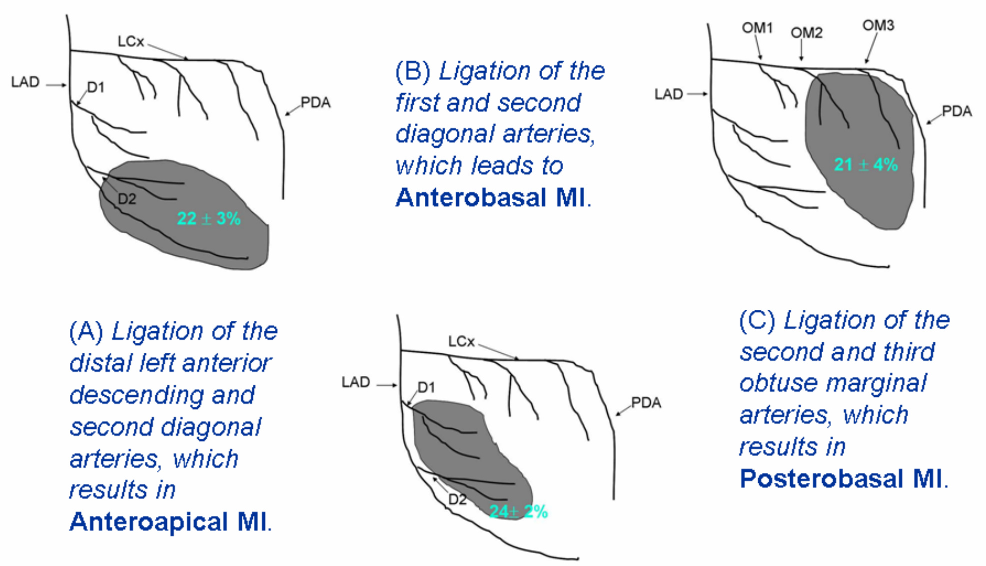

Figure 6.1. Animal infarction models. (A) shows the anteroapical infarction model; (B) shows the anterobasal infarction model; (C) shows the posterobasal infarction model.

6.3.3. Mathematical analysis

A mono-exponential model was used to describe the course of pressure drop during isovolumic relaxation phase:

$$P = P_0 e^{-t/\tau} + P_\infty \quad (6\text{-}1)$$

where P is the LV pressure, P_0 is the pressure at minimal $\frac{dP}{dt}$, τ is the pressure drop time-constant, P_∞ represents the pressure asymptote[21] and t is the time (Figure 6.2). The asymptote will be zero if the LV pressure during IVR does not fall below zero. The IVR phase was identified based on the trend of LVP and $\frac{dP}{dt}$ in each case and the results confirmed by the ECG[46].

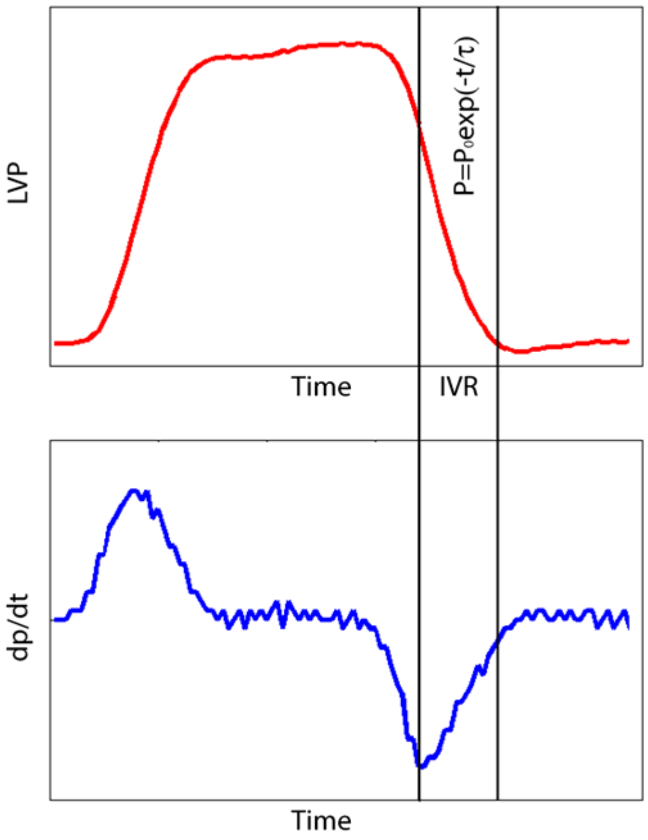

Figure 6.2. Left ventricular pressure and dp/dt plots. Red curve shows the measured LVP for a healthy sheep. Blue curve shows the dp/dt computed from the LVP. Isovolumic relaxation (IVR) phase is defined based on LVP and dp/dt curves. IVR was regressed to a decaying exponential function as showed in the Figure.

The length of ventricular long-axis segments through the cardiac cycles were measured using sonomicrometry transducers. Long axis segmental Eulerian strain (ε) was computed as:

$$\varepsilon = \frac{EDL - ESL}{EDL} \qquad (6\text{-}2)$$

where EDL is the length of end-diastolic long-axis segment and ESL is the length of end-systolic long-axis segment.

6.4. Results

6.4.1. Left ventricular pressure.

The LV pressure drop time-constant (τ) and pressure asymptote (P_∞) were computed based on regression of the measured pressure during IVR to an exponential pressure drop function (6-1). Pressure drop time-constant (τ) was computed for each sheep at baseline, post infarction, two, five and eight weeks after induction of infarct (Table 6.1). For comparison purposes, each time-constant (τ) was normalized by the primary time-constant obtained at the baseline (τ_0) for each sheep. The averaged curve as the representative of each group is depicted in Figure 6.3. Results for each group show similarities in the overall trend of change in time-constant (tau):

The normalized tau curve for the anteroapical infarct group showed a 21.00 ± 2.00% increase instantly after infarction. Two weeks after infarction, it declined 7.00 ± 2.50% lower than the baseline and remained at this level until the fifth week. By the eighth week, measured tau was 14.00 ± 4.00% greater than the baseline (Figure 6.3 and Table 6.1).

Results for the anterobasal MI groups showed 26.00 ± 4.00% increase in tau, immediately after infarction. After two weeks, tau dropped 5.00 ± 3.00% below the baseline and remained at this level until the fifth week. After 8 weeks, tau increased 29.00 ± 8.00% above its baseline (Figure 6.3 and Table 6.1).

The trend of change in tau for the posterobasal MI group showed 58.00 ± 10.00 % immediate elevations after infarction (Figure 6.3); then it fell to 42.00 ± 3.00% below the baseline at the second week. Within the fifth and the eighth weeks, tau grew. However, it was still 12.00 ± 1.00% lower than the baseline level at the eighth week (Figure 6.3).

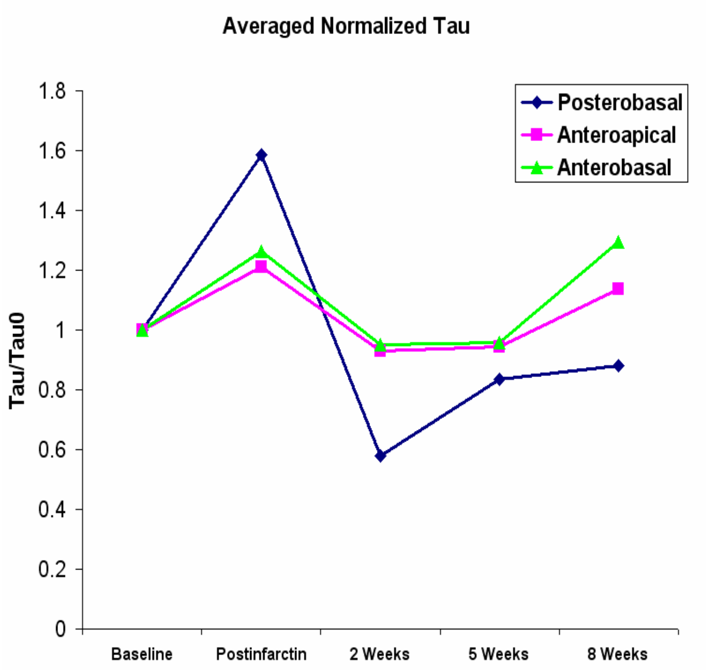

Figure 6.3. Averaged normalized τ following distinct infarctions. As a common characteristic for all the examined groups, τ shows an immediate elevation after infarction and a late rise after five weeks. This is a representative of deterioration of suction in early filling phase, immediately after infarction and later during the remodeling process. The extent of the rise in each group was different. Anteroapical MI group shows the minimum post infarction rise (11%). Anterobasal MI group showed 31% post-infarction rise. The maximum post-infarction rise was observed in posterobasal MI group (66%).

6.4.2. Measurement of long-axis segment

End-systolic (ESL) and end-diastolic (EDL) long-axis segments were measured as the distance between the base and the apex of the heart at end-systole and end-diastole, respectively.

For the anteroapical MI group, the average ESL and EDL at baseline were 68.42 ± 4.76 mm and 71.92 ± 4.30 mm, respectively. Eight weeks after infarction, these values increased to 77.85 ± 4.43 mm and 80.41 ± 5.24 mm, respectively. For the anterobasal MI group, the average ESL and EDL at the baseline were 61.09 ± 8.02 mm and 64.60 ± 7.98 mm, respectively. Eight weeks after infarction, ESL and EDL increased to 68.04 ± 6.51 mm and 71.30 ± 7.71 mm, respectively. For the posterobasal MI group, the average ESL and EDL at the baseline were 67.11 ± 5.26 mm and 69.55 ± 6.21 mm and increased to 72.47 ± 4.83 mm and 76.26 ± 7.00 mm, respectively, eight weeks after infarction. The averaged normalized curves of EDL and ESL for each case during remodeling process have been depicted in Figure 6.4.

Tau (ms)	Anteroapical	Anterobasal	Posterobasal
Baseline	22.652 ± 5.430	28.461 ± 11.603	26.278 ± 4.173
30 minutes after MI	28.125 ± 10.689	33.908 ± 10.131	43.240 ± 3.006
2 Weeks after MI	19.957 ± 1.923	24.511 ± 4.416	16.527 ± 8.773
5 Weeks after MI	20.965 ± 5.935	26.136 ± 9.615	21.566 ± 1.692
8 Weeks after MI	24.107 ± 3.387	31.978 ± 12.563	22.884 ± 2.681

Table 6.1. Averaged pressure drop constant after different models of MI. Note: Values are means plus/minus standard deviations. All values are in millisecond

Long Axis Strain	Anteroapical	Anterobasal	Posterobasal
Baseline	0.049 ± 0.026	0.055 ± 0.011	0.034 ± 0.010
30 minutes after MI	0.034 ± 0.017	0.050 ± 0.015	0.030 ± 0.005
2 Weeks after MI	0.041 ± 0.018	0.051 ± 0.022	0.041 ± 0.016
5 Weeks after MI	0.039 ± 0.031	0.050 ± 0.015	0.040 ± 0.020
8 Weeks after MI	0.031 ± 0.016	0.045 ± 0.013	0.048 ± 0.024

Table 6.2. LV Long Axis Eulerian Strain following MI. Note: Values are means plus/minus standard deviations.

Long axis Eulerian strain was calculated based on the definition that has been described in the method section (6-2). Results showed a drop in Eulerian strains followed by the induced infarction in all the cases. The trend of the variations during the remodeling process is depicted in Figure 5 and also shown in Table 6.2.

6.5. Discussion

The interrelated changes in trend of pressure drop during IVR phase and LV long-axis strain during remodeling process suggest that variation in diastolic function can directly influence the systolic performance of the left ventricle. Location of the infarct, regardless of its size induces a variety of changes in IVR dynamics during remodeling process which accordingly results in a range of variation in LV long-axis strain. However, certain phenomena seem to take place in spite of infarct location.

6.5.1. Variation of diastolic function

Previous studies have shown the effects of myocardial ischemia on global hemodynamics of the heart[128]. Marsch et al[27] showed that the time-constant of IVR (tau) temporarily increases during ischemia but recovers completely one hour after reperfusion. The results of the present study show an immediate rise in tau, 30 minutes after infarction as a common characteristic for all the examined groups (Figure 6.2). This phenomenon demonstrates that the dysfunction in IVR is the immediate response of the heart to infarction and it occur regardless of location of infarct. However, reduction of time-constant during the first two weeks after all three types of infarction in this study can be described as a compensatory mechanism to retrieve the diastolic function. A possible hypothesis that can explain this phenomenon is the inverse relation between the intraventricular pressure gradient and the tau[129]. In a post infraction condition, heart struggles to improve the diastolic function by increasing the intraventricular pressure gradient faster than normal.

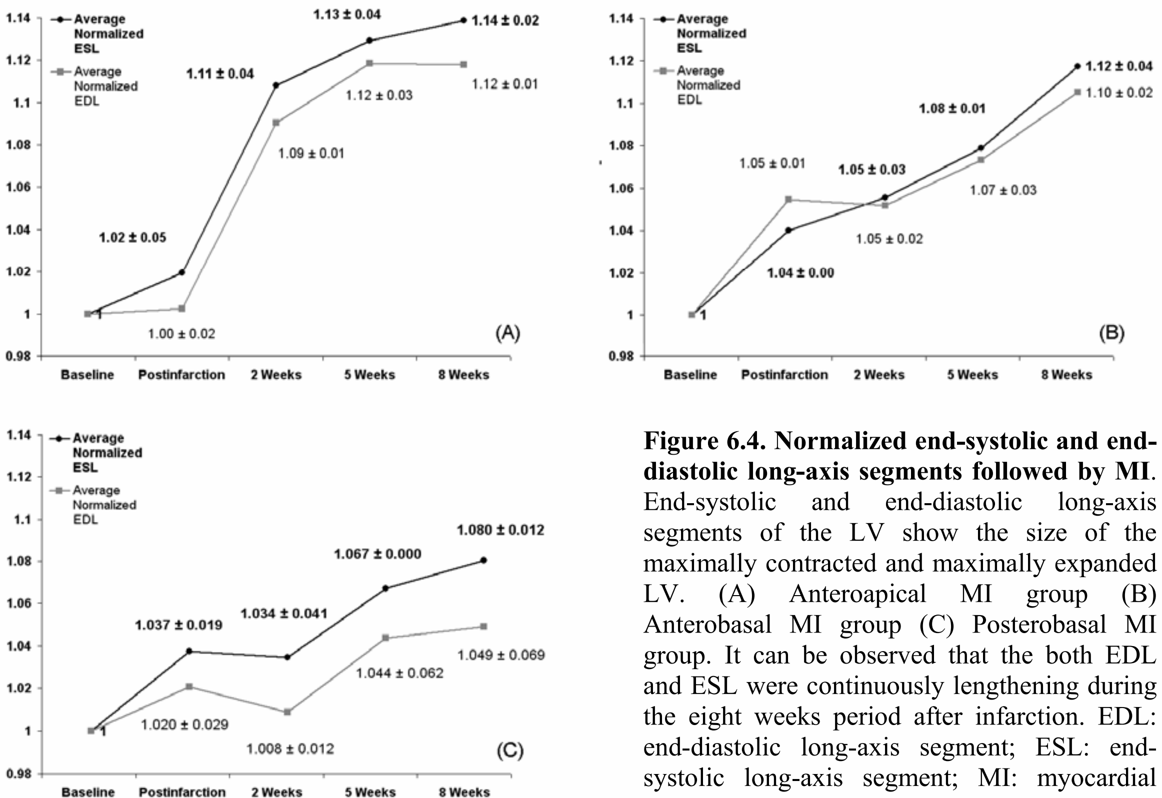

Figure 6.4. Normalized end-systolic and end-diastolic long-axis segments followed by MI. End-systolic and end-diastolic long-axis segments of the LV show the size of the maximally contracted and maximally expanded LV. (A) Anteroapical MI group (B) Anterobasal MI group (C) Posterobasal MI group. It can be observed that the both EDL and ESL were continuously lengthening during the eight weeks period after infarction. EDL: end-diastolic long-axis segment; ESL: end-systolic long-axis segment; MI: myocardial infarction.

In each infarction group, results showed that after the second week, tau gradually increased and by the week eighth, it reached to a level very close to its baseline (in posterobasal) or beyond the baseline level (anteroapical and anterobasal). At this stage, the compensatory mechanisms have failed to maintain the diastolic function and diastolic failure occurred. As a matter of fact, it can be concluded that the remodeling is initially an adaptive response to maintain normal cardiac function. However, it gradually becomes maladaptive and leads to progressive decompensation.

6.5.2. Variation in ventricular expansion

Contraction of the ventricle in the longitudinal axis is mainly caused by subendocardial fibers which are sensitive to ischemia[130]. End-systolic and end-diastolic long-axis segments of LV represent the size of the maximally contracted and maximally expanded LV, respectively. It has been previously shown that the length of the unstressed myocardial segments increases when they are subjected to ischemia[128,131]. However, the process of ventricular enlargement after infarction is more complex and is also influenced by several other factors such as infarct size[132], infarct healing[133], and ventricular wall stresses[120]. Deformation of ventricular geometry has been reported as the final stage of infarct expansion which is a consequence of lengthening in non-contractile region[134].

Infarction initiates a process resulting in plastic deformation of the ventricle. Continuous increase in the length of the myocardial elements is referred as creep, which is an engineering term defined as time-dependant change in length, at a constant stress from external forces[135].

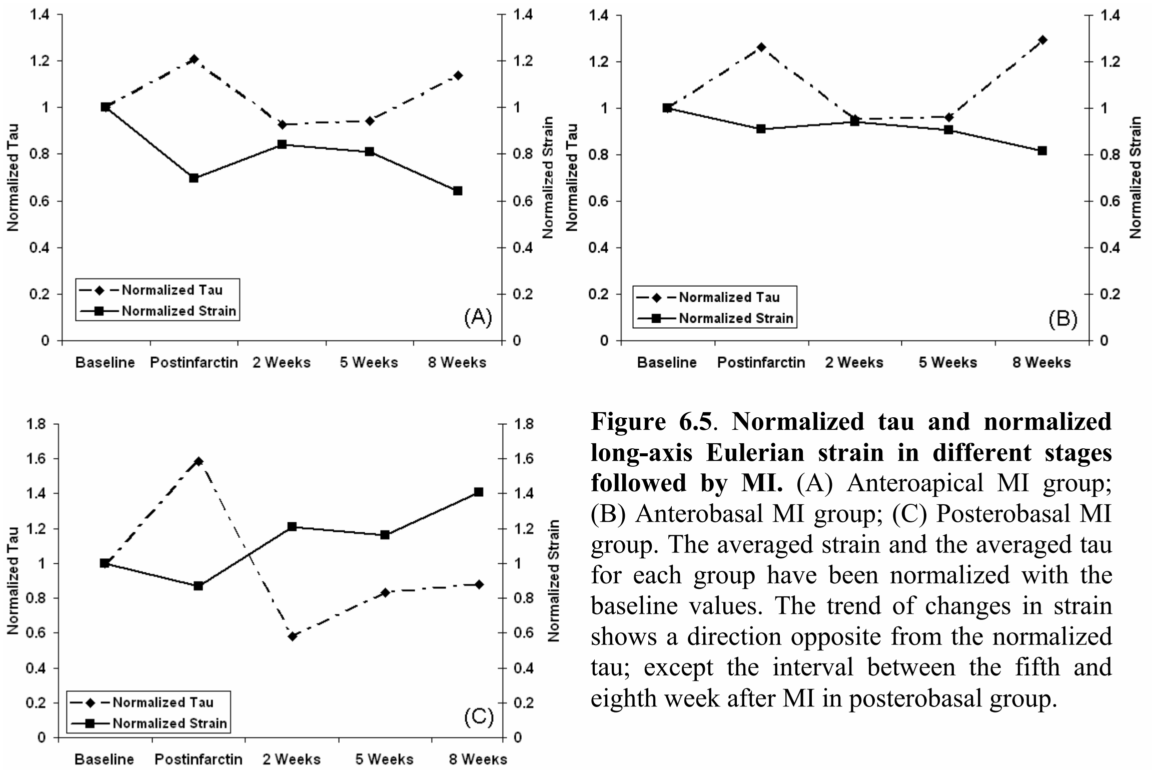

Figure 6.5. **Normalized tau and normalized long-axis Eulerian strain in different stages followed by MI.** (A) Anteroapical MI group; (B) Anterobasal MI group; (C) Posterobasal MI group. The averaged strain and the averaged tau for each group have been normalized with the baseline values. The trend of changes in strain shows a direction opposite from the normalized tau; except the interval between the fifth and eighth week after MI in posterobasal group.

Our results confirm the gradual increase in EDL and ESL within the studied myocardial infarction groups. However, the trend of lengthening was not quite similar in all the groups studied (Figure 6.3A). In anteroapical MI group, the lengthening was stabilized at the fifth week to a level around 13% greater than the baseline (Figure 6.3B). In anterobasal MI group, the lengthening process steadily continued until the eighth week (Figure 6.3C). However, the extent of lengthening in anterobasal group was less than in anteroapical group at any time points after MI. The trend of long-axis elongation in posterobasal MI group was quite different with the other two groups. The long-axis segment enlarged after infarction but unlike the other groups, it shrank after two weeks and then rose again until the eighth week.

6.5.3. Correlation between IVR time-constant and ventricular contraction

The correlation between IVR time-constant (tau) and the ventricular contractility is a topic that has been less thoroughly studied in the process of remodeling after infarction.

In the present study, we considered long-axis Eulerian strain (ε) as an index of LV contraction.

In anteroapical MI group, epsilon (ε) dropped to 69% of its baseline level after infarction, while tau (τ) elevated 120% with respect to its baseline valve. Two weeks after infarction, epsilon elevated to 84% of its baseline value whereas tau dropped 7% below the baseline. Five weeks after infarction, epsilon slightly dropped to 81% of its original value while tau slightly increased to 94% to the baseline magnitude. Eight weeks after infarction, epsilon dropped again to 64% of the baseline value as tau elevated 14% above its original valve (Figure 6.5A).

In anterobasal MI group, epsilon dropped to 91% of its baseline level after infarction, while tau (τ) elevated 126% with respect to its baseline valve. Two weeks after infarction, epsilon slightly elevated to 94% of its baseline value whereas tau dropped 5% below the baseline. Five weeks after infarction, epsilon slightly dropped to 90% of its original value while tau slightly increased to 96% to the baseline magnitude. Eight weeks after infarction, epsilon dropped again to 81% of the baseline value as tau elevated 29% above its original valve (Figure 6.5B).

In posterobasal MI group, epsilon dropped to 86% of its baseline level after infarction, while tau (τ) elevated 158% with respect to its baseline valve. Two weeks after infarction, epsilon elevated to 21% above the baseline value whereas tau dropped to 58% of the baseline. Five weeks after infarction, epsilon slightly dropped to 16% above its original value while tau increased to 83% to the baseline magnitude. Eight weeks after infarction, epsilon increased to 41% above the baseline value as tau slightly elevated to 88% of its original valve (Figure 6.5C).

Results showed that ε in most cases did not follow the trend of change in neither EDL nor ESL; except the interval between the fifth and eighth week after MI in posterobasal group (Figure 6.5C). However, there was an inverse relationship between tau (τ) and epsilon (ε) in all the studied groups (Figure 6.5).

6.6. Conclusion

The present study has confirmed the strong inverse relationship between tau and epsilon. On the other hand, it was observed that the trend of change in epsilon (ε) is independent of length both EDL and ESL. Therefore, it can be postulated that ventricular longitudinal shortening as an index for contraction, is not a direct consequence of myocardial segment lengthening as previously thought[136,137].

The presence of an infarct zone deteriorates the homogeneity of the LV chamber. This geometrical change alters the untwisting motion in IVR phase and eventually affects the LV suction in early filling phase of diastole. The isovolumic movements, rather than being a simple coiling and recoiling phenomenon, constitute components of a specific and complex ventricular reshaping process, most probably creating the optimal conditions for the diastolic filling and systolic ejection[138].

6.7. Study limitations

The relatively small number of cases and the variety in the weight and the age of the sheep resulted in moderately wide standard deviations for the computed parameters.

APPENDIX

A.1. Cardiac physiology

The heart is a hollow muscular organ of a somewhat conical form; it lies between the lungs in the middle mediastinum and is enclosed in the pericardium. The heart, in the adult, measures about 12cm in length, 8 to 9cm in breadth at the broadest part, and 6cm in thickness. Its weight, in the male, varies from 280 to 340grams; in the female, from 230 to 280grams. The heart continues to increase in weight and size up to an advanced period of life; this increase is more marked in men than in women. The heart is subdivided by septa into right and left halves, and a constriction subdivides each half of the organ into two cavities, the upper cavity being called the atrium, the lower the ventricle. The heart, therefore, consists of four chambers, right and left atria, and right and left ventricles. The base (*basis cordis*) which is directed upward, backward, and to the right, is formed mainly by the left atrium, and, to a small extent, by the back part of the right atrium. The apex (*apex cordis*) is placed downward, forward, and to the left, and is overlapped by the left lung and pleura. The left atrioventricular opening (*mitral orifice*) is surrounded by a dense fibrous ring and covered by the lining membrane of the heart and is guarded by the bicuspid or mitral valve; it measures about 1 inch in diameter. The bicuspid or mitral valve is attached to the circumference of the left atrioventricular orifice. It consists of two triangular cusps, formed by duplication of the lining membrane, strengthened by fibrous tissue, and containing a few muscular fibers. The cusps are of unequal size, and are larger, thicker, and stronger than those of the tricuspid valve are. The larger cusp is placed in front and to the right between the atrioventricular and aortic orifices, and is known as the anterior or aortic cusp; the smaller or posterior cusp is placed behind and to the left of the opening. The cusps of the bicuspid valve are furnished with a number of delicate tendinous cords known as chorda tendinae. The papillary muscles are two in number, one being connected to the anterior, the other to the posterior wall of the ventricle; they are of large size, and end in rounded extremities from which the chorda tendinae arise. The chorda tendinae from each papillary muscle are connected to both cusps of the bicuspid valve[44] (Figures A.1-A.4).

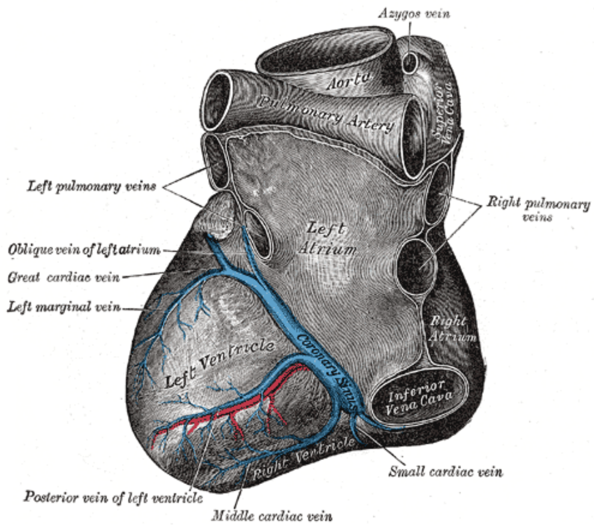

Figure A.1. Base and diaphragmatic surface of heart. The position of left atrium and left ventricle could be observed. [Henry Gray (1825–1861). *Anatomy of the Human Body*].

The oxygenated blood from lungs returns to left atrium, then left ventricle, and finally pumps through the aorta from left ventricle. Cardiac cycle has two major functional phases; diastole, which is the phase that ventricles are filled with blood and systole which blood pumps out of the heart. Each cycle takes around 800 milliseconds which 60% of it is during diastole and the rest is during systole. Each phase divides to several stages.

Diastole is divided to isovolumic relaxation and ventricular filling which is subdivided to rapid inflow, diastasis and atrial contraction. Systole includes isovolumic contraction and ventricular ejection (Figure A.5).

Figure A.2. Interior of left side of heart. The base of the heart, papillary muscles inside the left ventricle and the inlet of the left atrium has shown [Henry Gray (1825–1861). *Anatomy of the Human Body*].

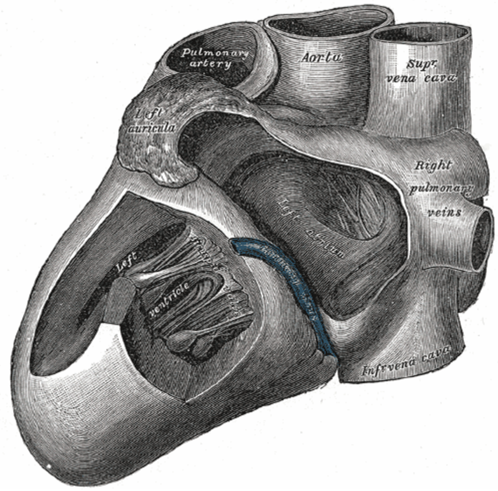

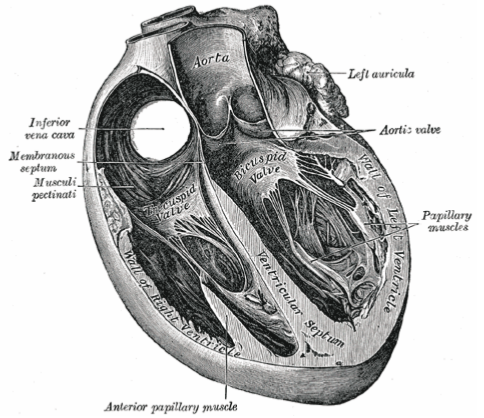

Figure A.3. Coronal section of the heart; showing the ventricular septum; position of mitral valve corresponding to papillary muscles could be observed too [Henry Gray (1825–1861). *Anatomy of the Human Body*].

A.2. Echocardiography

Cardiac ultrasonography (echocardiography) is a valuable non-invasive tool for imaging the heart and surrounding structures. In general, echocardiography is used to evaluate cardiac chamber size, wall thickness, wall motion, valve configuration and motion, and the proximal great vessels. Using ultrasound, anatomic relationships can be determined and some information regarding cardiac function can be derived.

Diagnostic ultrasound employs pulsed, high frequency (>20,000 Hz) sound waves that are reflected back from body tissues and processed by the ultrasound machine to create characteristic images. Sound waves are propagated to the surrounding medium at a characteristic speed (approximately 1540 m/sec in soft tissues), the thickness, size and location of various soft tissue structures in relation to the origin of the ultrasound beam can be calculated at any point in time. The intensity of the ultrasound beam decreases as it travels away from the transducer because of beam divergence, absorption, scatter, and reflection of wave energy at tissue interfaces; these factors influence the intensity of the returning echoes. Three types of echocardiography are used clinically: M-mode, two-dimensional (2-D B-mode or real time), and Doppler. Each has important applications, which are briefly described below:

The M-mode echocardiogram provides a one-dimensional view (depth) into the heart. The M-mode images represent echoes from various tissue interfaces along the axis of the beam (Figure A.4).

Two-dimensional echocardiography allows a plane of tissue (both depth and width) to be imaged. Thus, the orientation and anatomic relationships between various structures are easier to appreciate that with M-mode images. A variety of planes through the heart can be imaged from several locations on the chest wall (Figure A.5).

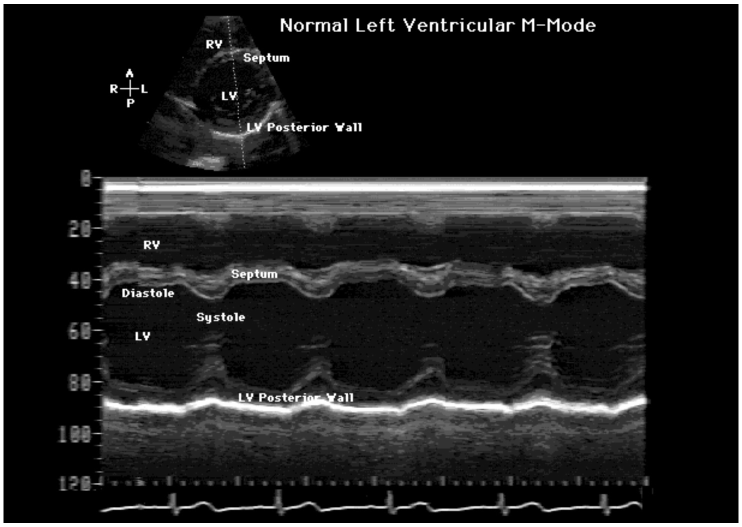

Figure A.4. M-Mode Echo of a Normal left ventricle. Septum is the wall separating LV and RV. LV: Left ventricle and LA: Left atrium. The structures during systolic and diastolic phase are depicted (Courtesy of the University of Kansas Medical Center).

Doppler imaging allows evaluation of blood flow patterns, direction, and velocity; thus, it permits documentation and quantification of valvular insufficiency or stenosis and cardiac shunts. Estimations of blood flow and cardiac output can also be made. Doppler echocardiography is based on detection of frequency changes (the Doppler shift) occurring as ultrasound waves reflect off individual blood cells moving either away from or toward the transducer. Calculation of blood flow velocity is possible when the flow is parallel to the angle of the ultrasound beam.

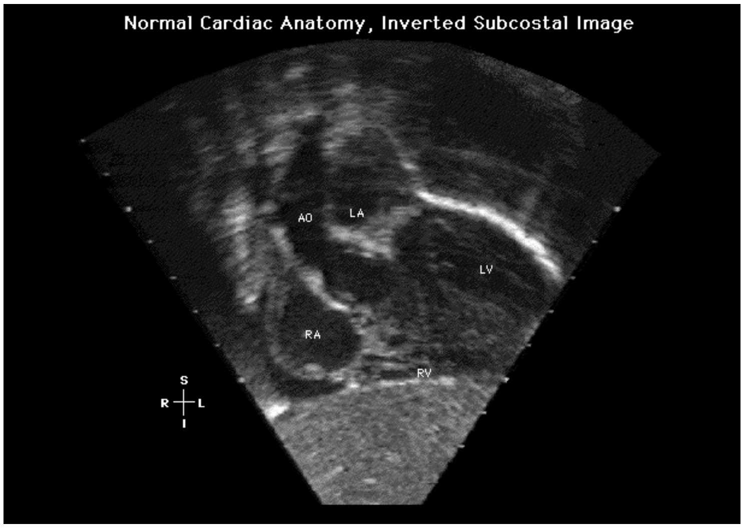

Figure A.5. Normal cardiac anatomy shown by 2-D-Echo. AO: Aortic arch; RA: Right atrium: LV: Left ventricle and LA: Left atrium (Courtesy of the University of Kansas Medical Center).

The parameters that can be obtained from Doppler imaging and are useful in evaluating the diastolic function are: E-wave, which is the early trans-mitral flow velocity during rapid filling phase; A-wave, which is the trans-mitral velocity during atrial contraction in late diastole; the ratio between the early peak trans-mitral flow velocity (E) and the late peak atrial systolic velocity (A) (E/A ratio), which is expressed in terms of the peak velocities; deceleration time (DT), which is calculated and expressed as the time for the peak filling velocity (E-wave) to fall to baseline; and isovolumic relaxation time (IVRT), which is the time from aortic valve closure to the onset of mitral valve inflow (Figure A.6).

The Doppler principle can also be used to measure the velocity of movement of tissue in the direction of the ultrasound beam (Tissue Doppler Imaging). Because the velocities are generally much lower than that of blood, the frequency shift is correspondingly lower and more difficult to measure. Modern ultrasound machines, however, frequently offer 'tissue Doppler' as an option and it is being used with increasing frequency in echocardiography.

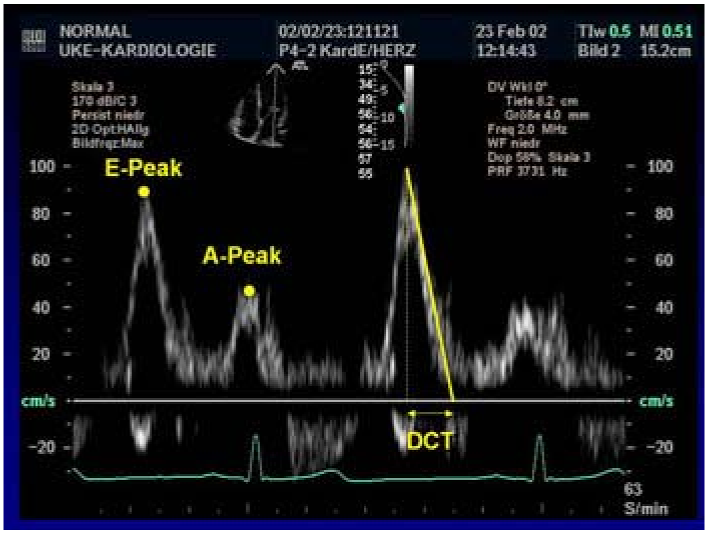

Figure A.6. Normal echo Doppler components. E-wave, which is the early maximal trans-mitral flow velocity; A-wave, which is the peak velocity during atrial contraction in late diastole and deceleration time (DT), which is calculated and expressed as the time from the peak filling velocity (E-wave) to fall to baseline have been shown in this Figure (Courtesy of University Medical Center Hamburg-Eppendorf).

A.3. Patient selection criteria for evaluation of formation number

To test whether the Formation Number could characterize the flow process in the left ventricle, the goal is to conduct a series of *in vivo* tests on approximately 100 consented subjects within the following specific groups.

A.3.1. Patient selection inclusion criteria

1) At least 50 healthy volunteers (preferably, 25-M & 25-F) of the following characteristics:

    a) Age: ≥ 20,
    b) Normal rhythm,
    c) Normal heart valves,
    d) Normal blood pressure,
    e) Normal EKG,
    f) No history of any kind of myocardial infarction,
    g) Left ventricular ejection fraction ≥ 50%,
    h) Non-smoker,
    i) Appropriate weight for the height.

2) At least 20 patients with dilated cardiomyopathy with the following criteria:

    a) Left ventricular end diastolic dimension ≥ 60mm,
    b) Left ventricular fractional shortening ≤ 25%,
    c) No segments of cardiac hypertrophy (left ventricular wall thickness ≤ 12mm).

3) At least 20 hypertensive patients in the age group of 30-60 with the following criteria:

    a) Diagnosed as essential hypertension with diastolic blood pressure ≥ 95 mmHg,
    b) No prior history of myocardial infarction.

4) Any patients diagnosed with hypertrophic or restrictive cardiomyopathy.

5) At least 10 patients with different stages of mitral stenosis (higher formation numbers).

A.3.2. Protocol for Echocardiography

1) Use a 3.5 MHz or 5.0 MHz phased-array transducer
2) Use Pulsed-Wave (*PW*) Doppler
3) Optimize depth and repetition rate
4) Obtain 4-chamber gray-scale view or left 2-chamber view (LV & LA) of at least 15 cycles
5) Measure diameter/area of mitral annulus (as a function of time, preferably)
6) Measure the distance from mitral annulus to the cardiac apex, *L*
7) Obtain Color Doppler Flow Mapping (CDFM) of the trans-mitral flow of at least 15 cycles
8) Obtain *E*-wave and *A*-wave
9) Measure *DT*, *IVRT* and *E/A* ratio
10) Measure color-coded diameter of mitral annulus, $D_{(Color)}$
11) Obtain mean trans-mitral velocity, $V_{(Mean)}$
12) Develop cut-off criteria for tracing *E*-wave
13) Obtain velocity-time integral (*VTI*) from *PW* Doppler
14) Obtain tissue Doppler indices (E’, A’, etc.)
15) Obtain ejection fraction (EF), *LVEDV* and *LVESV*

A.4. Engineering drawing of the load cell

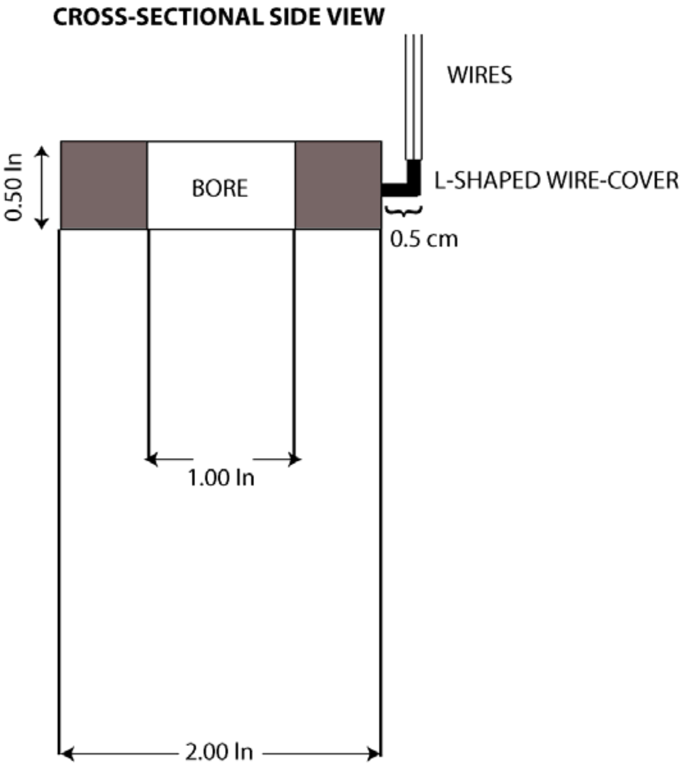

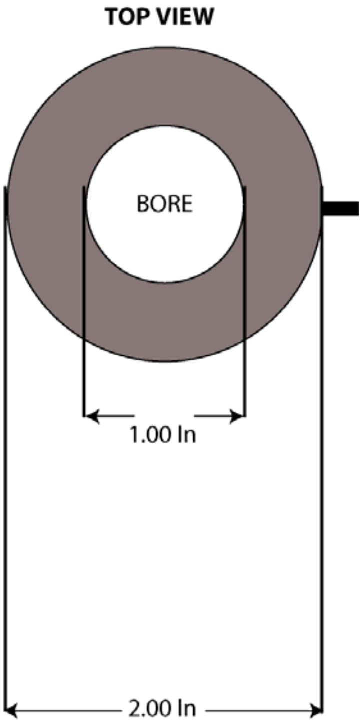

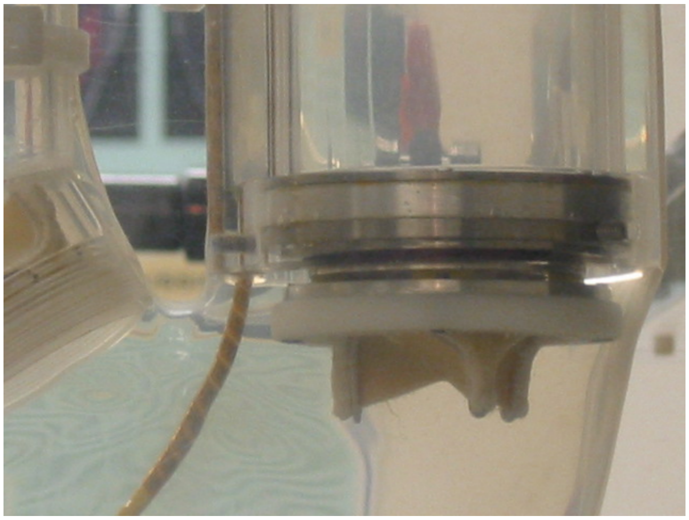

References:

---

[1] Ho KK, Pinsky JL, Kannel WB, Levy D. The epidemiology of heart failure: the Framingham Study. J Am Coll Cardiol 1993;22(4 suppl A):6A-13A

[2] Yusuf S, Thom T, Abbott RD. Changes in hypertension treatment and in congestive heart failure mortality in the United States. *Hypertension*. 1989;13(suppl 5):I-74–I-79.

[3] Massie BM, Shah NB. Evolving trends in the epidemiologic factors of heart failure: rationale for preventive strategies and comprehensive disease management. *Am Heart J* 1997;133:703-12

[4] McMurray JJ, Stewart S. Epidemiology, aetiology, and prognosis of heart failure. *Heart* 2000;83:596-602

[5] Vasan RS, Larson MG, Benjamin EJ, Evans JC, Reiss CK, Levy D. Congestive heart failure in subjects with normal versus reduced left ventricular ejection fraction: prevalence and mortality in a population-based cohort. *J Am Coll Cardiol* 1999;33:1948-55.

[6] de Simone G, Greco R, Mureddu G, Romano C, Guida R, Celentano A, Contaldo F. Relation of Left Ventricular Diastolic Properties to Systolic Function in Arterial Hypertension. *Circulation*. 2000;101:152

[7] Zile MR, Brutsaert DL. New Concepts in Diastolic Dysfunction and Diastolic Heart Failure: Part I Diagnosis, Prognosis, and Measurements of Diastolic Function. *Circulation.* 2002;105:1387-1393

[8] Ohno M, Cheng CP, Little WC. Mechanism of altered patterns of left ventricular filling during the development of congestive heart failure. Circulation 1994;89:2241-50.

[9] Grodecki PV, Klein AL. Pitfalls in the echo-Doppler assessment of diastolic dysfunction. *Echocardiography*. 1993 Mar;10(2):213-34.

[10] Bellhouse, B.J. Fluid mechanics of a model mitral valve and left ventricle. *Cardiovascular Research*, 1972; 6, 199–210.

[11] Reul, H., Talukder, N., Muller, W., 1981. Fluid mechanics of the natural mitral valve. *Journal of Biomechanics* 14, 361–372.

[12] Kim, W.Y., Bisgaard, T., Nielsen, S.L., Poulsen, J.K., Pedersen, E.M., Hasenkam, J.M., Yoganathan, A.P., 1994. Two-dimensional mitral flow velocity profiles in pig models using epicardial echo Doppler Cardiography. *J Am Coll Cardiol* 24, 532–545.

[13] Kim, W.Y., Walker, P.G., Pedersen, E.M., Poulsen, J.K., Oyre, S., Houlind, K., Yoganathan, A.P., 1995. Left ventricular blood flow patterns in normal subjects: a quantitative analysis by three dimensional magnetic resonance velocity mapping. *J Am Coll Cardiol* 26, 224–238.

[14] Kilner, P.J., Yang, G.Z., Wilkes, A.J., Mohiaddin, R.H., Firmin, D.N., Yacoub, M.H., 2000. Asymmetric redirection of flow through the heart. *Nature* 404, 759–761.

[15] Shariff K, Leonard A. Vortex rings. *Annu Rev Fluid Mech* 24: U235-U279 1992

[16] Gharib M, Rambod E, Shariff K. A universal time scale for vortex ring formation. *J. Fluid Mech*: 121-140 APR 10 1998

[17] Krueger PS, Gharib M. The significance of vortex ring formation to the impulse and thrust of a starting jet. *Physics of fluids* 15 (5): 1271-1281 MAY 2003

[18] Dabiri JO, Gharib M. Fluid entrainment by isolated vortex rings. *J. Fluid Mech*. 2004 (511): 311-331

---

[19] Dabiri JO, Gharib M. Starting flow through nozzles with temporally variable exit diameter, *J. Fluid Mech* 538: 111-136.

[20] Abel FL. Maximal negative dP/dt as an indicator of end systole. *Am J Physiol Heart Circ Physiol* 240:H676-H679, 1981

[21] Weiss JL, Fredrisen JW, Weisfeldt ML. Hemodynamic determinants of the time course of fall in canine left ventricular pressure. *J Clin Invest.* 1976;58:751-760

[22] Yellin EL, Hori M, Yoran C, Sonnenblick EH, et al. Left ventricular relaxation in the filling and nonfilling intact canine heart. *Am J Physiol(Heart Circ Physiol)* 250:H620-629, 1986

[23] Hori M, Yellin EH, Sonnenblick EH. Left ventricular diastolic suction as a mechanism of ventricular filling. *Jpn. Circ.J*. 46:124-129, 1982

[24] Hees PS, Fleg JL, Dong SJ, Shapiro EP. MRI and Echocardiographic assessment of the diastolic dysfunction of normal aging: altered LV pressure decline or load? *Am J Physiol(Heart Circ Physiol)* 286:H782-788, 2004

[25] Ommen SR, Nishimura RA, Appleton CP, Miller FA, et al. Clinical utility of Doppler echocardiography and tissue Doppler imaging in the estimation of left ventricular filling pressures; a comparative simultaneous Doppler-catheterization study. *Circulation* 2000:102:1788-1794.

[26] Tokushima T, Reid CL, Gardin JM. Left ventricular diastolic function in the elderly. *AJGC*. 2001;10:20-29.

[27] Marsch SC, Dalmas S, Philbin DM, et al. Post-ischemic diastolic dysfunction. *J Cardiothorac Vasc Anesth.* 1994 Dec;8(6):611-7.

[28] Kheradvar A, Gorman RC, Gorman III, JH, Zeeshan, A, Gharib, M Evaluation of Isovolumic Relaxation Phase in the process of Ventricular Remodeling following Myocardial Infarction. Engineering in Medicine and Biology Society (EMBC), 2004. Conference Proceedings. 26th Annual International Conference of the ,Vol 2 (2004):3654 – 3657

[29] Fuster V, Alexander RW, O'Rourke RA, Roberts R, et al. Hurst's The Heart, 11th Edition. The McGraw-Hill companies, Inc. 2004.

[30] Gharib M, Rambod E, Kheradvar A, Sahn D, Dabiri JO. A global index for heart failure based on optimal vortex formation in the left ventricle. *Proc Natl Acad Sci U S A.* 2006 Apr 18;103(16):6305-8.

[31] Rademakers FE, Buchalter MB, Rogers WJ, Zerhouni EA, et al. Dissociation between left ventricular untwisting and filling. Accentuation by catecholamines. *Circulation.* 1992 Apr;85(4):1572-81.

[32] Sonnenblick EH. The structural basis and importance of restoring forces and elastic recoil for the filling of the heart. *Eur Heart J*. 1980; Suppl A: 107-10.

[33] Yellin EL, Meisner JS. Physiology of diastolic function and transmitral pressure-flow relations. *Cardiol Clin*. 2000 Aug;18(3):411-33, vii.

[34] Hasegawa H, Little WC, Ohno M, Brucks S, Morimoto A, Cheng HJ, Cheng CP Diastolic mitral annular velocity during the development of heart failure. *J Am Coll Cardiol* 2003;41:1590 –7

---

[35] Didden N, On the formation of vortex rings: Rolling-up and production of circulation. Z. *Angew. Math. Phys*. 30, 101 1979.

[36] Rosenfeld M, Rambod E, Gharib M. Circulation and formation number of laminar vortex rings *J. Fluid Mech*: 376: 297-318 DEC 10 1998

[37] Vierendeels J, Dick, EA and Verdonck PR. Hydrodynamics of color M-mode Doppler flow wave propagation velocity V(p): A computer study, *J. Am. Soc. Echocardiogr*. 15:219–224, 2002.

[38] Johari H, Rixon GS. Effects of pulsing on a vortex generator jet. *AIAA J* 41 (12): 2309-2315 2003

[39] Cater JE, Soria J The evolution of round zero-net-mass-flux jets. *J Fluid Mech* 472: 167-200 2002

[40] Steen T, Steen S. Filling of a model left ventricle studied by colour M mode Doppler. *Cardiovasc Res.* 1994 Dec;28(12):1821-7.

[41] Baccani B, Domenichini F, Pedrizzetti G, Tonti G. Fluid dynamics of the left ventricular filling in dilated cardiomyopathy. *J Biomech*. 2002 May;35(5):665-71.

[42] Yellin EL, Nikolic S, Frater RWM. Left-ventricular filling dynamics and diastolic function Progress in cardiovascular diseases 1990; 32 (4): 247-271.

[43] Rodriguez F, Langer F, Harrington KB, Tibayan FA, Zasio MK, Cheng A, Liang D, Daughters GT, Covell JW, Criscione JC, Ingels NB, Miller DC. Importance of mitral valve second-order chordae for left ventricular geometry, wall thickening mechanics, and global systolic function. *Circulation*. 2004 Sep 14;110(11 Suppl 1):II115-22.

[44] Standring S. Gray's Anatomy: The Anatomical Basis of Clinical Practice. Churchill Livingstone; 39th edition (November 24, 2004)

[45] Dong SJ, Hees PS, Siu CO, Weiss JL and Shapiro EP. MRI assessment of LV relaxation by untwisting rate: a new isovolumic phase measure of t. *Am J Physiol Heart Circ Physiol* 281: H2002–H2009, 2001.

[46] Guyton AC, Hall JE. Textbook of medical physiology. 10th edition, *WB Saunders Company*, 2000

[47] Brutsaert DL, Rademakera FE, Sys SU. Triple control of relaxation: implications in cardiac disease. *Circulation* 1984; 69: 190-196.

[48] Brutsaert DL, Sys SU. Relaxation and diastole of the heart. *Physiol Rev* 1989; 69: 1228-1315.

[49] Gilbert JC, Glantz SA. Determinants of left ventricular filling and ofthe diastolic pressure/volume-relationship. *Circ Res* 1989; 64: 827-852.

[50] Willert CE, Gharib M. Digital Particle Image Velocimetry *Exp Fluids* 10 (4): 181-193 1991

[51] Kheradvar A, Kasalko J, Johnson D, Gharib M. An in vitro study of changing profile heights in mitral bioprostheses and their influence on flow. *ASAIO J* 2006 Jan-Feb;52(1):34-8.

[52] Appleton CP. Doppler assessment of left ventricular diastolic function: the refinements continue. *J Am Coll Cardiol* 1993;21:1697–700.

[53] Nishimura RA, Tajik AJ. Evaluation of diastolic filling of left ventricle in health and disease: Doppler echocardiography is the clinician's Rosetta stone. *J Am Coll Cardiol* 1997;30:8–18.

---

[54] Nagueh SF. Noninvasive evaluation of hemodynamics by Doppler echocardiography. *Curr Opin Cardiol* 14: 217-224, 1999

[55] Nagueh SF, Middleton KJ, Kopelen HA, Zoghbi WA, and Quinones MA. Doppler tissue imaging: a noninvasive technique for evaluation of left ventricular relaxation and estimation of filling pressures. *J Am Coll Cardiol* 30: 1527-1533, 1997

[56] Sanderson JE, Wang M and Yu CM. Tissue Doppler imaging for predicting outcome in patients with cardiovascular disease. *Curr Opin Cardiol* 19:458–463, 2004.

[57] Kwan J, Shiota T, Agler DA, Popvic ZB et al. Geometric Differences of the Mitral Apparatus Between Ischemic and Dilated Cardiomyopathy With Significant Mitral Regurgitation: Real-Time Three-Dimensional Echocardiography Study. *Circulation*. 2003;107:1135-1140

[58] Mori K, Edagawa T, Inoue M et al. Peak negative myocardial velocity gradient and wall-thickening velocity during early diastole are noninvasive parameters of left ventricular diastolic function in patients with Duchenne's progressive muscular dystrophy. *J Am Soc Echocardiogr* 2004;17:322–9.

[59] Ozer N, Can I, Atalar E, Sade E, et al. Left ventricular long-axis function is reduced in patients with rheumatic mitral stenosis. *Echocardiography*. 2004 Feb;21(2):107-12.

[60] Kranidis A, Kostopoulos K, Anthopoulos L. Evaluation of left ventricular filling by echocardiographic atrioventricular plane displacement in patients with coronary artery disease. *Int J Cardiol* 1995;48:183– 6.

[61] Alam M, Hǿglund C. Assessment by echocardiogram of left ventricular diastolic function in healthy subjects using the atrioventricular plane displacement. *Am J Cardiol* 1992;69:505– 65.

[62] Galiuto L, Ignone G, DeMaria AN. Contraction and relaxation velocities of the normal left ventricle using pulsed-wave tissue Doppler echocardiography. *Am J Cardiol* 1998, 81:609-614.

[63] Fukuda K, Oki T, Tabata T, Luchi A, Ito S. Regional left ventricular wall motion abnormalities in myocardial infarction and mitral annular descent velocities studied with pulsed tissue Doppler imaging. *J Am Soc Echocardiography* 1998, 11(9):841-848.

[64] Kheradvar A, Milano M, Gorman RC, Gorman III, JH, Gharib M. Assessment of left ventricular elastic and viscous components based on ventricular harmonic behavior. *Cardiovasc Eng* 2006: 2006 March 6(1): 30-39

[65] Carr-White GS, Gibson DG. Mitral annulus dynamics: Determinant of left ventricular filling. *J Cardiol* 2001: 37(suppl I):27-32.

[66] Glasson JR, Komeda M, Daughters GT, et al. Most ovine mitral annular three-dimensional size reduction occurs before ventricular systole and is abolished with ventricular pacing. Circulation 1997;96 (Suppl II):115–22.

[67] Glasson JR, Green GR, Nistal JF, et al. Mitral annular size and shape in sheep with annuloplasty rings. *J Thorac Cardiovasc Surg* 1998;117:302–9.

[68] Gorman III JH, Gupta KB, Streicher JT, et al. Dynamic three dimensional imaging of the mitral valve and left ventricle by rapid sonomicrometry array localization. *J Thorac Cardiovasc Surg* 1996;112:712–26.

[69] Komoda T, Hetzer R, Uyama C, et al. Mitral annular function assessed by 3D imaging for mitral valve surgery. *J Heart Valve Dis* 1994;3:483–90.

---

[70] Ormiston JA, Shah P, Tei C, Wong M. Size and motion of the mitral valve annulus in man. *Circulation* 1981;64:113–20.

[71] Pai RG, Tanimoto M, Jintapakorn W, Azevedo J, Pandian NG, Shah PM. Volume-rendered three-dimensional dynamic anatomy of the mitral annulus using transesophageal echocardiographic technique. *J Heart Valve Dis* 1995;4:623–7.

[72] Vierendeels, J. A., E. Dick, and P. R. Verdonck. Hydrodynamics of color M-mode Doppler flow wave propagation velocity V(p): A computer study, *J. Am. Soc. Echocardiogr* 2002; 15:219–224.

[73] Kheradvar A, Milano M, Gharib M. Correlation between vortex ring formation and mitral annulus dynamics during ventricular rapid filling. *ASAIO J* in press.

[74] Choong CY, Herrmann HC, Weymann AE, Fifer MA. Preload dependence of Doppler-derived indexes of left ventricular diastolic function in humans. *J Am Coll Cardiol* 1987;10:800–8.

[75] Kuo LC, Quinones MA, Rokey R, Sartori M, Abinader EG, Zoghbi WA. Quantification of atrial contribution to left ventricular filling by pulsed Doppler echocardiography and the effect of age in normal and diseased hearts. *Am J Cardiol* 1987;59:1174–8.

[76] Sohn DW, Chai IH, Lee DJ, Kim HC, et al. Assessment of mitral annulus velocity by Doppler Tissue imaging in the evaluation of left ventricular diastolic function. *J Am Coll Cardiol* 1997; 30:474-480.

[77] Sabbah HN, Stein PD. Pressure-diameter relations during early diastole in dogs: incompatibility with the concept of passive left ventricular filling. *Circ Res.* 1981; 48: 357–365

[78] Keren G, Sonnenblick EH, LeJemtel TH: Mitral annulus motion: relation to pulmonary venous and transmitral flows in normal subjects and in patients with dilated cardiomyopathy. *Circulation* 1988; 78:621

[79] Garcia MJ, Thomas JD, Klein AL. New Doppler echocardiographic applications for the study of diastolic function. *J Am Coll Cardiol* 1998;32:865–75.

[80] Nagueh SF, Middleton KJ, Kopelen HA, Zoghbi WA, Quinones MA. Doppler tissue imaging: a noninvasive technique for evaluation of left ventricular relaxation and estimation of filling pressures. *J Am Coll Cardiol* 1997;30:1527–33.

[81] Chiu YL, Ballou EW, Ford LE. Internal viscoelsatic loading in cat papillary muscle. *Biophys J.* 1982 Nov;40(2):109-20.

[82] Noble MI. The diastolic viscous properties of cat papillary muscle. *Circ Res*. 1977 Mar;40(3):288-92

[83] Chiu YL, Ballou EW, Ford LE. Velocity transients and viscoelsatic resistance to active shortening in cat papillary muscle. *Biophys J*. 1982 Nov;40(2):121-8.

[84] Garcia MJ and Thomas JD. Tissue Doppler to assess diastolic left ventricular function. *Echocardiography*1999, 16(5):501-508.

[85] Thomas JD and Weyman AE. Echocardiographic Doppler evaluation of left ventricular diastolic function: physics and physiology. *Circulation* 1991; 84(3): 977-990.

[86] Rowlatt U. Functional morphology of the heart in mammals. *Am Zool*. 1968 May;8(2):221-9.

[87] Suga H, Sagawa K. Instantaneous pressure-volume relationships and their ratio in the excised, supported canine left ventricle. *Circ Res* 1974;35: 117-126.

---

[88] McQueen DM, Peskin CS A three-dimensional computer model of the human heart for studying cardiac fluid dynamics. *Computer Graphics-US* 34 (1): 56-60 FEB 2000

[89] Takaoka H, Takeuchi M, Odake M, Yokoyama M. Assessment of myocardial oxygen consumption ($\dot{V}O_2$) and systolic pressure-volume area (PVA) in human hearts. *Eur Heart J.* 1992;13:85-90

[90] Applegate RJ, Cheng CP, Little WC. Simultaneous conductance catheter and dimension assessment of left ventricular volume in the intact animal. *Circulation* 1990;81: 638-648.

[91] Burkhoff D, de Tombe PP, and Hunter WC. Impact of ejection on the magnitude and time course of ventricular pressure generating capacity. *Am J Physiol Heart Circ Physiol* 1993;265: H899–H909.

[92] Campbell KB, Shroff SG, and Kirkpatrick RD. Short time-scale LV systolic dynamics: evidence for a common mechanism in both LV chamber and heart-muscle mechanics. *Circ Res* 1991;68: 1532–1548.

[93] Campbell KB, Kirkpatrick RD, Knowlen GG, and Ringo JA. Late systolic mechanical properties of the left ventricle: deviation from elastance- resistance behavior. *Circ Res* 1990;66: 218–233.

[94] Shroff SG, Campbell KB, and Kirkpatrick RD. Short time-scale LV systolic dynamics: pressure vs. flow clamps and effects of activation. *Am J Physiol Heart Circ Physiol* 1993;264: H946–H959.

[95] Templeton GH, Nardizzi LR. Elastic and viscous stiffness of the canine left ventricle. *J Appl Physiol* 1974; 36(1): 123-127.

[96] Campbell, KB, Wu Y, Simpson AM, Kirkpatrick RD, Shroff SG, Granzier HL, and Slinker BK. Dynamic myocardial contractile parameters from left ventricular pressure volume measurements. *Am J Physiol Heart Circ Physiol* 2005;289:H114–H130

[97] Kovacs SJ, Barzilai B, Perez JE. Evaluation of diastolic function with Doppler echocardiography: the PDF formalism. *Am Jf Physiol Heart Circ Physiol* 1987;252 (1): H178-H187 Part 2.

[98] Hunter WC, Janicki JS, WeberKT and Noordergraaf A. Systolic mechanical properties of the left ventricle. Effects of volume and contractile state. *Circ Res* 1983; 52;319-327.

[99] Chiu YL, Ballou EW and Ford LE. Internal viscoelastic loading in cat papillary muscle. *Biophys J* 1982; 40:109–120.

[100] Chiu, YL, Ballou EW and Ford LE. Velocity transients and viscoelastic resistance to active shortening in cat papillary muscle. *Biophys J* 1982;40: 121-128.

[101] Schmiel FK, Lorenzen N, Fischer G, Harding P, Kramer HH. Diastolic left ventricular function Experimental study of the early filling period using the Voigt model. *Basic Res Cardiol*. 2005 Jan;100(1):64-74.

[102] Rich MW, Stitziel NO, Kovacs SJ. Prognostic value of diastolic filling parameters derived using a novel image processing technique in patients >= 70 years of age with congestive heart failure *Am J Cardiol* 1999; 84 (1): 82-86.

[103] Brecher GA. Experimental evidence of ventricular diastolic suction. *Circ Res* 1956; 4:513-518.

[104] Firstenberg MS, Smedira NG, Greenberg NL, Prior DL, et al. Relationship between early diastolic intraventricular pressure gradients, an index of elastic recoil, and improvements in systolic and diastolic function. *Circulation*. 2001 Sep 18;104(12 Suppl 1):I330-5.

---

[105] Ling D, Rankin JS, Edwards CH II, et al. Regional diastolic mechanics of the left ventricle in the conscious dog. *Am J Physiol*. 1979;236 H323–H330.

[106] Nikolic SD, Feneley MP, Pajaro OE, et al. Origin of regional pressure gradients in the left ventricle during early diastole. *Am J Physiol*. 1995; 268:H550–H557.

[107] Burkhoff D, Mirsky I and Suga H. Assessment of systolic and diastolic ventricular properties via pressure-volume analysis: a guide for clinical, translational, and basic researchers. *Am J Physiol Heart Circ Physiol* 2005; 289:501-512.

[108] Burkhoff D and Sagawa K. Ventricular efficiency predicted by an analytical model. *Am J Physiol Regul Integr Comp Physiol* 1986; 250: R1021– R1027.

[109] Cazorla O, Wu Y, Irving TC, Granzier H. Titin-based modulation of calcium sensitivity of active tension in mouse skinned cardiac myocytes. *Circ Res.* 2001; 88: 1028–1035

[110] Fukuda N, Sasaki D, Ishiwata S, Kurihara S. Length dependence of tension generation in rat skinned cardiac muscle: role of titin in the Frank-Starling mechanism of the heart. *Circulation.* 2001; 104: 1639–1645.

[111] Granzier HL, Labeit S.The Giant Protein Titin: A Major Player in Myocardial Mechanics, Signaling, and Disease. *Circ Res* 2004;94;284-295

[112] Ljung L, System identification – Theory for the user , Prentice-Hall, Englewood Cliffs, N J, 1987

[113] Söderström T, Fan H, Carlsson B, and Bigi S. Least Squares Parameter Estimation of Continuous-Time ARX models from Discrete-Time Data. *IEEE Trans*. On Automatic Control, 1997;42 (5): 659-673.

[114] Kass DA, Maughan WL. From “Emax” to pressure-volume relations: a broader view. *Circulation* 1988;77:1203–12.

[115] Chen CH, Fetics B, Nevo E, Rochitte CE, Chiou KR, et al. Noninvasive Single-Beat Determination of Left Ventricular End-Systolic Elastance in Humans. *J Am Coll Cardiol* 2001;38:2028 –34

[116] Bland JM, Altman DG. Statistical methods for assessing agreement between two methods of clinical measurement. *Lancet i* 1986: 307-310,

[117] Haberman R. Mathematical models: Mechanical vibrations, population dynamics and traffic flow. *SIAM*, 1998.

[118] Opitz CA, Kulke M, Leake MC, Neagoe C, Hinssen H, Hajjar RJ and Linke WA. Damped elastic recoil of the titin spring in myofibrils of human myocardium. *Proc. Natl. Acad. Sci. USA* 2003; 100, 12688-12693.

[119] Kulke M, Fujita-Becker S, Rostkova E, Neagoe C, Labeit D, Manstein DJ, Gautel M, Linke WA. Interaction between PEVK-titin and actin filaments: origin of a viscous force component in cardiac myofibrils. *Circ Res.* 2001; 89: 874–881.

[120] Pfeffer MA, Braunwald E. Ventricular remodeling after myocardial infarction; experimental observations and clinical implications. *Circulation* 81(4) 1990.

[121] Gaudron P, Eilles C, Kugler I, et al. Progressive left ventricular dysfunction and remodeling after myocardial infarction: potential mechanism and early predictors. *Circulation*. 1993;87:755–763.

---

[122] Simonson JS, Schiller NB. Descent of the base of the left ventricle: an echocardiographic index of left ventricular function. *J Am Soc Echocardiogr* 1989;2:25-35.

[123] Alam M. The atrioventricular plane displacement as a means to evaluate left ventricular function in acute myocardial infarction. *Clin Cardiol* 1991;14:588-94.

[124] Moainie SL, Gorman III JH, Guy TS, Bowen III FW, et al. An Ovine Model of Postinfarction Dilated Cardiomyopathy. *Annals of Thoracic Surgery* 74: 753-760, 2002

[125] Markovitz LJ, Savage EB, Ratcliffe MB, et al. Large animal model of left ventricular aneurysm. *Ann Thorac Surg* 1989; 48:838-845

[126] Gorman II JH I, Gorman RC, Jackson BM, Enomoto Y, et al. Annuloplasty Ring Selection for Chronic Ischemic Mitral Regurgitation: Lessons from the Ovine Model. *Annals of Thoracic Surgery* 76:1556-1563, 2003

[127] Llaneras MR, Nance ML, Streicher JT, et al. Large animal model of ischemic mitral regurgitation. *Ann Thorac Surg* 1994; 57: 432-439.

[128] Edwards CH, Rankin JS, McHale PA. Effects of ischemia on left ventricular regional function in the conscious dog. *Am J Physiol Heart Circ Physiol* 240:H413-H420, 1981

[129] Steine K, Stugaard M, Smiseth OA. Mechanisms of retarded apical filling in acute ischemic left ventricular failure. *Circulation*. 1999;99: 2048–2054.

[130] Simpson IA. Echocardiographic assessment of the long axis: a simple solution to a complex problem. *Heart* 1997;78:211–2.

[131] Glower DD, Schaper J, Kabas JS, et al. Relation between reversal of diastolic creep and recovery of systolic function after ischemic myocardial injury in conscious dogs. *Circ Res.* 1987 Jun;60(6):850-60.

[132] Chareonthaitawee P, Christian TF, Hirose K, Gibbons RJ, Rumberger JA. Relation of initial infarct size to extent of left ventricular remodeling in the year after acute myocardial infarction. *J Am Coll Cardiol*. 1995;25(3):567-73.

[133] Boyle MP, Weisman HF. Limitation of infarct expansion and ventricular remodeling by late reperfusion. Study of time course and mechanism in a rat model. Circulation. 1993;88(6):2872-83.

[134] Eaton LW, Weiss JL, Bulkley BH, et al. Regional cardiac dilatation after acute myocardial infarction. *N Engl J Med* 1979;300:57-62

[135] Betten J. Creep mechanics**.** Berlin ; New York : Springer, 2002

[136] Pai RG, Gill KS. Amplitudes, durations, and timings of apically directed left ventricular myocardial velocities: II. Systolic and diastolic asynchrony in patients with left ventricular hypertrophy. *J Am Soc Echocardiogr*. 1998 Feb;11(2):112-8.

[137] Olivetti G, Capasso JM, Meggs LG, Sonnenblick EH, Anversa P. Cellular basis of chronic ventricular remodeling after myocardial infarction in rats. *Cirs Res* 1991;68:856-869

[138] Lind B, Eriksson M, Roumina S, Nowak J, Brodin LA. Longitudinal isovolumic displacement of the left ventricular myocardium assessed by tissue velocity echocardiography in healthy individuals. *J Am Soc Echocardiogr*. 2006 Mar;19(3):255-65.